SIZE-DEPENDENT DYNAMICS OF FLEXOELECTRIC AND FLEXOELECTRIC-PIEZOELECTRIC STRUCTURES

A Dissertation
Presented to
The Academic Faculty

by

Adriane G. Moura

In Partial Fulfillment
of the Requirements for the Degree
Doctor of Philosophy in the
George W. Woodruff School of Mechanical Engineering

Georgia Institute of Technology
August 2019

SIZE-DEPENDENT DYNAMICS OF FLEXOELECTRIC AND FLEXOELECTRIC-PIEZOELECTRIC STRUCTURES

Approved by:

Dr. Alper Erturk, Committee Chair
Mechanical Engineering
Georgia Institute of Technology

Dr. Alper Erturk, Advisor
Mechanical Engineering
Georgia Institute of Technology

Dr. F. Levent Degertekin
Mechanical Engineering
Georgia Institute of Technology

Dr. Julien Meaud
Mechanical Engineering
Georgia Institute of Technology

Dr. Karim Sabra
Mechanical Engineering
Georgia Institute of Technology

Dr. Qian Deng
Aerospace Engineering
Xi'an Jiaotong University

Date Approved: 17 June 2019

ACKNOWLEDGEMENTS

I would like to thank the many people who guided, encouraged, and supported me over the years of my doctoral studies at Georgia Tech. First, with deepest gratitude, I express my thanks to my advisor, Dr. Alper Erturk for his tireless support and guidance. Special thanks also to Drs. F. Levent Degertekin, Julien Meaud, Karim Sabra and Qian Deng for reviewing my work and providing valuable insights and comments. I had a great pleasure in working with past and present members of the SSDSL and would like to thank them all for their helpful suggestions and feedback.

I am deeply grateful to my family for always supporting my dreams and encouraging me during this journey. To the many friends who accompanied me along this journey, I would like to express my thanks for making it enjoyable and memorable. Most importantly I express my deepest gratitude and appreciation to my husband Silvino, for his sacrifices, encouragement, support, and patience throughout my doctoral studies. Lastly, all praise and honor to God for providing me this opportunity and granting me the capability to proceed successfully.

This work was supported by the National Science Foundation grant CMMI-1463339, which I gratefully acknowledge.

TABLE OF CONTENTS

LIST OF FIGURES

SUMMARY

Flexoelectricity is the generation of electric polarization by the application of a non-uniform mechanical strain field, i.e. a strain gradient. Unlike piezoelectricity (strain-induced polarization), flexoelectric coupling is associated with a fourth rank tensor, and is exhibited by all elastic dielectrics regardless of the material symmetry; however, as a gradient effect, flexoelectricity is expected to be significant only at very small scales. This work aims to develop electromechanical models to analyze the dynamics and vibration of structures leveraging flexoelectricity and to establish analytical and approximate analytical frameworks for next-generation submicron concepts and devices for energy harvesting, sensing, and actuation. At such small geometric scales, flexoelectricity enables electromechanical behavior even in non-piezoelectric dielectric materials, while it enhances the electromechanical coupling in piezoelectric ones. In particular, energy harvesting is a potential future application area of flexoelectricity to enable ultra-low-power nanoscale devices by converting vibrations into electricity. The focus of this work is first placed on bending vibration of centrosymmetric cantilevers, such as a monolayer STO (Strontium Titanate) cantilever. An electroelastodynamic framework is presented and analyzed for flexoelectric power generation from strain gradient fluctuations in centrosymmetric dielectrics, by accounting for the presence of a finite electrical load across the surface electrodes as well as two-way electromechanical coupling, and capturing the size effect. Following recent efforts on the converse flexoelectric effect in finite samples, the proposed model properly accounts for a thermodynamically consistent, symmetric two-way coupling, i.e. the direct and converse effects. In addition to the electromechanical frequency response functions, the transverse mode flexoelectric coupling coefficient (a direct measure of energy conversion) is obtained analytically; its dependence on the cantilever thickness and a material figure of merit is shown. It is obtained that the flexoelectric coupling coefficient (k) of an STO cantilever for the fundamental bending mode increases from $k \approx 3.5 \times 10^{-7}$ to $k \approx 0.33$ as the thickness is

reduced from mm- to nm-level. A critique of the experimentally identified large flexoelectric coefficient for Barium Strontium Titanate (BST) (for mm-thick samples) from the existing literature is also given with a coupling coefficient perspective. The modeling framework is then extended to non-centrosymmetric configurations, such as bimorph cantilevers made from Barium Titanate (BTO), to understand the interaction between flexoelectricity and piezoelectricity for different thickness levels from mm-scale to nm-scale, with a focus on resonant energy harvesting and actuation dynamics. The level of enhancement in the overall electromechanical coupling due to flexoelectricity with reduced thickness is quantified. The flexoelectric-piezoelectric coupling increases from the bulk piezoelectric value of $k \approx 0.0652$ at the mm-scale to $k \approx 0.365$ at the nm-scale owing to flexoelectric contribution. The effects of varying cross section and aspect ratio are also of interest, which requires the use of approximate analytical electromechanical modeling frameworks such as the assumed-modes method used in conjunction with an energy formulation. An increase in the coupling coefficient was seen when the uniform cross-section beam ($k \approx 0.105$) was changed to a tapered beam with narrow tip ($k \approx 0.119$). Geometrically nonlinear frameworks for flexoelectric and flexoelectric-piezoelectric configurations are also developed. Modeling frameworks for the linear vibration of flexoelectric and flexoelectric-piezoelectric thin plates are also developed and the simulation results are compared to those of the beams. It is obtained that the flexoelectric coupling coefficient of an STO simply supported plate for the fundamental bending mode increases from $k \approx 3.6 \times 10^{-7}$ to $k \approx 0.34$ as the thickness is reduced from mm- to nm-level. Other than bending vibrations leveraging the transverse mode, this work includes the leveraging of axial vibrations to develop a framework for the dynamics and vibration of truncated nanostructures in thickness mode. As the thickness is reduced from mm- to nm-level, the flexoelectric axial electromechanical coupling coefficient of an STO truncated cone increases from $k \approx 0$ to $k \approx 0.00397$ for the fundamental longitudinal mode. In all numerical case studies for the continuum models proposed in this work, atomistic values of the flexoelectric constants are used as the only reliable data in the current literature.

CHAPTER I

INTRODUCTION

1.1 Background and motivation

Microelectromechanical systems (MEMS) and nanoelectromechanical systems (NEMS) have received growing attention in the last decade for various applications including mechanical energy harvesting at very small scales [19, 51, 17, 67]. The mechanical energy in this context spans from structure-borne vibrations [5] and waves [15, 79] to rigid-body motions [63, 30], acoustic energy [22, 21, 69], as well as aeroelastic [33, 25] and hydroelastic [4, 32] vibrations. In harvesting various forms of mechanical energy, piezoelectricity remains arguably the most widely studied transduction method with examples ranging from PZT-based (lead zirconate titanate) ferroelectric thin-films [17] to piezoelectric nanowires [67] employing non-ferroelectrics, such as ZnO (zinc oxide). Examples of such MEMS energy harvester are shown in Fig. 1. It is well known that the electromechanical coupling [1] of piezoelectric materials diminishes dramatically in thin films [80] and polymers [39]. Piezoelectric polymers, such as PVDF (polyvinylidene fluoride), are environmentally benign as compared to ceramics but they are poor power generators due to low electromechanical coupling. Bulk piezoelectric ceramics (such as PZT-5A and PZT-5H) are relatively brittle and less reliable for powering sensor systems in harsh environments. Moreover, lead content in most piezoelectric ceramic compositions is a major environmental issue [58]. Furthermore, several of the high electromechanical coupling materials lose their piezoelectricity at moderate to high temperatures, where self-powered sensors are most needed.

Recent efforts at small scales [59] suggest that the effective electromechanical properties of elastic dielectrics can be enhanced dramatically under non-uniform strain fields due to an entirely different phenomenon called flexoelectricity [75, 76, 89, 82, 65, 84]. Flexoelectricity describes the generation of electric polarization in elastic dielectrics by the application of a mechanical strain gradient [76, 82, 60]. The phenomenon of flexoelectricity in solids is

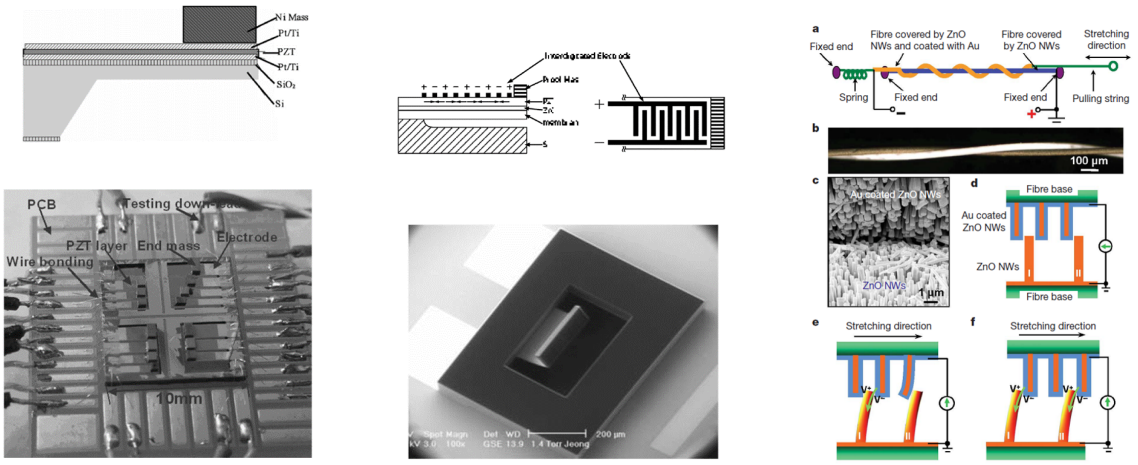

(a) **(b)** **(c)**

Figure 1: MEMS energy harvesters examples: **(a)** Thick film PZT array of cantilevers from Liu et al. [51]. **(b)** Thin film ZnO (zinc oxide) cantilever with interdigitated electrodes from Choi et al. [17]. **(c)** Nanogenerator of fiber based ZnO nanowires from Qin et al. [67].

a higher-order effect and is expected to be rather weak except for very small (sub-micron) dimensions, making the concept of interest mainly for potential MEMS and especially NEMS applications. Following the early efforts by Mashkevich and Tolpygo [61], Kogan [45], and Indenbom et al. [43], the first comprehensive theoretical discussion of the flexoelectric effect was presented by Tagantsev [75]. The research field of flexoelectricity has been active for liquid crystals [13] and biological matter [66, 28] for decades. However, it was only in early 2000s the flexoelectric effect in solids has received suddenly growing attention especially after the experiments by Ma and Cross [52, 53, 56, 54, 55, 57] on elastic dielectrics, specifically high-K materials such as ferroelectric perovskites (see the review article by Cross [20]). In addition to experimental efforts by Ma and Cross [52, 53, 56, 54, 55, 57] and others [87, 88, 42] for samples with high dielectric constants, atomistic simulations [60] were presented to extract flexoelectric coefficients. Importantly, substantial difference (several orders of magnitude) was reported between the simulated and experimentally identified flexoelectric coefficients [57]. The experimental samples [52, 53, 56, 54, 55, 57] (of ∼mm thickness) used in the identification efforts were typically far from the thickness levels of interest (< 100 nm) in flexoelectricity. A comprehensive article on the flexoelectric effect in solids by Yudin and Tagantsev [82] presents a detailed discussion on the subject matter along with a historical

account. It is no surprise that, with its promise of increased electromechanical coupling at small scales, flexoelectricity is of great interest for submicron level energy harvesting [59, 27] to power next-generation nanoscale sensors and other extremely low-power small electronic components.

Other than the mismatch in the order of magnitude of flexoelectric coupling between atomistic simulations [60] and experimental measurements [52, 53, 56, 54, 55, 57], one of the issues in flexoelectric transduction and energy conversion has been the lack of a clear understanding and modeling of the converse effect, as the subject has created confusion since the converse effect is represented by a polarization gradient [40, 14, 62]. For instance, it was suggested ([20, 18]) that mechanical flexoelectric sensors could be made with no actuation property (which has no precedent or thermodynamic basis) due to a limited interpretation of the constitutive equation for the converse effect. In a recent work focusing on finite samples, Tagantsev and Yurkov [77] presented a consistent and symmetric converse effect representation and its justification. Part of the research goal in this proposal aims to extend such concepts on flexoelectricity to electromechanical structural dynamics frameworks to capture size dependent response in energy harvesting and actuation. Furthermore, any ordinary piezoelectric cantilever model developed for devices above micron-level thickness has to be modified for next-generation nanoscale devices since the effect of flexoelectric coupling will change the electroelastic dynamics at such small scales.

1.2 Flexoelectricity and piezoelectricity

In elastic dielectrics, piezoelectricity is the response of polarization to applied mechanical strain, and vice versa. Piezoelectric coupling is controlled by a third-rank tensor and is allowed only in materials that are non-centrosymmetric. Flexoelectricity, on the other hand, is the generation of electric polarization by the application of a non-uniform mechanical strain field, i.e. a strain gradient, and is expected to be pronounced at submicron thickness levels, especially at the nano-scale. Flexoelectricity is controlled by a fourth-rank tensor and is therefore allowed in materials of any symmetry, i.e. a piezoelectric material also exhibits the flexoelectric effect at very low thickness levels. As a gradient effect, flexoelectricity is

size dependent, while piezoelectric coupling has no size dependence.

1.2.1 Transverse mode Euler-Bernoulli thin beam constitutive equations

Cantilever beams are often used for MEMS energy harvesting devices [31] as shown in Fig. 1. The strain gradient from bending a thin cantilever beam induces polarization by separating the negative and positive material particles in a unit cell as shown in Fig. 2 [27]. The induced polarization vector in the deformed beam (Fig. 2b) is in the x_3-direction.

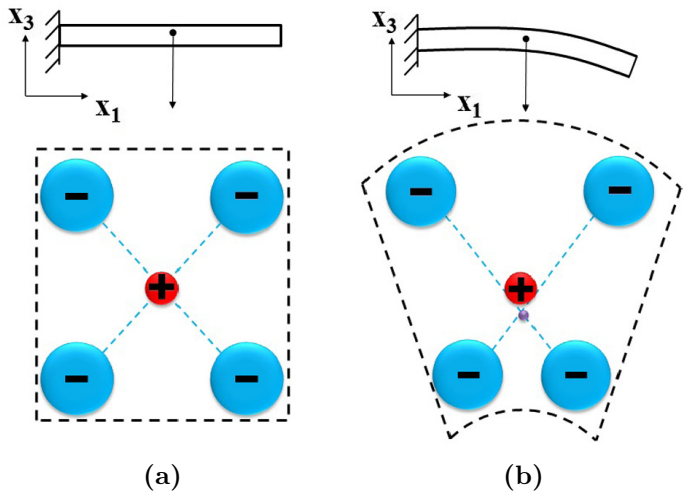

Figure 2: Polarization in a centrosymmetric beam due to bending: **(a)** undeformed **(b)** deformed (Figure from Deng et al. [27]).

The resulting polarization for a centrosymmetric cantilever, including the *direct* flexoelectric effect, for the transverse mode can be written as

$$P_3 = \chi_{33} E_3 + \mu_{1133} \frac{\partial S_{11}}{\partial x_3} \tag{1}$$

where P_3 is the polarization in thickness direction (3-direction is the thickness direction and 1-direction is the axial direction), E_3 is the electric field, S_{11} is the axial strain, χ_{33} is the dielectric susceptibility (which has the units of F/m, and should not be confused with the dimensionless electric susceptibility form $\bar{\chi}_{33}$, $\chi_{33} = \bar{\chi}_{33}\varepsilon_0$, where ε_0 is the vacuum permittivity), and μ_{1133} is the transverse flexoelectric coefficient.

For the transverse mode, the mechanical stress accounting for the *converse* flexoelectric effect can be expressed as

$$T_{11} = c_{1111} S_{11} + f_{1133} \frac{\partial P_3}{\partial x_3} \tag{2}$$

or alternatively

$$T_{11} = c_{1111} S_{11} + \mu_{1133} \frac{\partial E_3}{\partial x_3} \tag{3}$$

where T_{11} is the axial stress, c_{1111} is the elastic modulus (under short-circuit condition of the electrodes), and f_{1133} is the transverse mode "flexocoupling coefficient" [82] ($f_{1133} = \chi_{33}^{-1} \mu_{1133}$). Note that the above form [82] neglects the strain gradient elasticity [27, 41] and is suitable for basic "exogenous" strain gradients, such as those due to mechanical bending, but would be limited for "endogenous" ones, such as those due to domain boundaries and interfaces, which are beyond the scope of this work (see Section 3.1 in Tagantsev and Yudin [82] for more discussion).

A piezoelectric material can also exhibit flexoelectricity [10, 2]. For instance, the combined transverse mode flexoelectric-piezoelectric effects yield the following constitutive equations (that relate the stress and electric displacement to strain and electric field):

$$T_{11} = c_{1111} S_{11} - e_{311} E_3 + \mu_{1133} \frac{\partial E_3}{\partial x_3} \tag{4}$$

$$D_3 = \varepsilon_{33} E_3 + e_{311} S_{11} + \mu_{1133} \frac{\partial S_{11}}{\partial x_3} \tag{5}$$

where e_{311} is the piezoelectric constant, D_3 is the electric displacement, and ε_{33} is the dielectric permittivity. The form of Eqs. 4 and 5 contains both the piezoelectric and the flexoelectric effects, and therefore it is applicable to a wide range of geometric scales.

1.2.2 Transverse mode Kirchhoff thin plate constitutive equations

In many thin film configurations the length and width become comparable as seen in Figs. 1a and 1b. Such MEMS configurations are more of a plate where torsion/twist related modes can easily be excited/pronounced which cannot be captured with beam models. Existing literature for 2-dimensional flexoelectric effects is limited to biomembranes [66]. Therefore to properly account for the two-dimensional behavior of the MEMS devices, a plate model including the flexoelectric effect must be developed. The stress state for Kirchhoff thin

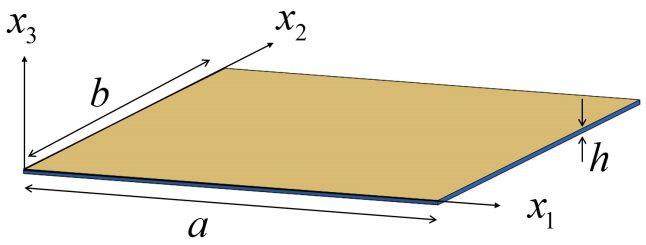

Figure 3: Kirchhoff thin plate with lateral dimensions a and b and thickness h.

flexoelectric-piezoelectric plate (Fig. 3) is

$$\begin{aligned} T_{11} &= c_{1111}S_{11} + c_{1122}S_{22} - e_{311}E_3 + f_{1133}\frac{\partial P_3}{\partial x_3} \\ T_{22} &= c_{1122}S_{11} + c_{1111}S_{22} - e_{311}E_3 + f_{1133}\frac{\partial P_3}{\partial x_3} \\ T_{12} &= c_{1212}S_{12} \end{aligned} \tag{6}$$

The electric displacement is

$$D_3 = \varepsilon_{33}E_3 + e_{311}S_{11} + e_{311}S_{22} + \mu_{1133}\frac{\partial S_{11}}{\partial x_3} + \mu_{1133}\frac{\partial S_{22}}{\partial x_3} \tag{7}$$

1.2.3 Axial mode constitutive equations

Axial strain-induced polarization in piezoelectric structures (e.g. stacks and monolithic elements [85, 74, 22]) is not associated with any size dependence. However, flexoelectric polarization enables the possibility of generating polarization from strain gradients associated with axial deformation of non-uniform geometries (i.e. under a given axial load, non-uniform geometry results in non-homogeneous strain field, hence strain gradients). One example is the truncated pyramid configuration as depicted in Fig 4a which is considered a standard experimental configuration (for the longitudinal mode) since the early work by Cross [20]. Another example of inducing strain gradient is the truncated cone (studied by Deng [26]) as shown in Fig. 4b.

In their simplest form, the respective constitutive equations for the axial mode (incorporating both flexoelectricity and piezoelectricity) are:

$$T_{33} = c_{3333}S_{33} - e_{333}E_3 + \mu_{3333}\frac{\partial E_3}{\partial x_3} \tag{8}$$

$$D_3 = \varepsilon_{33} E_3 + e_{333} S_{33} + \mu_{3333} \frac{\partial S_3}{\partial x_3} \tag{9}$$

However, because of the comparable lateral dimensions (Fig. 4a), rather than standard one-dimensional longitudinal vibration investigation, enhanced longitudinal vibration models must be employed such as the Rayleigh-Love and Rayleigh-Bishop type models accounting for the lateral inertia and shear effects [12].

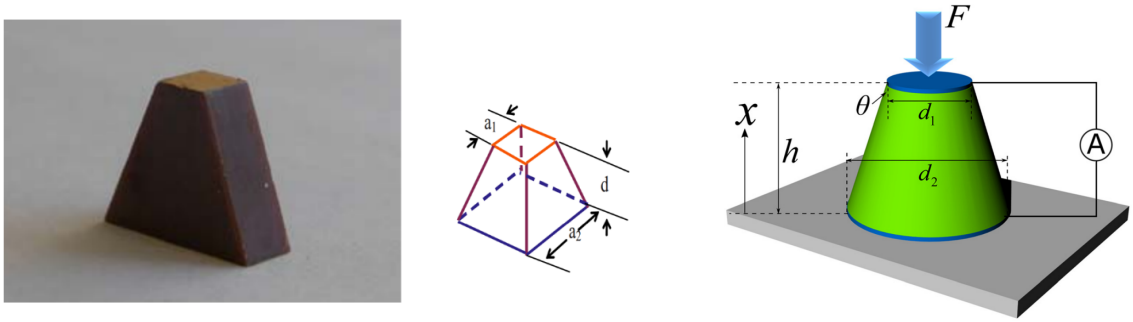

(a) **(b)**

Figure 4: **(a)** Truncated pyramid configurations (experimental sample and composite arrangements with a building block) for exploiting longitudinal (or thickness) flexoelectric mode from Cross [20] and **(b)** a truncated cone under compression as analytically analyzed by Deng [26]

1.3 Geometric nonlinearities in flexoelectric structures

MEMS and NEMS applications often involve large excitation levels that create nonlinear motions (Figs. 1b and 1c). These nonlinearities have to be modeled for accurate prediction of the response and can also be exploited to enhance the frequency bandwidth of effective energy harvesting. Recently, a few research groups have studied the nonlinear behavior of flexoelectric nanobeams. Such studies include nonlinear frequency behavior of Euler-Bernoulli beams using surface elasticity method [7], nonlinear free vibration and post buckling of nanobeams with the flexoelectric effect [83], and nonlinear vibration of flexoelectric beams using the strain gradient theory [86]. The main focus of these studies was the change in the frequency ratio parameter with varying electrical and mechanical parameters. Limited work has been done on capturing the nonlinear jump phenomenon that results from purely geometric hardening in flexoelectric nanobeams. Recently, Dai et al. [23] studied a geometrically nonliner microbeam under harmonic tip forcing for optimization of forcing,

damping, and load resistance where equations resulted in linear coupling and were solved using Galerkins method. The moderately large deformation can be modeled by accounting for an inextensible cantilever as done by Tan et al. [78] for piezoelectric beams. It is also shown that nonlinear electromechanical coupling can result from the inextensibility condition even when linear constitutive equations are used.

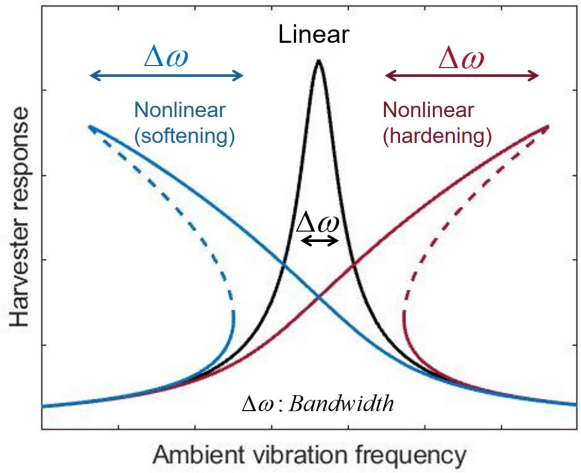

Figure 5: Linear vs. monostable nonlinear energy harvester frequency response curves demonstrating the bandwidth enhancement.

Beyond its inherent presence under large deformations, there is an advantage of nonlinear frequency response especially in energy harvesting. A limitation of linear vibration energy harvesting is that the effective power generation performance of the device is limited to resonance excitation. Any slight deviation of the excitation frequency from the resonance frequency (due to environmental conditions or changes in excitation, etc.) results in significant decreases in harvester performance (orders of magnitude). Intentionally designed nonlinearities have been employed by a number of research groups to enhance the frequency bandwidth of vibration energy harvesters [24]. Typically the backbone curve of nonlinear resonance that is associated with increased excitation intensity enables the desired frequency bandwidth amplification in monostable configurations as depicted in Fig. 5. Specifically the jump phenomenon [64] that is associated with up-sweep in hardening nonlinearity and down-sweep in softening nonlinearity results in significant bandwidth enhancement in monostable settings [46, 47] and more complex bandwidth enhancement mechanisms take

place in bistable or generalized multistable configurations [24, 35, 6].

1.4 Dissertation outline

Having reviewed the flexoelectric literature, it is important to investigate flexoelectrically coupled electroelasticdynamic modeling frameworks for energy harvesting and actuation of MEMS devices to gain a fundamental understanding of exploiting the size effects of strain gradients. The development of flexoelectric models is essential to predict the performance of next generation MEMS devices. Therefore, the main goal of this dissertation research is to establish analytical and approximate analytical modeling and analysis frameworks for dynamics of structures leveraging flexoelectric and flexoelectric-piezoelectric behaviors for various configurations (transverse mode, axial mode, varying cross-section, etc.) and geometric scales.

In this context, the following chapters are outlined as follows: Chapter II describes the transverse mode flexoelectric modeling framework developed for bending vibration of a centrosymmetric (non-piezoelectric) cantilevered beam under base excitation for resonant energy harvesting and actuation, accounting for direct and converse flexoelectric effects. Chapter III extends the previous chapter to a bimorph cantilevered beam including both flexoelectric and piezoelectric effects. Chapter IV further extends the model to varying cross-section cantilevered beams. Chapter V describes the geometrically nonlinear framework for flexoelectric and flexoelectric-piezoelectric cantilever beams under moderately large base excitation. Chapter VI extends the beam modeling framework to plate structures. Chapter VII describes the dynamics of longitudinal (axial) mode flexoelectric structures. Chapter VIII concludes the dissertation by summarizing the contributions made to the field of flexoelectricity and MEMS energy harvesting and opportunities for further work.

CHAPTER II

FLEXOELECTRIC MONOLAYER CANTILEVER MODEL FOR BENDING VIBRATIONS

2.1 Introduction

In this chapter, we combine the direct effect of flexoelectricity and the symmetric converse effect [77] within a distributed-parameter electroelastodynamic framework and provide a modal analysis solution for vibration energy harvesting from base excitation of dielectric cantilevers. In addition to closed-form expressions for the electromechanically coupled voltage across the electrical load and the shunted vibration response (that accounts for the effect of the electrical load), the size-dependent flexoelectric coupling coefficient is extracted analytically, and a figure of merit is identified. Simulation case studies are given for transverse vibrations of a cantilevered Strontium Titanate (STO) energy harvester at different geometric scales to explore the effect of thickness on flexoelectric energy conversion as well as the effect of power generation on the harvester structure due to converse coupling.

2.2 Centrosymmetric Euler-Bernoulli cantilever model for flexoelectric energy harvesting and actuation

We consider the problem of a centrosymmetric thin cantilever under mechanical base excitation and voltage actuation (Fig. 6) for linear transverse (bending) vibrations, i.e. linear electroelastic material behavior and geometrically small oscillations are assumed in this continuum framework. In Fig. 6a, the surface electrodes of the cantilever are shunted to a resistive electrical load to quantify the electrical power output in the harvester model. The sample geometry justifies thin beam assumptions, such that the width (b) and the thickness (h) of the rectangular cross section are much smaller than the overhang length (L). Static flexoelectricity [82] is applicable since the thickness (smallest dimension) of the beam is much smaller than the wavelength at vibration frequencies of interest in this work for the first few bending modes. In the following, the focus is placed on static bulk flexoelectricity,

and therefore the surface effects [89, 82] are excluded. The direct and converse effects are

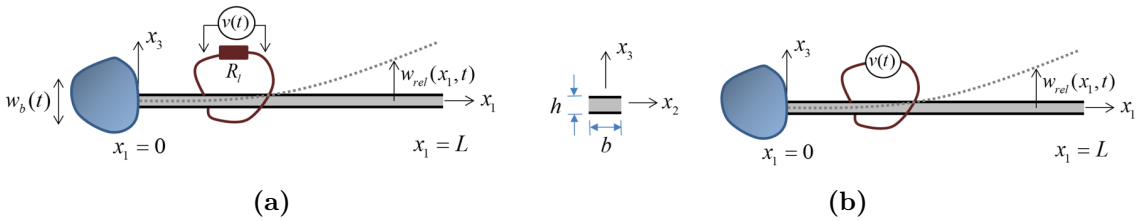

Figure 6: **(a)** Base-excited centrosymmetric dielectric cantilever with surface electrodes (that are perpendicular to the thickness direction) connected to a resistive electrical load for energy harvesting, and a cross-sectional view. The transverse displacement of the beam relative to the moving base is w_{rel} and the voltage output across the resistive load is v. **(b)** Dynamic actuation configuration of the same cantilever (the base is fixed).

defined as given by Eqs. 1 and 3 in Chapter 1. The dynamic actuation problem for a fixed base is depicted in Fig. 6b. In the following, first the energy harvesting problem will be formulated and then will also be rearranged for dynamic voltage actuation.

The partial differential equation governing the forced vibration of a uniform cantilevered centrosymmetric thin dielectric beam under transverse base excitation (Fig. 6a) is

$$-\frac{\partial^2 M(x_1,t)}{\partial {x_1}^2}+c_s I\frac{\partial^5 w_{rel}(x_1,t)}{\partial {x_1}^4 \partial t}+c_a\frac{\partial w_{rel}(x_1,t)}{\partial t}+m\frac{\partial^2 w_{rel}(x_1,t)}{\partial t^2}=-m\frac{d^2 w_b(t)}{dt^2} \quad (10)$$

where $w_b(t)$ is the base excitation (in the form of displacement), $w_{rel}(t)$ is the transverse displacement of the beam (reference surface, or neutral axial level) relative to its base, $M(x_1,t)$ is the internal bending moment at position x_1 and time t, c_a is the viscous air damping coefficient (as a mass-proportional dissipative term), c_s is the strain-rate damping coefficient (as a stiffness-proportional dissipative term), and m is the mass per unit length of the beam ($m=\rho bh$ where ρ is the mass density of the beam material). In the same vein as cantilevered piezoelectric energy harvester counterparts [36, 37], the linear damping operators in Eq. 10 satisfy the proportional damping condition so that the mode shapes of the corresponding undamped system can be used in modal analysis (implementation of nonlinear intrinsic and extrinsic damping mechanisms is beyond the scope of this work see Leadenham and Erturk [48, 46], among others, for the resonant modeling of quadratic solid [48] and fluid [46] damping).

The internal bending moment in Eq. 10 is the first moment of the axial stress field over

the cross-section and can be expressed as

$$M(x_1,t) = b \int_{-h/2}^{h/2} T_{11} x_3 dx_3 \tag{11}$$

The axial strain component is due to bending only and it can be expressed as

$$S_{11}(x_1,x_3,t) = -x_3 \frac{\partial^2 w_{rel}(x_1,t)}{\partial {x_1}^2} \tag{12}$$

It is clear from Eqs. 1 and 12 that the *strain gradient*, $\partial S_{11}/\partial x_3$, in this model is nothing but the negative curvature of the uniform Euler-Bernoulli beam (assuming the effect of the gradient $\partial S_{11}/\partial x_1$ to be negligible).

Substituting Eq. 2 into the bending moment in Eq. 11 gives

$$M(x_1,t) = b \left(\int_{-h/2}^{h/2} c_{1111} S_{11} x_3 dx_3 + \int_{-h/2}^{h/2} f_{1133} \frac{\partial P_3}{\partial x_3} x_3 dx_3 \right) \tag{13}$$

Following Tagantsev and Yurkov [77], for a finite sample in which the polarization in the thickness direction varies continuously from its bulk value to zero at the top and bottom surfaces of the cantilever at $x_3 = h/2$ and $x_3 = -h/2$ (see Fig. 12a in Yudin and Tagantsev [82]), the second right-hand-side term can be evaluated using integration by parts to identify the role of this term in the moment equation:

$$b f_{1133} \int_{-h/2}^{h/2} \frac{\partial P_3}{\partial x_3} x_3 dx_3 = -b f_{1133} \int_{-h/2}^{h/2} P_3 dx_3 = -b f_{1133} h \langle P_3 \rangle \tag{14}$$

where $\langle P_3 \rangle$ is the average polarization induced by the electric field in the beam. The spatial scale of the polarization variation at the dielectric-electrode interface is much smaller than that in the overall thickness h, therefore this average polarization is approximately the polarization in the bulk [82, 77]:

$$\langle P_3 \rangle \approx \chi_{33} E_3 \tag{15}$$

where the electric field, E_3, can be given in terms of the voltage (v) across the surface electrodes and the electrode spacing as $E_3 = -v/h$ (where it is assumed that the electrode thickness is negligible). It is useful to recall from Eqs. 3 and 2 that the dielectric susceptibility, χ_{33} is

$$\chi_{33} = \mu_{1133}/f_{1133} \tag{16}$$

The flexoelectric term in Eq. 14 is only a function of time, therefore it is multiplied by $[H(x_1) - H(x_1 - L)]$ (where $H(x_1)$ is the Heaviside function), to ensure the survival of this term when the bending moment is substituted into Eq. 10, for full electrode coverage (Fig. 6a) from the clamped end ($x_1 = 0$) to the free end ($x_1 = L$). The internal bending moment is then

$$M(x_1, t) = -YI\frac{\partial^2 w_{rel}(x_1, t)}{\partial {x_1}^2} + \mu_{1133} bv(t)[H(x_1) - H(x_1 - L)] \tag{17}$$

where the flexural rigidity, YI, for the rectangular cross-section (under short-circuit condition) is

$$YI = \frac{c_{1111} bh^3}{12} \tag{18}$$

The flexoelectrically coupled centrosymmetric Euler-Bernoulli beam equation for transverse vibrations can then be obtained from Eq. 10 as

$$\begin{aligned} YI\frac{\partial^4 w_{rel}(x_1, t)}{\partial {x_1}^4} + c_s I\frac{\partial^5 w_{rel}(x_1, t)}{\partial {x_1}^4 \partial t} + c_a\frac{\partial w_{rel}(x_1, t)}{\partial t} + m\frac{\partial^2 w_{rel}(x_1, t)}{\partial t^2} + \\ -\mu_{1133} bv(t)\left[\frac{d\delta(x_1)}{dx_1} - \frac{d\delta(x_1 - L)}{dx_1}\right] = -m\frac{d^2 w_b(t)}{dt^2} \end{aligned} \tag{19}$$

where $\delta(x_1)$ is the Dirac delta function that satisfies the following equation for a smooth test function $\gamma(x_1)$:

$$\int_{-\infty}^{\infty} \frac{d^{(n)}\delta(x_1 - p)}{dx_1^{(n)}}\gamma(x_1)dx_1 = (-1)^n \frac{d\gamma^{(n)}(p)}{dx_1^{(n)}} \tag{20}$$

The vibration response (transverse displacement of the reference surface, i.e. neutral axis level) relative to the moving base in Fig. 6 can be expressed as

$$w_{rel}(x_1, t) = \sum_{r=1}^{\infty} \phi_r(x_1)\eta_r(t) \tag{21}$$

Here $\eta_r(t)$ is the modal mechanical coordinate and $\phi_r(x_1)$ is the mass-normalized eigenfunction (obtained from the short-circuit problem) for the r-th vibration mode:

$$\phi_r(x_1) = \sqrt{\frac{1}{mL}}\left[\cos\frac{\lambda_r x_1}{L} - \cosh\frac{\lambda_r x_1}{L} + \sigma_r\left(\sin\frac{\lambda_r x_1}{L} - \sinh\frac{\lambda_r x_1}{L}\right)\right] \tag{22}$$

where $\sigma_r = \frac{\sin\lambda_r - \sinh\lambda_r}{\cos\lambda_r + \cosh\lambda_r}$ and the eigenvalues ($\lambda_r > 0, r = 1, 2, ...$) are the roots of the characteristic equation (for the short-circuit and clamped-free boundary conditions):

$$1 + \cos(\lambda_r)\cosh(\lambda_r) = 0 \tag{23}$$

The mass-normalized eigenfunctions in Eq. (15) satisfy the following orthogonality conditions:

$$\begin{aligned} \int_0^L m\phi_r(x_1)\phi_s(x_1)dx_1 &= \delta_{rs} \\ \int_0^L YI\phi_r(x_1)\frac{d^4\phi_s(x_1)}{dx_1^4}dx_1 &= \delta_{rs}\omega_r^2 \end{aligned} \tag{24}$$

where δ_{rs} is the Kronecker delta and ω_r is the undamped natural frequency of the r-th vibration mode under short-circuit conditions ($R_l \to 0$):

$$\omega_r = \lambda_r^2\sqrt{\frac{YI}{mL^4}} \tag{25}$$

which can also be denoted by ω_r^{sc}, the short-circuit natural frequency of the r-th mode.

The mechanical equation in modal coordinates can be obtained as

$$\frac{d^2\eta_r(t)}{dt^2} + 2\zeta_r\omega_r\frac{d\eta_r(t)}{dt} + {\omega_r}^2\eta_r(t) - \theta_r v(t) = f_r(t) \tag{26}$$

where ζ_r is the modal mechanical damping ratio of r-th vibration mode (due to purely mechanical dissipation) that can easily be related to c_s and c_a as $2\zeta_r\omega_r = c_sI\omega_r^2/YI + c_a/m$. The modal electromechanical coupling term due to flexoelectricity is

$$\theta_r = \mu_{1133}b\left.\frac{d\phi_r(x_1)}{dx_1}\right|_{x_1=L} \tag{27}$$

and the mechanical forcing function can be expressed as

$$f_r(t) = -m\frac{d^2w_b(t)}{dt^2}\int_0^L \phi_r(x_1)dx_1 \tag{28}$$

In order to obtain an electrical circuit equation in the presence of a finite electrical load impedance, it is useful to obtain the electric displacement that is compatible with the polarization form of Eq. 1 through the well-known dielectric relationship $D_3 = P_3 + \varepsilon_0 E_3$. The non-zero electric displacement component for transverse vibrations of the thin beam configuration with surface electrodes shown in Fig. 6 is then

$$D_3 = \varepsilon_{33}E_3 + \mu_{1133}\frac{\partial S_{11}}{\partial x_3} \tag{29}$$

where ε_{33} is the dielectric permittivity, $\varepsilon_{33} = \varepsilon_0 + \chi_{33} = (1 + \bar{\chi_{33}})\varepsilon_0$ (note that for high-K materials, which are of interest in flexoelectricity, $\bar{\chi_{33}} >> 1,$ and $\varepsilon_{33} \approx \chi_{33}$).

In the presence of a finite resistive load connected across the electrodes of the beam, the flexoelectrically coupled circuit equation is obtained from the integral

$$\frac{d}{dt}\left(\int_A \mathbf{D}\cdot\mathbf{n}dA\right) = \frac{v(t)}{R_l} \tag{30}$$

where $\mathbf{D}$ is the vector of electric displacement components, $\mathbf{n}$ is the unit outward normal of the electrodes, and the integration is performed over the electrode area A. The only contribution to the inner product of the integrand is from D_3 given by Eq. 29.

Using Eq. 29 in Eq. 30 the following circuit equation (current balance) is obtained:

$$C\frac{dv(t)}{dt} + \frac{v(t)}{R_l} + \mu_{1133}b\int_0^L \frac{\partial^3 w_{rel}(x_1,t)}{\partial {x_1}^2 \partial t}dx_1 = 0 \tag{31}$$

where the capacitance C is

$$C = \frac{\varepsilon_{33}bL}{h} \tag{32}$$

The modal electrical equation then obtained by substituting Eq. 21 into Eq. 31 as

$$C\frac{dv(t)}{dt} + \frac{v(t)}{R_l} + \sum_{r=1}^{\infty}\theta_r\frac{d\eta_r(t)}{dt} = 0 \tag{33}$$

Here, the modal electromechanical coupling (θ_r) due to the *direct* flexoelectric effect is the same as Eq. 27 that was obtained from the *converse* effect, which further confirms the symmetry in the fully coupled governing electroelastodynamic equations, which are Eqs. 26 and 33 in modal coordinates. Flexoelectric power generation as a result of voltage output across the resistive load is due to Eq. 33, and simultaneously the voltage output sends a feedback to the mechanical domain due to the voltage term in Eq. 26, as a manifestation of the thermodynamic consistency resulting from the two-way coupling.

In the voltage actuation problem (for a fixed base, i.e. $f_r(t) = 0$), Eqs. 26 and 33 become

$$\frac{d^2\eta_r(t)}{dt^2} + 2\zeta_r\omega_r\frac{d\eta_r(t)}{dt} + {\omega_r}^2\eta_r(t) = \theta_r v(t) \tag{34}$$

$$i(t) = C\frac{dv(t)}{dt} + \sum_{r=1}^{\infty}\theta_r\frac{d\eta_r(t)}{dt} \tag{35}$$

where $i(t)$ is the electric current input associated with dynamic actuation.

2.3 Electromechanical frequency response at steady state

2.3.1 Voltage and vibration response for energy harvesting

For harmonic base excitation ($w_b(t) = W_0 e^{j\omega t}$), the modal forcing given by Eq. 28 can be expressed as $f_r(t) = F_r e^{j\omega t}$, where the amplitude F_r is

$$F_r = \omega^2 m W_0 \int_0^L \phi_r(x_1) dx_1 \tag{36}$$

Then, the steady-state modal mechanical coordinate of the beam and the steady-state voltage response across the resistive load are also harmonic at the same frequency as $\eta_r(t) = H_r e^{j\omega t}$ and $v(t) = V e^{j\omega t}$, respectively, where the amplitudes H_r and V are complex valued. Therefore, the modal mechanical and electrical equations (Eqs. 26 and 33) yield

$$(\omega_r^2 - \omega_r + j2\zeta_r\omega_r\omega)H_r - \theta_r V = F_r \tag{37}$$

$$\left(\frac{1}{R_l} + j\omega C\right) V + j\omega \sum_{r=1}^{\infty} \theta_r H_r = 0 \tag{38}$$

The steady state voltage response is obtained from Eqs. 37 and 38 as

$$v(t) = \frac{\sum_{r=1}^{\infty} \frac{-j\omega\theta_r F_r}{\omega_r^2 - \omega^2 + j2\zeta_r\omega_r\omega}}{\frac{1}{R_l} + j\omega C + \sum_{r=1}^{\infty} \frac{j\omega\theta_r^2}{\omega_r^2 - \omega^2 + j2\zeta_r\omega_r\omega}} e^{j\omega t} \tag{39}$$

Once the voltage across the electrical load is obtained, the current and power output can be calculated easily. For the case of a real-valued electrical load (i.e. resistive load), the current delivered to the load is $i(t) = v(t)/R_l$ and the instantaneous power output is $P(t) = v^2(t)/R_l$.

The steady-state vibration response of the beam (that accounts for the converse effect) can be obtained as

$$w_{rel}(x_1, t) = \sum_{r=1}^{\infty} \left[\left(F_r - \theta_r \frac{\sum_{r=1}^{\infty} \frac{j\omega\theta_r F_r}{\omega_r^2 - \omega^2 + j2\zeta_r\omega_r\omega}}{\frac{1}{R_l} + j\omega C + \sum_{r=1}^{\infty} \frac{j\omega\theta_r^2}{\omega_r^2 - \omega^2 + j2\zeta_r\omega_r\omega}} \right) \frac{\phi_r(x_1) e^{j\omega t}}{\omega_r^2 - \omega^2 + j2\zeta_r\omega_r\omega} \right] \tag{40}$$

2.3.2 Vibration response and current drawn for actuation

The governing equations in energy harvesting can be modified to represent the actuation problem similarly such that there is no base excitation ($F_r = 0$) as given by Eqs. 34 and 35

and the excitation is due to harmonic voltage input. The steady state mechanical response and current are obtained as

$$w_{rel}(x_1,t)=\sum_{r=1}^{\infty}\frac{\theta_r\phi_r(x_1)}{\omega_r^2-\omega^2+j2\zeta_r\omega_r\omega}Ve^{j\omega t} \tag{41}$$

$$i(t)=j\omega\left(C+\sum_{r=1}^{\infty}\frac{\theta_r^2}{\omega_r^2-\omega^2+j2\zeta_r\omega_r\omega}\right)Ve^{j\omega t} \tag{42}$$

2.4 Size effects on modal electromechanical coupling coefficient

One direct measure of energy conversion is the electromechanical coupling coefficient k as commonly used in piezoelectricity [1, 49]. It is possible to analytically extract the transverse mode electromechanical coupling coefficient due to bulk flexoelectricity for the centrosymmetric cantilever of Fig. 6. A dynamic definition of the modal electromechanical coupling coefficient can be obtained based on the difference between the open-circuit and short-circuit natural frequencies [1, 49]:

$$k^2=\frac{(\omega_r^{oc})^2-(\omega_r^{sc})^2}{(\omega_r^{oc})^2} \tag{43}$$

where k is the *flexoelectric coupling coeffcient* for the r-th vibration mode (the focus in the simulations of this work will be placed on the fundamental mode, $r=1$). Square of the coupling coefficient, as well known from piezoelectric energy conversion problems, is a measure of how much of the mechanical work is converted to electrical energy, or vice versa in electrical actuation. A similar argument and an analogous expression can be given in terms of the open- and short-circuit stiffness terms in quasistatic conditions [1, 49].

For modal vibrations (dominated by the r-th mode) and under open-circuit conditions, Eq. 33 can be reduced to

$$v(t)=\frac{-\theta_r\eta_r(t)}{C},\ R_l\to\infty \tag{44}$$

Substituting Eq. 44 into the modal mechanical equation, Eq. 26, the undamped open-circuit natural frequency of the r-th vibration mode becomes

$$(\omega_r^{oc})^2=(\omega_r^{sc})^2\left(1+\frac{\theta_r^2}{\omega_r^2C}\right) \tag{45}$$

yielding

$$k^2 = \frac{\left(\frac{\theta_r^2}{\omega_r^2 C}\right)}{\left(1 + \frac{\theta_r^2}{\omega_r^2 C}\right)} = \frac{\theta_r^2}{\omega_r^2 C + \theta_r^2} \tag{46}$$

Here, the capacitance is given by Eq. 32 and the modal coupling term given by Eq. 27 can be expressed as

$$\theta_r = \mu_{1133} b \left.\frac{d\phi_r(x_1)}{dx_1}\right|_{x_1=L} = \mu_{1133} b \frac{1}{\sqrt{mL}} \frac{\lambda_r}{L} \alpha_r \tag{47}$$

where $\alpha_r = -\sin\lambda_r - \sinh\lambda_r + \frac{\sin\lambda_r - \sinh\lambda_r}{\cos\lambda_r + \cosh\lambda_r}(\cos\lambda_r - \cosh\lambda_r)$.

Equation 46 then becomes

$$k^2 = \frac{1}{\frac{c_{1111}\varepsilon_{33}}{\mu_{1133}^2} \frac{\lambda_r^2}{12\alpha_r^2} h^2 + 1} \tag{48}$$

The coupling coefficient for the centrosymmetric flexoelectric beam given by Eq. 48 clearly captures the thickness dependence of the modal flexoelectric coupling coefficient. Note that the fundamental (first) bending vibration mode ($r = 1$) is typically of interest for energy harvesting using a linear cantilever under base excitation [36, 37], yielding $\lambda_1 = 1.87510407$ and $\alpha_1 = -1.46819102$ for the simulations in this work (the first mode shape is shown in Fig. 7a). Energy harvesting at higher vibration modes requires using segmented electrodes to avoid charge cancellation [36, 37]. The fundamental bending mode results in no cancellation for continuous electrode coverage since the curvature is in phase throughout the length of the beam (Fig. 7c), i.e. there are no inflection points. Note that, 85% of the electric charge is produced by the first half of the cantilever, i.e. $0 \leq x_1 \leq L/2$, according to Fig. 7b (since the integral of curvature is related to the electric charge according to current balance Eq. 31 and the curvature is maximum near the clamped end in Fig. 7c). From the electromechanical coupling standpoint, 85% of the modal electromechanical coupling θ_1 (which determines the coupling coefficient k) is due to the region $0 \leq x_1 \leq L/2$, in view of Eq. 27 and Fig.7b.

In terms of the size effect, Eq. 48 shows that, with decreased thickness (h) the coupling coefficient (k) increases. This equation also shows the effect of the material properties on the coupling coefficient. The Figure of Merit (FoM) in flexoelectric energy conversion is

$$\text{FoM} = \frac{\mu_{1133}^2}{c_{1111}\varepsilon_{33}} = \frac{\left(\chi_{33} f_{1133}\right)^2}{c_{1111}\varepsilon_{33}} \tag{49}$$

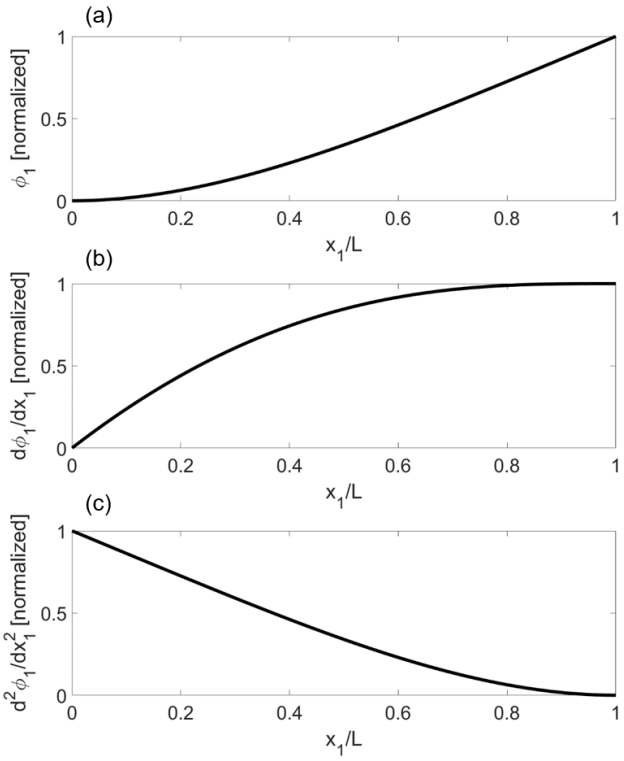

Figure 7: Normalized (a) displacement, (b) slope, and (c) curvature distributions of a thin cantilever for the fundamental bending vibration mode ($r = 1$). The maximum curvature is near the clamped end. The region $0 \leq x_1 \leq L/2$ produces 85% of the modal electromechanical coupling from Eq. 27 and Fig. 7b.

and as FoM $\to \infty$, $k^2 \to 1$ which is the limit of 100% mechanical-to-electrical energy conversion within the structure (note that it is not the percentage energy delivered to the electrical load, hence not an overall efficiency).

2.5 Case studies and results

In this section, simulations are performed to show the effect of thickness on the electromechanical coupling and the frequency response behavior of a flexoelectric uniform beam under bending vibrations for energy harvesting and actuation. The simulations are for Strontium Titanate (STO) using the elastic [9, 44] and dielectric [89, 3] properties of $c_{1111} = 318$ GPa, $\rho = 5116$ kg/m^3, and $\varepsilon_{33} = 2.66$ nF/m (for the room temperature relative permittivity [89, 88, 3], $\varepsilon_{33}/\varepsilon_0 = 300$), and using the atomistic flexoelectric coefficient value [60] of $\mu_{1133} = -3.75 \times 10^{-9}$ C/m.

2.5.1 Electromechanical coupling and size effects

The electromechanical coupling coefficient due to flexoelectric energy conversion, or simply the transverse mode flexoelectric coupling coefficient, k, is plotted for a range of FoM values and cantilever thicknesses in Fig. 8a. The focus is placed on the fundamental bending vibration mode ($r = 1$), and the beam thicknesses in the simulations range from 1 mm to 1 nm. As stated previously based on Eq. 48, the coupling coefficient increases with decreased thickness. This is now illustrated graphically in Fig. 8a. The coupling coefficient also increases with increased flexoelectric FoM defined by Eq. 49. The resulting FoM for STOs is around $\mu_{1133}{}^2/c_{1111}\varepsilon_{33} = 1.66 \times 10^{-20}$ m^2, yielding negligible coupling coefficient values except at the nanoscale according to Fig. 8a.

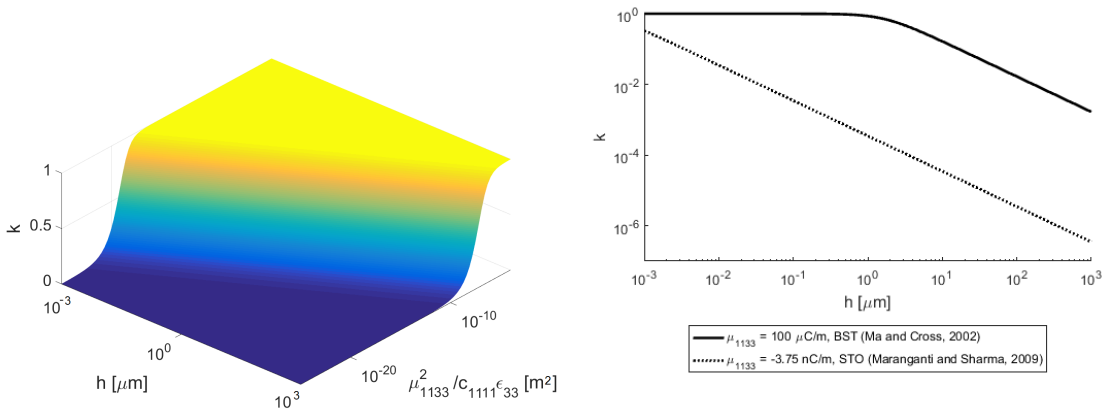

(a) **(b)**

Figure 8: **(a)** Transverse mode flexoelectric coupling coefficient vs. cantilever thickness and figure of merit in flexoelectric energy conversion (for the fundamental bending vibration mode). **(b)** Flexoelectric coupling coefficient (k) vs. thickness (h) plots obtained using sample flexoelectric coefficient (μ_{1133}) values identified by Ma and Cross [56] for BST (experimental) and calculated by Maranganti and Sharma [60] for STO (atomistic).

Typical atomistic simulations [60] result in flexoelectric coefficient values on the order of 10^{-9} C/m while the experimentally identified values (by Cross et al. [56, 57, 38] for mm-scale samples) are as high as 10^{-4} C/m. Consider the experimental value of $\mu_{1133} = 100 \times 10^{-6}$ C/m (the authors of the original paper [56] reported a positive value) for Barium Strontium Titanate (BST) from the experiments by Ma and Cross [56] for mm-thick samples. The elastic modulus and permittivity values of BST were reported in another

work by the same group [38] as $c_{1111} = 166$ GPa and $\varepsilon_{33} = 0.1594$ μF/m, respectively. The thickness dependence of the transverse mode coupling coefficient for these properties of BST is shown in Fig. 8b (solid line), along with that of STO (dashed line) based on the aforementioned atomistic values by Maranganti and Sharma [60] to demonstrate the order of magnitude difference between available experiments and atomistic simulations, although the materials are not identical. As expected, with decreased thickness, the coupling coefficient gradually approaches unity, indicating increased energy conversion with reduced thickness. Importantly, Fig. 8b reveals that, for $\mu_{1133} = 100 \times 10^{-6}$ C/m, the coupling coefficient is nearly unity for all submicron thickness levels, which makes the validity of this value (identified from mm-thick samples [56]) as a bulk flexoelectric coefficient questionable. Such an order of magnitude in bulk flexoelectric coefficient (10^{-4} C/m) suggests very high conversion even for micron-thick non-piezoelectric cantilevers, which, obviously, is not the case. This observation definitely encourages rigorous experiments at much smaller scales (ideally for thickness levels of less than ~ 100 nm). The trend in the second curve (dashed line) based on atomistic simulations [60] of STO (with $\mu_{1133} = -3.75 \times 10^{-}9$ C/m) is more reasonable, as it reveals that the coupling coefficient exceeds 0.1 only when the cantilever thickness is a few nanometers. Overall, reducing the thickness from 1 mm to 1 nm increases the flexoelectric coupling coefficient by nearly 6 orders of magnitude in the STO cantilever.

2.5.2 Electromechanical frequency response in energy harvesting

In this section, the electromechanical frequency response of a cantilevered flexoelectric energy harvester under base excitation is simulated with a focus on the first bending mode ($r = 1$) for a broad range of electrical load resistance values. Three different geometric scales are explored, spanning from mm-scale to nm-scale thickness. For each case the length/width/thickness aspect ratio is fixed at 100/5/1. The cantilever is made of STO and has perfectly conductive surface electrodes on the faces that are perpendicular to the direction of transverse base excitation (Fig. 6a). The results are given in the form of frequency response magnitude maps normalized by the base acceleration quantified in terms of the gravitational acceleration ($g = 9.81$ m/s^2) . A wide range of electrical load resistance

values spanning from short- to open-circuit conditions (100 Ω to 1 GΩ) are simulated for each case study to capture the optimal load in power generation and the respective trends with changing load.

The voltage output (per base acceleration) frequency response map (obtained from Eq. 39 via $\left|v(t)/-\omega^2 W_0 e^{j\omega t}\right|$ as the magnitude form) for the 1 mm-thick STO beam (100 mm x 5 mm x 1 mm) is shown in Fig. 9a.i. The base excitation frequency is normalized with respect to the fundamental short-circuit natural frequency in the vertical axis. With increased electrical load resistance, the voltage output increases monotonically at all frequencies, as a typical trend in energy harvesting [37]. It is shown that the resonance frequency for the 1 mm-thick STO cantilever is unaffected by the change in resistive load, i.e. the frequency of peak magnitude does not change as the electrical load resistance value is swept from short- to open-circuit conditions. This indicates very low electromechanical coupling such that the feedback in the mechanical domain due to induced low voltage is negligible. The flexoelectric coupling coefficient for the 1 mm thickness level and STO material property combination is obtained from Eq. 48 or Fig. 9a.i as $k \approx 3.5 \times 10^{-7}$, confirming negligible electromechanical coupling. The beam thickness is then decreased to 1 μm while keeping the same aspect ratio (i.e. the dimensions are now 100 μm x 5 μm x 1 μm) and the analysis is repeated. The voltage output frequency response map for this case is shown in Fig. 9a.ii. As with the 1 mm thickness case, the 1 μm-thick STO cantilever shows no noticeable change in the fundamental resonance frequency with changing load resistance. The flexoelectric coupling coefficient of this simulation case is $k \approx 3.5 \times 10^{-4}$, which, again, indicates very weak electromechanical coupling. Next, the beam thickness is further decreased to 1 nm and the analysis is repeated for a 100 nm x 5 nm x 1 nm sample. As shown by the voltage output frequency response map in Fig. 9a.iii, this nm-thick beam exhibits a certain shift in resonance frequency from short- to open-circuit conditions, which is a manifestation of significant electromechanical coupling according to Eq. 43. Decreasing the thickness of the cantilever (while keeping the same volumetric aspect ratio) results in increased electromechanical coupling, hence increased mechanical to electrical energy conversion. The electromechanical coupling for this thickness level is $k \approx 0.33$, which is in

agreement with nearly 5.6 % difference between the values of the fundamental short- and open-circuit resonance frequencies in Fig. 9a.iii. This can easily be confirmed using Eq. 43 (for ω_1^{sc}, ω_1^{oc}, and k relationship), since the resonance frequencies (frequencies of peak forced response magnitude) are very close to the natural frequencies in the lightly damped setting with $\zeta_1 = 0.01$.

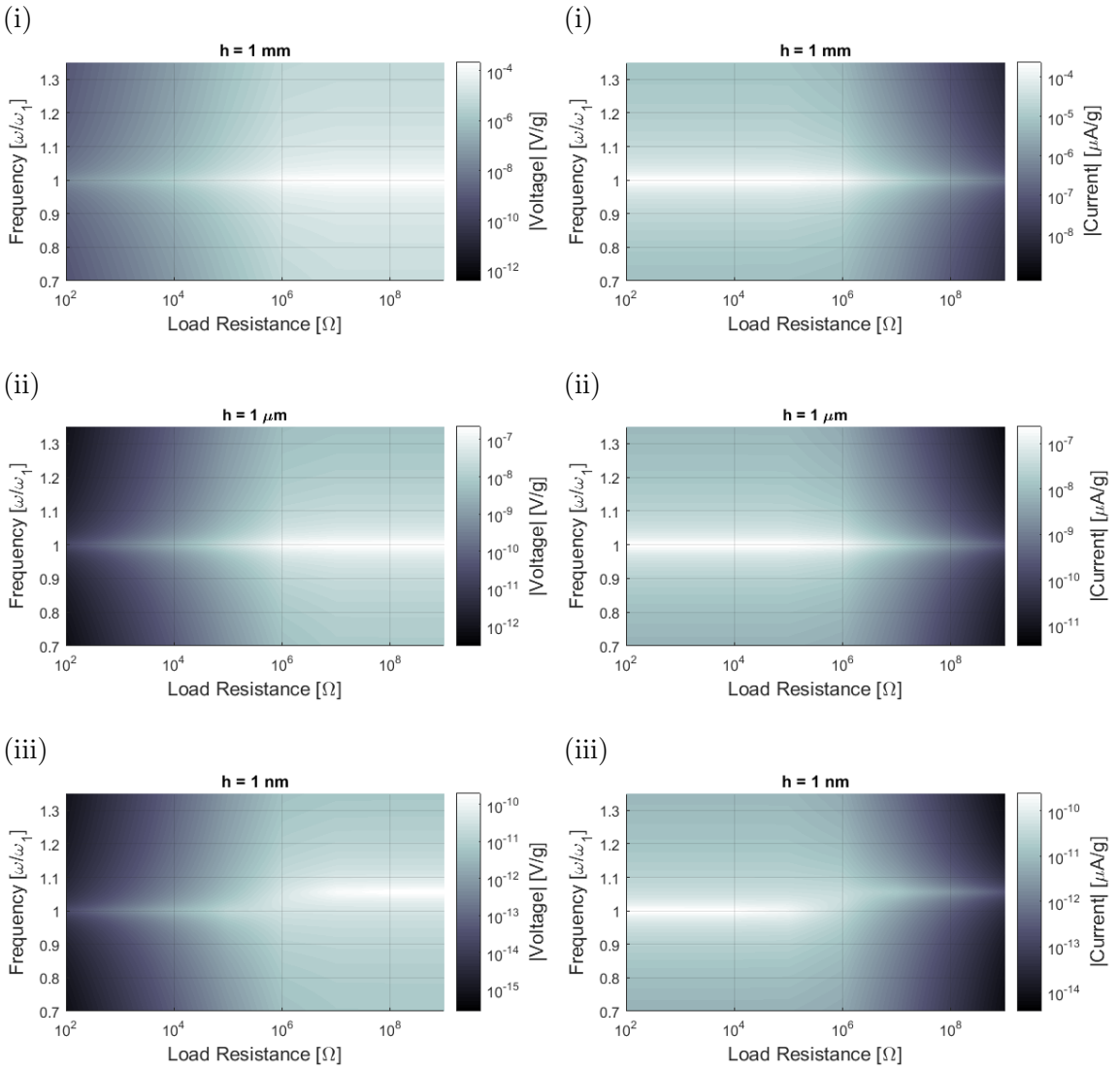

Figure 9: **(a)** Voltage output frequency response vs. load resistance maps (in magnitude form and per base acceleration) and **(b)** current output frequency response vs. load resistance maps (in magnitude form and per base acceleration) for cantilevered STO harvesters with a fixed aspect ratio of 100/5/1 ($L/b/h$) for three different geometric scales with the following thickness (h) values: (i) 1 mm, (ii) 1 μm, and (iii) 1 nm.

The electric current flowing to the resistive load is simply obtained from the voltage output using Ohms law. The current output (per base acceleration) frequency response maps (calculated using $\left|v(t)/-R_l\omega^2 W_0 e^{j\omega t}\right|$) are also generated for the STO cantilever configurations of each geometric scale using the previously mentioned fixed volumetric aspect ratio as displayed in Fig. 9b. The electric current decreases monotonically with increased electrical load resistance at all frequencies, which is the opposite trend as compared to the voltage output. At all frequencies, the maximum current is achieved under short-circuit conditions of the surface electrodes. As with the voltage output frequency response maps, similar trends are observed for each case study in terms of the flexoelectric coupling coefficient. The thickness levels of 1 mm and 1 μm show no noticeable shift in resonance frequency (Figs. 9b.i and 9b.ii), indicating negligible electromechanical coupling, whereas the 1 nm thickness case results significant frequency shift (Fig. 9b.iii), revealing strong electromechanical coupling as discussed previously for the voltage output.

As a product of two quantities which have opposite trends with changing load resistance (voltage and current), the electrical power output exhibits interesting trends, such as the presence of an optimal electrical load resulting in the maximum power output at a given frequency. The electrical power output is calculated using $\left|v(t)/-\omega^2 W_0 e^{j\omega t}\right|^2/R_l$ for each of the three geometric scales and the fixed aspect ratio discussed previously. The resulting graphs are shown in Fig. 10a. Note that, since the output voltage and current are individually proportional to the base acceleration, the power output is proportional to base acceleration squared (hence normalized by g^2), i.e. doubling the base acceleration increases the power output by a factor of 4 under the linear system assumption. The optimal load for peak power output can be determined for each case from the power output frequency response maps. For instance, the cases of both 1 mm and 1 μm-thick harvesters result in a peak power output around 1 MΩ. The 1 mm and 1 μm power output frequency response maps show the resonance frequency to be insensitive to the resistive load due to very low electromechanical coupling (Figs. 10a.i and 10a.ii). Consequently, a single optimal load is observed in the power map for the fundamental vibration mode. On the other hand, the 1 nm case study exhibits two peak values for two distinct optimal electrical loads, 100 kΩ and

10 MΩ, respectively at the short-circuit and open-circuit resonance frequencies, yielding the same power output (Fig. 10a.iii). The existence of two peaks in the power output is also the case in strongly coupled and lightly damped piezoelectric energy harvesters [37, 72, 73]. The same power output can be extracted at the short-circuit resonance frequency ($\sim \omega_1^{sc}$) for a lower electrical load resistance or at the open-circuit resonance frequency ($\sim \omega_1^{oc}$) for a larger electrical load resistance. As a result, the former optimal condition results in larger current and lower voltage, while the latter gives larger voltage and lower current.

It is also of interest to explore what happens to the structural response of the STO cantilever while generating electricity from strain gradient fluctuations in response to mechanical base excitation. The motion of the cantilever can be evaluated at any position (x_1) using Eq. 40, while the focus is typically placed on the tip ($x_1 = L$). Figure 10b shows the tip displacement map (per base acceleration input via $\left|w_{rel}(L,t)/-\omega^2 W_0 e^{j\omega t}\right|$) for the cantilevers of all three geometric scales for the same load resistance and normalized excitation frequency ranges discussed previously. For the cases of 1 mm and 1 μm thickness levels, as another manifestation of very weak electromechanical coupling at these geometric scales, the vibration response of the cantilever is insensitive to changing electrical load resistance(Figs. 10b.i and 10b.ii). That is, although some power output is delivered to the electrical load according to Figs. 10a.i and 10a.ii, the level of this electrical output is so small that it is negligible as compared to mechanical (vibrational) energy of the harvester (confirmed by the coupling coefficient values), and this tiny level of electricity production does not alter the vibration response although the converse effect is taken into account in the model (i.e. the converse flexoelectric effect is negligible at these geometric scales). Therefore, as a result of weak electromechanical coupling, Joule heating in the resistive load does not create any significant dissipation in the vibration response of the STO cantilever. However, for the cantilever with 1 nm thickness, the electromechanical coupling is relatively strong, and therefore mechanical to electrical energy conversion is rather significant. As a consequence, the response of the harvester is sensitive to changing electrical load in Fig. 10b.iii in the vicinity of the resonance. Certain load resistance values result in significant shunt damping, analogous to piezoelectric shunt damping [37, 50], confirming

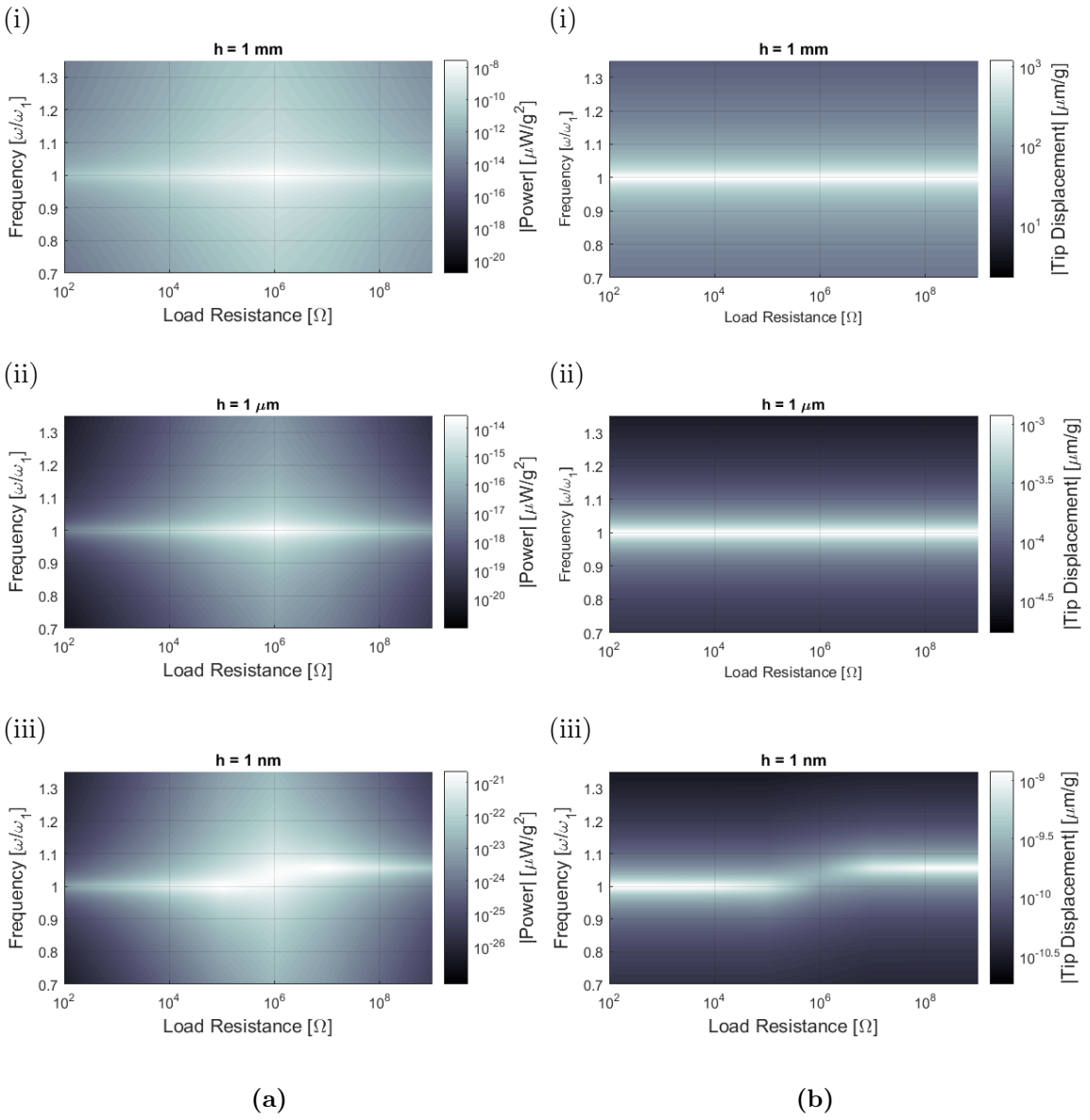

Figure 10: **(a)** Power output frequency response vs. load resistance maps (in magnitude form and per base acceleration squared) and **(b)** tip displacement frequency response vs. load resistance maps (in magnitude form and per base acceleration) for cantilevered STO harvesters with a fixed aspect ratio of 100/5/1 ($L/b/h$) for three different geometric scales with the following thickness (h) values: (i) 1 mm, (ii) 1 μm, and (iii) 1 nm.

thermodynamic consistency of the fully coupled electroelastodynamic model.

2.5.3 Electromechanical frequency response in actuation

The same modeling framework is also employed to understand the electromechanical response of the cantilever in the case of electrical excitation for the same set of system parameters. Of interest, is the tip displacement frequency response (structural response for unit actuation voltage input) from Eq. 41 and the admittance frequency response (amount of current drawn for unit actuation voltage input) calculated from Eq. 42. The tip displacement and admittance frequency responses are shown in Figs. 11a and 11b, respectively. These frequency response functions show, once again, that significant electromechanical coupling only occurs at the nm-scale (Figs 11a.iii and 11b.iii).

2.6 Conclusions

An electroelastodynamic framework is developed and analyzed for flexoelectric energy harvesting from strain gradient fluctuations in centrosymmetric dielectrics, by accounting for the presence of a finite electrical load across the surface electrodes as well as two-way electromechanical coupling. The model is then extended to the dynamic actuation problem for a fixed base. The flexoelectric energy harvester and actuation model presented in this work is based on the Euler-Bernoulli beam theory and it assumes the main source of polarization to be static bulk flexoelectricity. Following recent efforts on the converse flexoelectric effect in finite samples, the proposed model properly accounts for thermodynamically consistent, symmetric, direct and converse coupling terms, and it captures the size effect on the coupling coefficient.

Based on a modal analysis procedure, closed-form solutions of the electromechanical frequency response functions (voltage across the electrical load and coupled vibration response) are given. Results of an extensive analysis are presented at different geometric scales (mm, μm, and nm thickness levels with a fixed aspect ratio) for a Strontium Titanate (STO) cantilever that is shunted to a resistive electrical load for quantifying the electrical power output and its feedback on the vibration response due to the converse effect. Harmonic excitation is assumed and the focus of the numerical study is placed on the fundamental bending mode, which is the most flexible mode and it results in no charge cancellation when

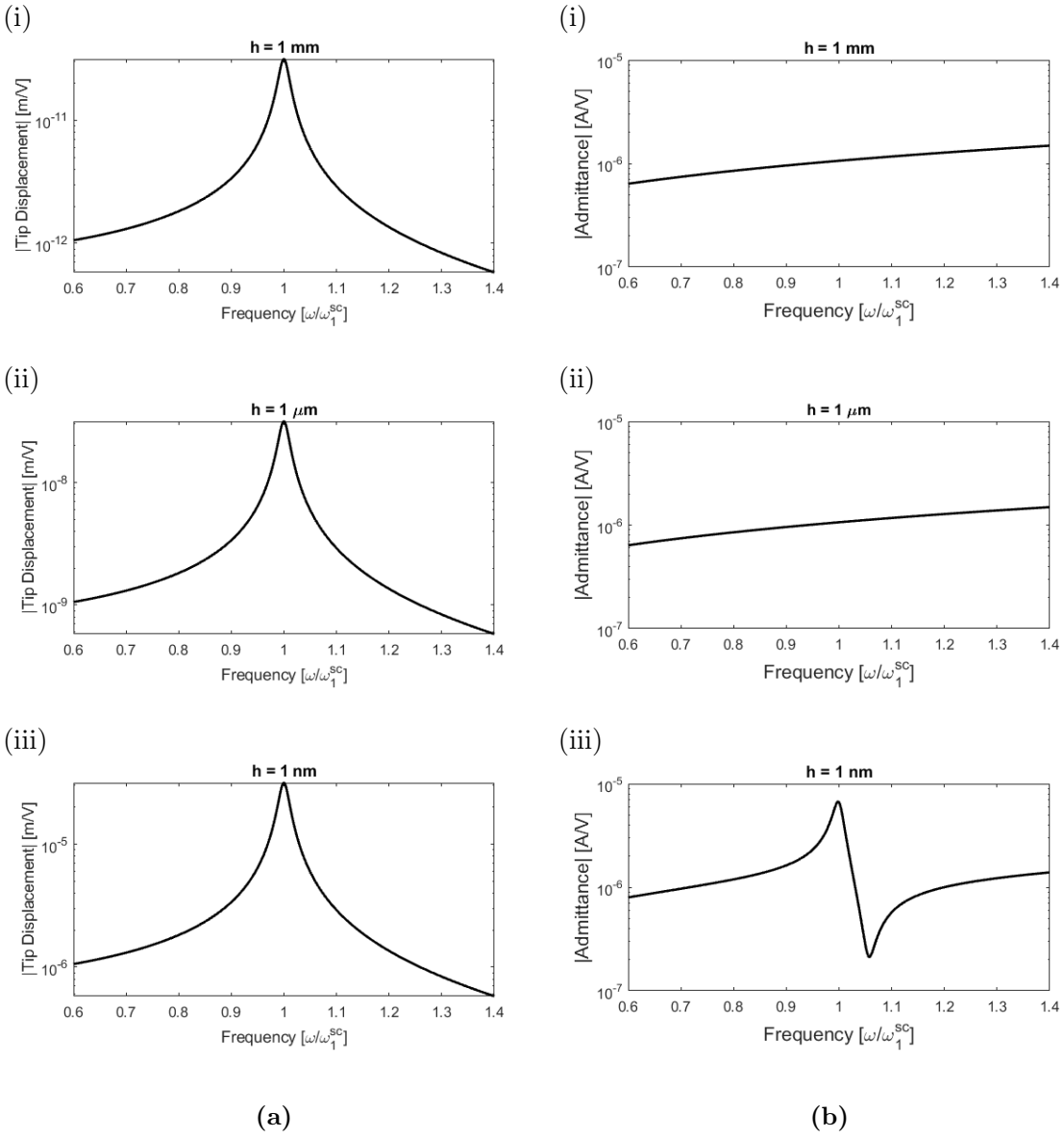

Figure 11: **(a)** Tip displacement and **(b)** admittance frequency response functions (in magnitude form) for actuation of cantilevered STO with a fixed aspect ratio of 100/5/1 ($L/b/h$) for three different geometric scales with the following thickness (h) values: (i) 1 mm, (ii) 1 μm, and (iii) 1 nm.

continuous surface electrodes are employed. However, the model can be employed for higher vibration modes, segmented electrodes, as well as other deterministic or random mechanical excitation forms.

The transverse mode flexoelectric coupling coefficient, k, (as a direct and compact measure of energy conversion) is analytically extracted from the short- and open-circuit natural frequencies. Dependence of the coupling coefficient on the thickness and material parameters

(figure of merit) is discussed in detail. The flexoelectric energy conversion and harvesting become significant only at nm thickness levels for typical flexoelectric coefficients obtained from atomistic simulations (with order of magnitude 10^{-9} C/m). For instance, the negligible flexoelectric coupling of an STO cantilever at the mm thickness level increases by 6 orders of magnitude (from $k \approx 3.5 \times 10^{-7}$ to $k \approx 0.33$) when the thickness is reduced to nm-level.

Substantially high values of flexoelectric coefficients (10^{-4} C/m) reported in the literature based on experiments conducted with mm-thick samples result in extremely high values of the coupling coefficient, yielding values nearly unity for all submicron thickness levels, and therefore suggesting very high energy conversion even at μm thickness level, which is not the case in reality. This observation confirms that the identified constants for certain mm-thick samples probably do not represent bulk flexoelectricity and are not valid at other scales (and cannot be used in the proposed model). Overall the framework given in this chapter is suitable for modeling and analysis of centrosymmetric dielectric materials (such as STO) and structural configurations that are flexoelectric but not piezoelectric. The next chapter considers the combination of piezoelectricity with flexoelectricity for non-centrosymmetric settings.

CHAPTER III

FLEXOELECTRIC-PIEZOELECTRIC BIMORPH CANTILEVER MODEL FOR BENDING VIBRATIONS

3.1 Introduction

In this chapter, we establish and explore a complete analytical framework based on Eqs. 4 and 5 by accounting for both the flexoelectric and piezoelectric effects. The focus is placed on the development of governing electro-elastodynamic flexoelectric-piezoelectric equations for the problems of energy harvesting, sensing, and actuation. The coupled governing equations are analyzed to obtain the frequency response functions such as the voltage output across the electrical load per base acceleration (in case of mechanical excitation) or electromechanical admittance in dynamic actuation (in case of electrical excitation). Furthermore, the coupling coefficient for the bimorph configuration is identified and its size dependence is explored.

3.2 Flexoelectric-piezoelectric Euler-Bernoulli beam model for energy harvesting and actuation

Figure 12 shows bimorph piezoelectric cantilevers under transverse base excitation for energy harvesting from bending vibrations (Fig. 12a) and under dynamic voltage actuation to create dynamic bending deformation (Fig. 12b). In the following, we formulate these two problems for series connected piezoelectric layers (assuming oppositely poled layers) by accounting for both flexoelectricity and piezoelectricity. The direct and converse effects are defined as given by Eqs. 4 and 5 in Chapter 1. Specifically we obtain the voltage output and vibration response frequency response functions (FRFs) in the energy harvesting problem, and vibration response and electromechanical admittance FRFs in the actuation problem in closed form to use in simulations of the next section.

Following an electromechanical modal analysis procedure similar to the one in Chapter 2 for an Euler Bernoulli beam, the governing equations for the forced vibration of a uniform

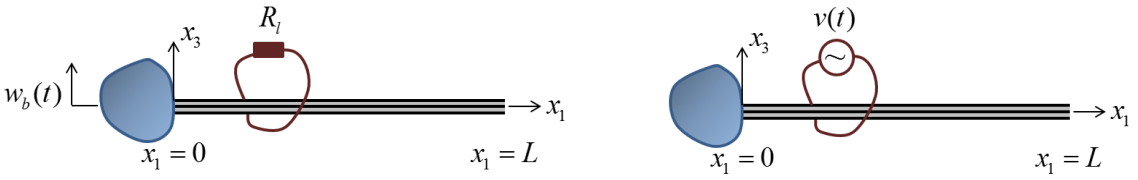

Figure 12: Bimorph cantilevers undergoing bending vibrations (exhibiting combined flexoelectric and piezoelectric effects at very small thickness levels): **(a)** Energy harvesting/sensing in response to mechanical excitation; **(b)** shape morphing or dynamic actuation under electrical excitation

bimorph cantilever under base excitation in modal coordinates can be obtained as

$$\frac{d^2\eta_r(t)}{dt^2} + 2\zeta_r\omega_r\frac{d\eta_r(t)}{dt} + {\omega_r}^2\eta_r(t) - \theta_r v(t) = f_r(t) \tag{50}$$

where ω_r is the natural frequency of the r-th vibration mode in short circuit, ζ_r is the damping ratio of r-th vibration mode. The modal electromechanical coupling term is

$$\theta_r = (\tfrac{1}{2}e_{311}bh_p + \mu_{1133}b)\left.\frac{d\phi(x_1)}{dx_1}\right|_{x_1=L} \tag{51}$$

and the mechanical forcing function can be expressed as $f_r(t) = -m\frac{d^2w_b(t)}{dt^2}\int_0^L \phi_r(x_1)dx_1$.

The coupled electrical circuit equation for series connection of the bimorph layers is

$$\frac{C_p}{2}\frac{dv(t)}{dt} + \frac{v(t)}{R_l} + \sum_{r=1}^{\infty}\theta_r\frac{d\eta_r(t)}{dt} = 0 \tag{52}$$

where the internal capacitance of the bimorph (for each layer) is $C_p = \frac{\varepsilon_{33}bL}{h_p}$. Note that both the flexoelectric and piezoelectric coupling terms exhibit symmetry in the mechanical force balance and electrical current balance equations.

The equivalent electromechanical equations governing the modal mechanical and voltage response of a bimorph can be given by

$$\frac{d^2\eta_r(t)}{dt^2} + 2\zeta_r\omega_r\frac{d\eta_r(t)}{dt} + \omega_r^2\eta_r(t) - \theta_r v(t) = f_r(t) \tag{53}$$

$$C\frac{dv(t)}{dt} + \frac{v(t)}{R_l} + \sum_{r=1}^{\infty}\theta_r\frac{d\eta_r(t)}{dt} = 0 \tag{54}$$

where the equivalent capacitance is $C = C_p/2$.

In the voltage actuation problem ($f_r(t) = 0$, i.e. for a fixed base), Eqs. 53 and 54 become

$$\frac{d^2\eta_r(t)}{dt^2} + 2\zeta_r\omega_r\frac{d\eta_r(t)}{dt} + {\omega_r}^2\eta_r(t) = \theta_r v(t) \tag{55}$$

$$i(t) = C\frac{dv(t)}{dt} + \sum_{r=1}^{\infty}\theta_r\frac{d\eta_r(t)}{dt} \tag{56}$$

where $i(t)$ is the electric current input associated with the dynamic actuation.

3.3 Electromechanical frequency response at steady state

3.3.1 Voltage and vibration response for energy harvesting

For harmonic base excitation, the steady state modal mechanical response of the beam and the steady state voltage response across the resistive load are also harmonic at the same frequency. The steady-state voltage response is obtained as

$$v(t) = \frac{\sum_{r=1}^{\infty}\frac{-j\omega\theta_r F_r}{\omega_r^2-\omega^2+j2\zeta_r\omega_r\omega}}{\frac{1}{R_l} + j\omega C + \sum_{r=1}^{\infty}\frac{j\omega{\theta_r}^2}{\omega_r^2-\omega^2+j2\zeta_r\omega_r\omega}}e^{j\omega t} \tag{57}$$

The steady-state mechanical response of the beam (that accounts for the converse flexo-electric-piezoelectric effect) is

$$w_{rel}(x_1,t) = \sum_{r=1}^{\infty}\left[\left(F_r - \theta_r\frac{\sum_{r=1}^{\infty}\frac{j\omega\theta_r F_r}{\omega_r^2-\omega^2+j2\zeta_r\omega_r\omega}}{\frac{1}{R_l} + j\omega C + \sum_{r=1}^{\infty}\frac{j\omega{\theta_r}^2}{\omega_r^2-\omega^2+j2\zeta_r\omega_r\omega}}\right)\frac{\phi_r(x_1)e^{j\omega t}}{\omega_r^2-\omega^2+j2\zeta_r\omega_r\omega}\right] \tag{58}$$

3.3.2 Vibration response and current drawn for actuation

The governing equations in energy harvesting can be modified to represent the actuation problem similarly, such that there is no base excitation ($f_r(t) = 0$) and the excitation is due to harmonic voltage input as given by Eqs. 55 and 56. The steady state mechanical response and current are obtained as

$$w_{rel}(x_1,t) = \sum_{r=1}^{\infty}\frac{\theta_r\phi_r(x_1)}{\omega_r^2-\omega^2+j2\zeta_r\omega_r\omega}Ve^{j\omega t} \tag{59}$$

$$i(t) = j\omega\left(C + \sum_{r=1}^{\infty}\frac{\theta_r^2}{\omega_r^2-\omega^2+j2\zeta_r\omega_r\omega}\right)Ve^{j\omega t} \tag{60}$$

3.4 Size effects on modal electromechanical coupling coefficient

Using the dynamic (resonant) definition of the modal electromechanical coupling coefficient based on the difference between the open-circuit and short-circuit natural frequencies given by Eq. 43 in Chapter 2, the expression for the *flexoelectric-piezoelectric coupling coefficient* for the r-th vibration mode is found to be

$$k^2 = \frac{1}{\frac{4c_{1111}^E \varepsilon_{33}}{3\alpha_r^2 (e_{311}+4\mu_{1133}/h\,)^2} + 1} \tag{61}$$

where $\alpha_r = -\sin(\lambda_r) - \sinh(\lambda_r) + \sigma_r\,(\cos(\lambda_r) - \cosh(\lambda_r))$ and $h = 2h_p$. Equation 61 clearly captures the thickness dependence of the flexoelectric effect and shows that with decreased thickness (h), the coupling coefficient (k) increases. Expectedly, the piezoelectric term has no size-dependence. This equation also shows the effect of material properties on the coupling coefficient and gives insight into the sign of the flexoelectric constant (μ_{1133}), which has varied from experimental and atomistic simulations [60]. Equation 61 shows that the flexoelectric and piezoelectric constants should have the same sign to prevent cancellation (and division by zero) at a particular thickness.

3.5 Case studies and results

In this section, simulations are performed to show the effect of thickness on the electromechanical coupling and the frequency response behavrior of a uniform bimorph cantileverd beam for energy harvesting and actuation. The simulations in this section are for Barium Titanate (BTO) using the atomistic value presented by Maranganti and Sharma [60] of $\mu_{1133} = -5.463 \times 10^{-9}$ C/m along with the necessary material properties [8]: $e_{311} = -4.4$ C/m^2, $c_{1111}^E = 166$ GPa, $\varepsilon_{33}^s = 12.56$ nF/m, and $\rho = 5720$ kg/m^3.

3.5.1 Electromechanical coupling and size effects

The electromechanical coupling coefficient due to combined flexoelectric and piezoelectric energy conversion is plotted for a range of cantilever thicknesses in Fig. 13. The focus is placed on the fundamental bending vibration mode ($r = 1$), and the beam thicknesses in the simulations range from 1 mm to 1 nm. As stated previously based on Eq. 61, the

coupling coefficient increases with decreased thickness and is illustrated graphically in Fig. 13. The isolated flexoelectric and piezoelectric coupling coefficients are also shown in Fig. 13 and it is seen that only submicron scale (mainly below ~ 100 nm) does the flexoelectric effect become appreciable, and it strongly enhances the overall electromechanical coupling. For micron thickness and above the overall electromechanical coupling is merely due to bulk piezoelectricity; however, the electromechanical coupling is dramatically enhanced due to flexoelectricity for thickness levels approaching the nanoscale.

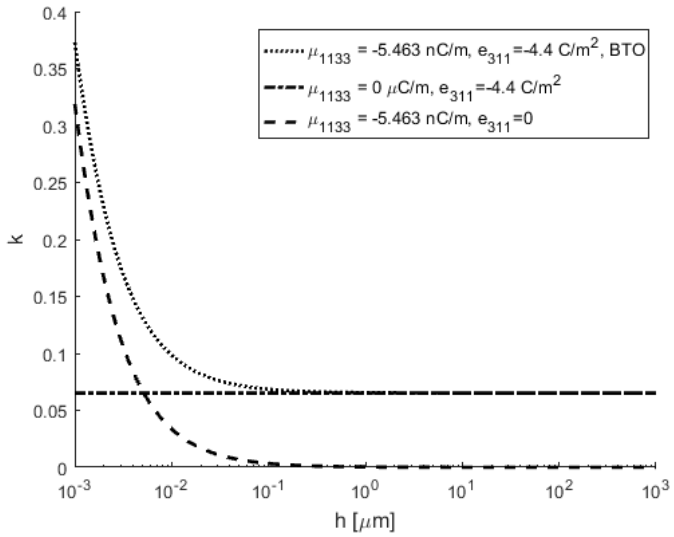

Figure 13: Transverse mode coupling coefficient (k) vs. bimorph thickness (h) for BTO cantilever for combined flexoelectric and piezoelectric effects, piezoelectric effect only, and flexoelectric effect only (by employing the atomistic flexoelectric constant value calculated by Maranganti and Sharma [60])

3.5.2 Electromechanical frequency response in energy harvesting

The electromechanical frequency response behavior of a bimorph cantilevered flexoelectric and piezoelectric energy harvester under base excitation is simulated with a focus on the first bending mode ($r = 1$) for a range of electrical load resistive values. Three different geometric scales are explored ranging from mm-scale to nm-scale. For each case, the length/width/total thickness aspect ratio was fixed at 100/5/1. The bimorph is made of BTO and has perfectly conductive surface electrodes on the faces that are perpendicular to the transverse base excitation. A mechanical quality factor (Q) of 50 is assumed, yielding

an approximate modal mechanical damping ratio of 1% of the critical damping. Three cases with total thicknesses (h) of 1 mm, 1 μm, and 1 nm (thickness of one layer of the bimorph is $h_p = h/2$) are analyzed while keeping the aspect ratio of $L/b/h$ fixed at 100/5/1. The mechanical excitation is harmonic base acceleration, $d^2w_b(t)/dt^2 = -\omega^2 W_0 e^{j\omega t}$. The results are presented as frequency response magnitude maps normalized by the base acceleration quantified in terms of gravitational acceleration as in the previous chapter. To capture optimal load in power generation and respective trends with changing load, a range of electrical resistive load values spanning from short- to open-circuit conditions (100 Ω to 1 GΩ) are simulated for each case.

The voltage output (per base acceleration) frequency response map for the 1 mm-thick BTO bimorph (100mm x 5mm x 1mm) is shown in Fig. 14a.i. With increased electrical load resistance, the voltage increases monotonically at all frequencies, as a typical trend in energy harvesting [37]. It is shown that the resonance frequency for the 1 mm-thick BTO cantilever is unaffected by the change in resistive load, i.e. the frequency of peak magnitude does not change as the electrical load resistance value is swept from short- to open-circuit conditions. This indicates very low electromechanical coupling such that the feedback in the mechanical domain due to induced low voltage is negligible. The combined flexoelectric-piezoelectric coupling coefficient for the 1 mm thickness level and BTO material property combination is obtained from Eq. 61 or Fig. 13 as $k \approx 0.0652$ (which is roughly the bulk piezoelectric value) confirming negligible contribution from flexoelectricity. The beam thickness is then decreased to 1 μm while keeping the same aspect ratio (i.e. the dimensions are now 100 μm x 5 μm x 1 μm). The voltage output frequency response map for this case is shown in Fig. 14a.ii. As with the 1 mm thickness case, the 1 μm-thick BTO bimorph shows no noticeable shift in the fundamental resonance frequency with changing load resistance. The combined flexoelectric-piezoelectric coupling coefficient for this case is $k \approx 0.0655$, which again, indicates negligible flexoelectric contribution. The beam thickness is further decreased to 1 nm (beam dimensions of 100 nm x 5 nm x 1nm) and the analysis is repeated. The nm-thick bimorph exhibits a shift in resonance from short- to open-circuit conditions as shown in Fig. 14a.iii. This shows significant electromechanical coupling as

confirmed by the combined flexoelectric-piezoelectric coupling coefficient of $k \approx 0.365$ and Fig. 13.

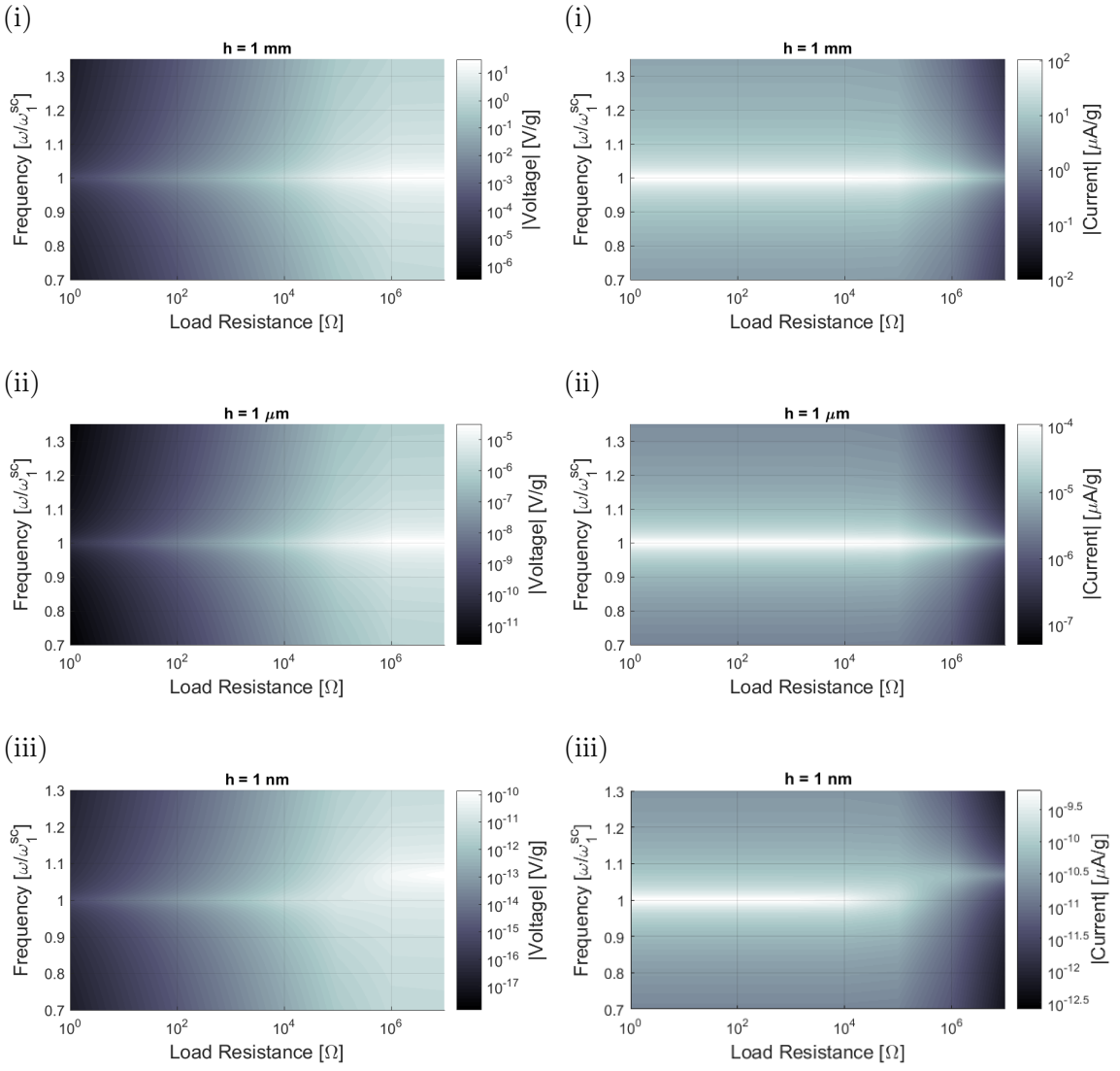

(a) **(b)**

Figure 14: **(a)** Voltage output frequency response vs. load resistance maps (in magnitude form and per base acceleration) and **(b)** current output frequency response vs. load resistance maps (in magnitude form and per base acceleration) for cantilevered BTO harvesters with a fixed aspect ratio of 100/5/1 ($L/b/h$) for three different geometric scales with the following thickness (h) values: (i) 1 mm, (ii) 1 μm, and (iii) 1 nm.

The electric current flowing to the resistive load is simply obtained from the voltage output using Ohms law. The current output (per base acceleration) frequency response maps are also generated for the BTO bimorph for each geometric scale as shown in Fig. 14b.

The electrical current output decreases with increased electrical load resistance, which is the opposite trend as compared to voltage output. At all frequencies, the maximum current is achieved under short-circuit conditions of the surface electrodes. As with the voltage output frequency response maps, similar trends are observed for each case study in terms of the coupling coefficient. The thickness levels of 1 mm and 1 μm show no noticeable shift in resonance frequency (Figs. 14b.i and 14b.ii), indicating low electromechanical coupling. The 1 nm thickness case shows significant frequency shift (Fig. 14b.iii), revealing strong electromechanical coupling as discussed previously for the voltage output, as a result of flexoelectric contribution.

The electrical power output is calculated for each of the three geometric scales and fixed aspect ratio. The resulting graphs are shown in Fig. 15a. The optimal load for peak power output can be determined for each case from the power output frequency response maps. Both the 1 mm and 1 μm-thick harvesters result in a peak power output around 100 kΩ (Figs. 15a.i and 15a.ii). The power output frequency response maps for 1mm and 1 μm thick cases show the resonance frequency to be insensitive to the resistive load due to very low electromechanical coupling. Consequently, a single optimal load is observed in the power map for the fundamental vibration mode for each case. However, the 1 nm-thick harvester exhibits two peak values for two distinct optimal electrical loads, 100 kΩ and 1 MΩ, respectively, at the short-circuit and open-circuit frequencies, yielding the same power output (Fig.15a.iii) . This is an indication of a relatively strongly coupled harvester configuration, the majority of which is due to flexoelectricity.

Finally, it is of interest to explore the structural response of the BTO bimorph while generating electricity from strain (piezoelectric effect) and strain gradient (flexoelectric effect) fluctuations in response to mechanical base excitation. The motion of the cantilever is evaluated at the tip ($x_1 = L$) using Eq. 58. Figure 15b shows the tip displacement maps for all three geometric scales of the bimorph using the same load resistances and normalized excitation frequency range. For the 1 mm-thick and 1 μm-thick bimorphs, the vibration response of the cantilever is insensitive to change in electrical load resistance, again, showing low electromechanical coupling (bulk piezoelectric value of BTO) at these

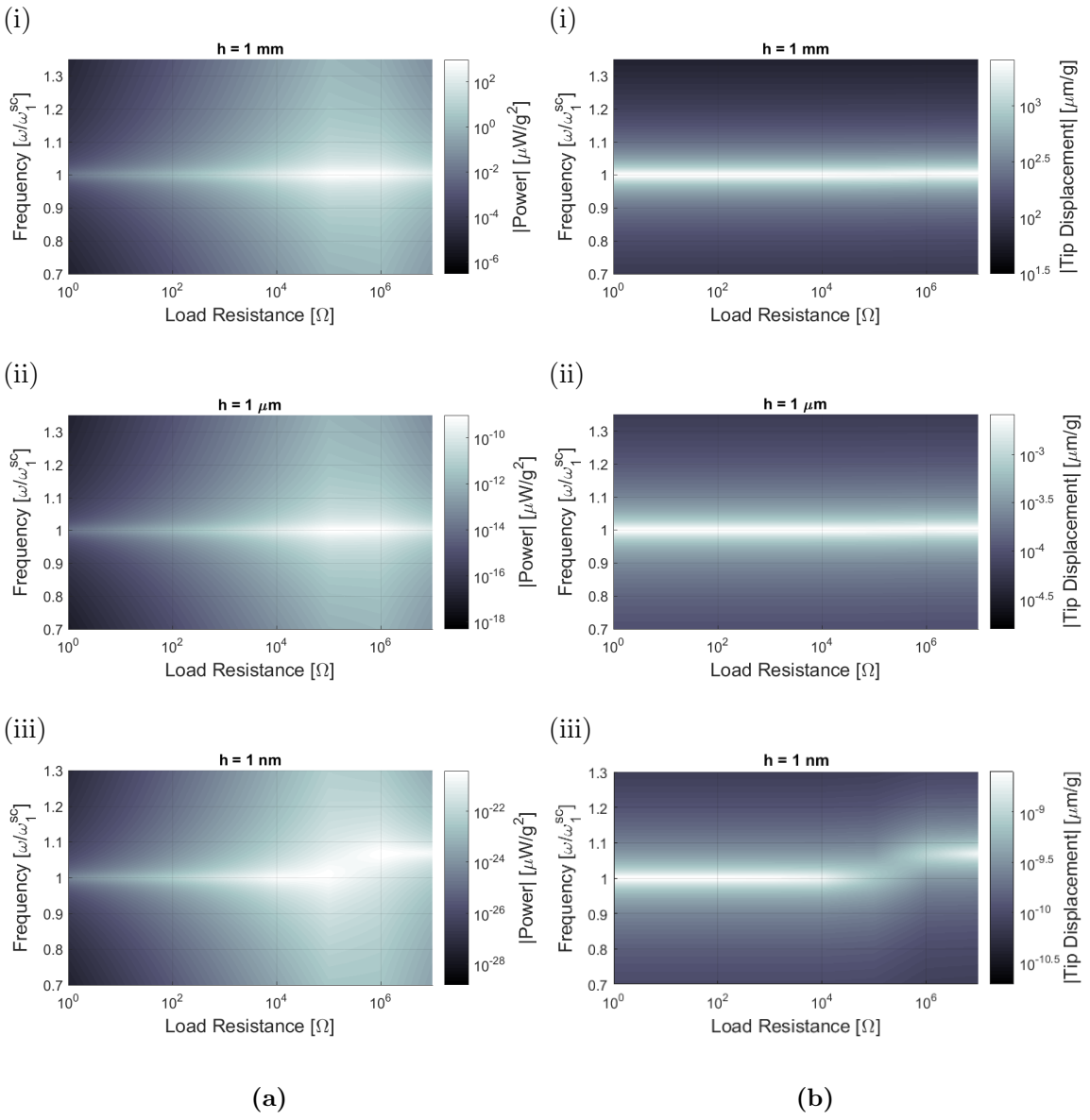

Figure 15: **(a)** Power output frequency response vs. load resistance maps (in magnitude form and per base acceleration squared) and **(b)** tip displacement frequency response vs. load resistance maps (in magnitude form and per base acceleration) for cantilevered BTO harvesters with a fixed aspect ratio of 100/5/1 ($L/b/h$) for three different geometric scales with the following thickness (h) values: (i) 1 mm, (ii) 1 μm, and (iii) 1 nm.

thickness levels (Figs. 15b.i and 15b.ii). Therefore, as a result of weak electromechanical coupling, variation in the resistive load does not create any significant dissipation in the vibration response of the BTO bimorph. However, for the bimorph with 1 nm thickness, the electromechanical coupling is much stronger, as seen from previous power output graphs, and therefore, mechanical to electrical energy conversion is rather significant. Consequently,

the structural response of the bimorph is sensitive to changing the electrical resistive load, as seen in Fig. 15b.iii, near the resonant frequency. Certain load resistance values result in significant shunt damping due to strong converse coupling.

3.5.3 Electromechanical frequency response in actuation

The same modeling framework is used to understand the electromechanical response of the bimorphs in the case of electrical excitation for the same set of system parameters. Of interest, is the tip displacement frequency response (structural response for unit actuation voltage input) from Eq. 59 and the admittance frequency response (amount of current drawn for unit actuation voltage input) calculated from Eq. 60. The tip displacement and admittance frequency responses are shown in Figs. 16a and 16b, respectively. Particularly, in the admittance plots, the percentage difference between the resonance and antiresonance frequencies is a measure of electromechanical coupling, and it increases substantially for the nm thickness level due to flexoelectric contribution to electromechanical coupling.

3.6 Conclusions

An electromechanical framework is developed and analyzed for combined transverse mode flexoelectric and piezoelectric energy harvesting from the bending vibration of piezoceramic bimorph accounting for two-way electromechanical coupling. The modeling framework is based on the Euler-Bernoulli beam theory and properly accounts for thermodynamically consistent, symmetric, direct and converse coupling terms, and it captures the size effect on the combined flexoelectric-piezoelectric coupling coefficient. Based on a modal analysis procedure, closed-form solutions of the electromechanical frequency response functions are presented along with various case studies for a broad range of geometric parameters. Thickness dependence of the electromechanical coupling (which is a measure of energy conversion) is analytically extracted and its size dependence is observed also in simulations of the electromechanical frequency response functions. The flexoelectric-piezoelectric coupling increases from the bulk piezoelectric value of $k \approx 0.0652$ at the mm-scale to $k \approx 0.365$ at the nm-scale owing to flexoelectric contribution. Overall, since the coupling coefficient is thickness dependent, the energy conversion dramatically increases in submicron thickness

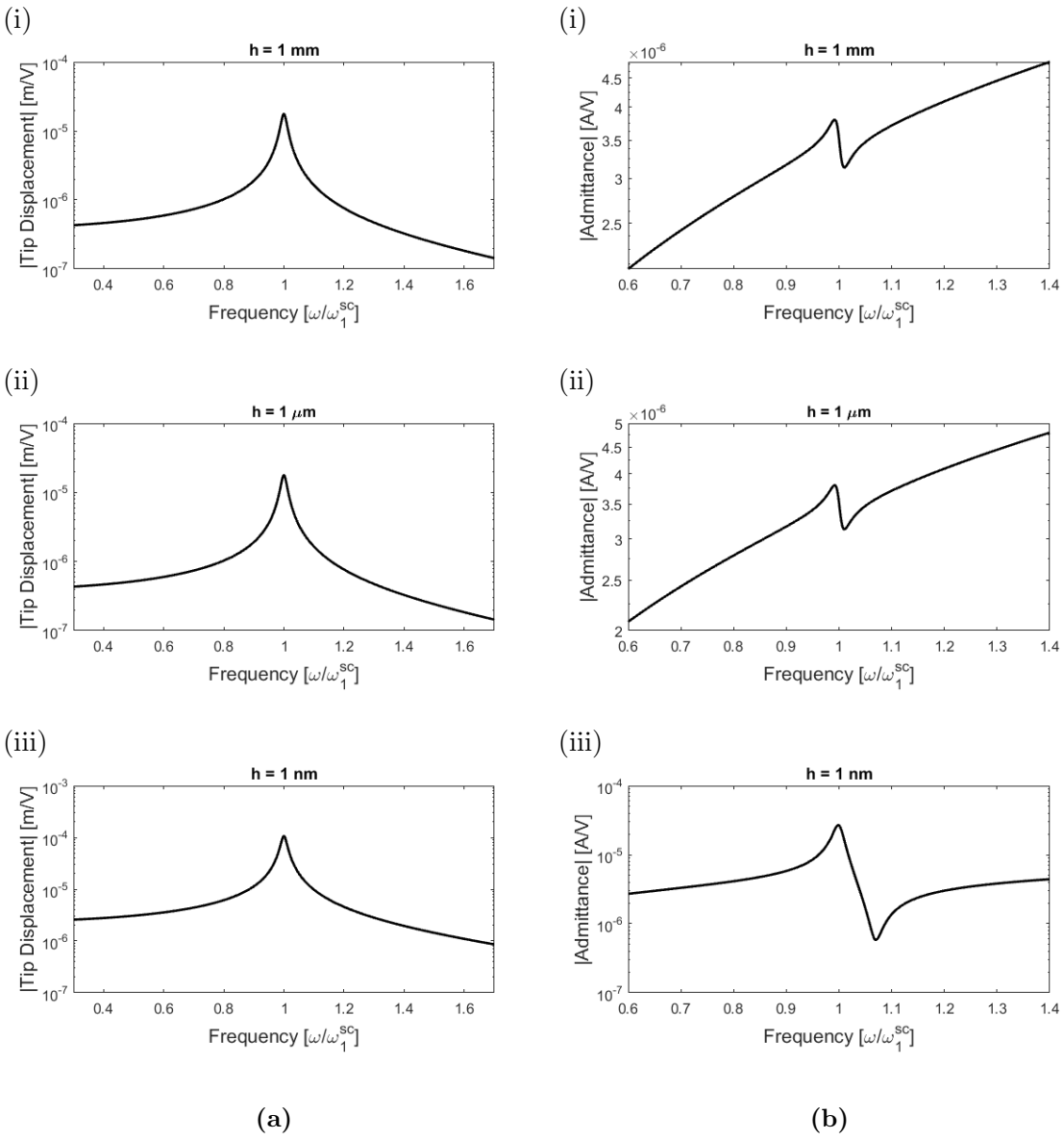

Figure 16: **(a)** Tip displacement and **(b)** admittance frequency response functions (in magnitude form) for actuation of bimorph cantilevered BTO with a fixed aspect ratio of 100/5/1 ($L/b/h$) for three different geometric scales with the following thickness (h) values: (i) 1 mm, (ii) 1 μm, and (iii) 1 nm.

levels due to the flexoelectric effect. The proposed model can be used for parameter identification as well as performance quantification and optimization in combined flexoelectric and piezoelectric energy harvesting. The model was also implemented for dynamic actuation, which could be of interest for next-generation NEMS concepts involving actuation for nanocantilevers with submicron thickness levels.

CHAPTER IV

EFFECT OF VARYING CROSS-SECTION ON RESONANT BENDING VIBRATIONS

4.1 Introduction

In this chapter, we aim to develop the governing electroelastodynamic flexoelectric and flexoelectric-piezoelectric equations for a bimorph cantilever with varying cross-sectional widths for energy harvesting and actuation. For non-uniform cross-sections, the exact solution is not available; therefore, an energy formulation is used to derive the electromechanical Lagrange's equations based on the extended Hamilton's principle. The coupled governing equations are analyzed to obtain the frequency response functions and study the effects of various axial geometry profiles on the electromechanical coupling for both energy harvesting (mechanical base excitation) and dynamic actuation (electrical excitation). The effects of the axial strain gradient are also studied for a flexoelectric bimorph cantilever by simulating the frequency response behavior for various cross-sectional profiles.

4.2 Flexoelectric bimorph with varying cross-section and axial strain gradient

First we consider the problem of a centrosymmetric thin bimorph cantilever for linear bending vibrations (Fig. 17). Chapters 2 and 3 showed that flexoelectricity is only significant at the nanoscale and flexoelectricity yields enhanced electromechanical coupling in nanocantilevers due to gradient effects. In the following, we formulate this problem assuming each layer is connected to a resistive load to study the effects of the axial strain gradient and the effects of varying width on the flexoelectric behavior. For arbitrary cross-sections, the problem has no exact solution unlike the uniform cross-section cases of Chapters 2 and 3.

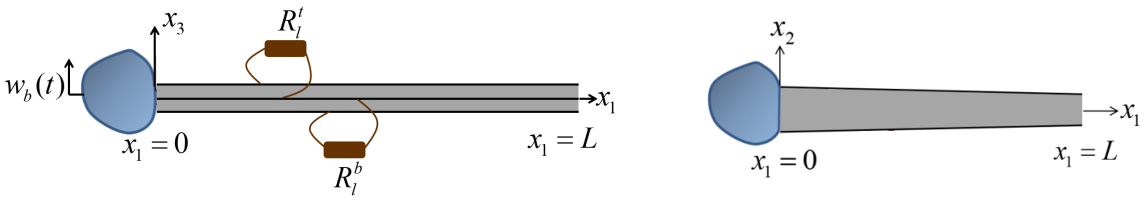

(a) **(b)**

Figure 17: (a) Bimorph flexoelectric cantilever undergoing bending vibrations for energy harvesting/sensing (each layer individually connected to a resistive load) in response to mechanical excitation; **(b)** top view of bimorph with varying cross-sectional width

4.2.1 Electromechanical Lagrange's equations based on the extended Hamilton's principle

In the absence of mechanical dissipative effects, the extended Hamilton's principle with the internal electrical energy is

$$\int_{t_1}^{t_2} (\delta T - \delta U + \delta W_{ie} + \delta W_{nc}) dt = 0 \tag{62}$$

where δT, δU, and δW_{ie} are the first variations of the total kinetic energy, the total potential energy, and the internal electrical energy while δW_{nc} is the virtual work of the non-conservative mechanical force and electrical charge components.

For consideration of the base excitation effect in the kinetic energy, the mechanical damping is to be introduced later. The only non-conservative virtual work is due to the electric charge output $(Q(t))$

$$\delta W_{nc} = \delta W_{nce} = Q(t)\delta v(t) \tag{63}$$

The total potential energy in the structure is

$$U = \frac{1}{2} \int_V S_{11} T_{11} dV \tag{64}$$

where S_{11} is the axial strain (given by Eq. 12), T_{11} is the axial stress due to bending (given by Eq. 4), and the integral is performed over the volume of the material. The total kinetic energy of the system can be given by

$$T = \frac{1}{2} \int_V \rho \frac{\partial \mathbf{u}_m^T}{\partial t} \frac{\partial \mathbf{u}_m}{\partial t} dV \tag{65}$$

where ρ is the mass density of the material, the superscript T indicates the transpose, and $\mathbf{u_m}$ is the modified displacement vector that is the superposition of the base displacement input and the beam displacement and is given as

$$\mathbf{u}_m = [0\ 0\ w_{rel}(x_1,t) + w_b(x_1,t)]^T \tag{66}$$

The internal electrical energy in the material is

$$W_{ie} = \frac{1}{2}\int_V E_3 D_3 dV \tag{67}$$

where E_3 is the electric field and D_3 is the electric displacement.

The constitutive equation for the stress component and the electric displacement to include the axial strain gradient $\left(\frac{\partial S_{11}}{\partial x_1}\right)$ in the flexoelectric material are

$$T_{11} = c_{1111} S_{11} + f_{1133}\frac{\partial P_3}{\partial x_3} \tag{68}$$

$$D_3 = \varepsilon_{33} E_3 + \mu_{1133}\frac{\partial S_{11}}{\partial x_3} + \mu_{1111}\frac{\partial S_{11}}{\partial x_1} \tag{69}$$

where μ_{1111} is the axial flexoelectric coefficient and recall the axial strain is $S_{11}(x_1, x_3, t) = -x_3\frac{\partial^2 w_{rel}(x_1,t)}{\partial {x_1}^2}$.

Evaluating Eqs. 64, 65, and 67, the total potential, kinetic and internal electrical energies are

$$U = \frac{1}{2}\int_0^L \left[c_{1111} I(x_1)\left(\frac{\partial^2 w_{rel}(x_1,t)}{\partial {x_1}^2}\right)^2 - b(x_1)\mu_{1133}\left(v_t(t) + v_b(t)\right)\frac{\partial^2 w_{rel}(x_1,t)}{\partial {x_1}^2}\right] dx_1 \tag{70}$$

$$T = \frac{1}{2}\int_0^L \rho A(x_1)\left[\left(\frac{\partial w_{rel}(x_1,t)}{\partial t}\right)^2 + 2\frac{\partial w_{rel}(x_1,t)}{\partial t}\frac{\partial w_b(x_1,t)}{\partial t} + \left(\frac{\partial w_b(x_1,t)}{\partial t}\right)^2\right] dx_1 \tag{71}$$

$$\begin{aligned} W_{ie} = \frac{1}{2}\int_0^L \Bigg[& b(x_1)\mu_{1133}\left(v_t(t) + v_b(t)\right)\frac{\partial^2 w_{rel}(x_1,t)}{\partial x_1^2} \\ & + \frac{1}{2} b(x_1)\mu_{1111} h\left(v_t(t) - v_b(t)\right)\frac{\partial^3 w_{rel}(x_1,t)}{\partial x_1^3}\Bigg] dx_1 + \frac{1}{2} C_b {v_b}^2(t) + \frac{1}{2} C_t {v_t}^2(t) \end{aligned} \tag{72}$$

where v_t and v_b is the voltage in the top and bottom layers, respectively. The zeroth and second moments of area for the cross section at an arbitrary point (x_1) are given as

$$\begin{aligned} A(x_1) &= \iint_S 1 \; dx_2 dx_3 \\ I(x_1) &= \iint_S x_3^2 \; dx_2 dx_3 \end{aligned} \tag{73}$$

The capacitance in each layer is

$$\begin{aligned} C_t &= \frac{\varepsilon_{33}}{h} \int_0^L b(x_1) dx_1 \\ C_b &= \frac{\varepsilon_{33}}{h} \int_0^L b(x_1) dx_1 \end{aligned} \tag{74}$$

Following the method of assumed modes for an electromechanical system [34], the components of the extended Hamilton's principle are discretized. The distributed parameter in the mechanical domain is $w_{rel}(x_1, t)$ while the electrical variable is $v(t)$. Let the vibration response be represented by the finite series expansion:

$$w_{rel}(x_1, t) = \sum_{r=1}^{N} a_r(t) \phi_r(x_1) \tag{75}$$

where $\phi_r(x_1)$ is the kinematically admissible trial functions which satisfy the respective essential boundary conditions (at the fixed end for a cantilever), $a_r(t)$ is the unknown generalized coordinates, and N is the number of modes considered in the solution.

The electromechanical Lagrange's equations based on the extended Hamilton's principle given by Eq. 62 are

$$\frac{d}{dt}\left(\frac{\partial T}{\partial \dot{a}_i}\right) - \frac{\partial T}{\partial a_i} + \frac{\partial U}{\partial a_i} - \frac{\partial W_{ie}}{\partial a_i} = 0 \tag{76}$$

$$\frac{d}{dt}\left(\frac{\partial T}{\partial \dot{v}_t}\right) - \frac{\partial T}{\partial v_t} + \frac{\partial U}{\partial v_t} - \frac{\partial W_{ie}}{\partial v_t} = Q_t \tag{77}$$

$$\frac{d}{dt}\left(\frac{\partial T}{\partial \dot{v}_b}\right) - \frac{\partial T}{\partial v_b} + \frac{\partial U}{\partial v_b} - \frac{\partial W_{ie}}{\partial v_b} = Q_b \tag{78}$$

where Q_t and Q_b are the electric charge outputs of each flexoelectric layer.

4.2.2 Voltage and vibration response for energy harvesting

The resulting Lagrange equation for the generalized coordinate a_i in matrix form is

$$\mathbf{m\ddot{a}} + \mathbf{d\dot{a}} + \mathbf{ka} - \tilde{\boldsymbol{\theta}}^{\mathbf{t}} v_t - \tilde{\boldsymbol{\theta}}^{\mathbf{b}} v_b = \mathbf{f} \tag{79}$$

where the damping matrix is $\mathbf{d} = \mu\mathbf{m} + \gamma\mathbf{k}$. Here, μ and γ are the constants of mass and stiffness proportionality, respectively.

The Lagrange equations for the voltage in each layer are

$$C_t \dot{v}_t + \frac{v_t}{{R_l}^t} + \left(\tilde{\boldsymbol{\theta}}^{\mathbf{t}}\right)^T \dot{\mathbf{a}} = 0 \tag{80}$$

$$C_b \dot{v}_b + \frac{v_b}{{R_l}^b} + \left(\tilde{\boldsymbol{\theta}}^{\mathbf{b}}\right)^T \dot{\mathbf{a}} = 0 \tag{81}$$

The $N \times 1$ vector of generalized coordinates is $\mathbf{a} = [a_1 \ a_2 \ . \ . \ . \ a_N]^T$ and the $N \times 1$ vectors of electromechanical coupling in the top and bottom layers are $\tilde{\boldsymbol{\theta}}^{\mathbf{t}} = \left[\tilde{\theta}_1^t \ \tilde{\theta}_2^t \ . \ . \ . \ \tilde{\theta}_N^t\right]^T$ and $\tilde{\boldsymbol{\theta}}^{\mathbf{b}} = \left[\tilde{\theta}_1^b \ \tilde{\theta}_2^b \ . \ . \ . \ \tilde{\theta}_N^b\right]^T$, respectively with elements given by

$$\tilde{\theta}_r^t = \mu_{1133} \int_0^L b(x_1)\phi_r^{''}(x_1)dx_1 + \frac{1}{4}\mu_{1111} h \int_0^L b(x_1)\phi_r^{'''}(x_1)dx_1 \tag{82}$$

$$\tilde{\theta}_r^b = \mu_{1133} \int_0^L b(x_1)\phi_r^{''}(x_1)dx_1 - \frac{1}{4}\mu_{1111} h \int_0^L b(x_1)\phi_r^{'''}(x_1)dx_1 \tag{83}$$

The mass, stiffness, and damping matrices ($\mathbf{m}$, $\mathbf{k}$, $\mathbf{d}$) are $N \times N$ matrices with elements given by

$$m_{rl} = \int_0^L \rho A(x_1)\phi_r(x_1)\phi_l(x_1)dx_1 \tag{84}$$

$$k_{rl} = \int_0^L c_{1111} I(x_1)\phi_r^{''}(x_1)\phi_l^{''}(x_1)dx_1 \tag{85}$$

and the forcing vector $\mathbf{f}$ is an $N \times 1$ vector whose elements are given by

$$f_r = -\int_0^L \rho A(x_1)\phi_r(x_1)\frac{\partial^2 w_b(x_1,t)}{\partial t^2}dx_1 \tag{86}$$

For harmonic base displacement the generalized coordinates are also harmonic at the same frequency. Solving Eqs. 79, 80, and 81 for the steady state transverse vibration and

voltage responses

$$w_{rel}(x_1,t) = \mathbf{\Phi}^T(x_1)(\mathbf{\Gamma})^{-1}\mathbf{F}e^{j\omega t} \tag{87}$$

$$v_t(t) = V_t e^{j\omega t} = j\omega\left(j\omega C_t + \frac{1}{R_l{}^t}\right)^{-1}\left[\left(-\tilde{\boldsymbol{\theta}}^{\mathbf{t}}\right)^T\mathbf{\Gamma}^{-1}\mathbf{F}e^{j\omega t}\right] \tag{88}$$

$$v_b(t) = V_b e^{j\omega t} = j\omega\left(j\omega C_b + \frac{1}{R_l{}^b}\right)^{-1}\left[\left(-\tilde{\boldsymbol{\theta}}^{\mathbf{b}}\right)^T\mathbf{\Gamma}^{-1}\mathbf{F}e^{j\omega t}\right] \tag{89}$$

where $\mathbf{\Phi}^T$ is the vectorial representations of the respectable admissible function sets $\phi_r(x_1)$ and $\mathbf{\Gamma} = \left(-\omega^2\mathbf{m} + j\omega\mathbf{d} + \mathbf{k}\right) + j\omega\left(j\omega C_t + \frac{1}{R_l{}^t}\right)^{-1}\tilde{\boldsymbol{\theta}}^{\mathbf{t}}\left(\tilde{\boldsymbol{\theta}}^{\mathbf{t}}\right)^T + j\omega\left(j\omega C_b + \frac{1}{R_l{}^b}\right)^{-1}\tilde{\boldsymbol{\theta}}^{\mathbf{b}}\left(\tilde{\boldsymbol{\theta}}^{\mathbf{b}}\right)^T$

4.3 Flexoelectric-piezoelectric bimorph with varying cross-section

Next, we consider a bimorph with varying cross-sectional width for series connected piezoelectric layers (assuming oppositely poled layers) by accounting for both flexoelectricity and piezoelectricity as shown in Fig. 18. In the following, we formulate the problems of transverse base excitation for energy harvesting from bending vibrations (Fig. 18) and under dynamic voltage actuation for a fixed base to create dynamic bending deformation in the same vein as Chapters 2 and 3 (not shown in Fig. 18). The direct and converse effects are defined as given by Eqs. 4 and 5 in Chapter 1. We obtain the voltage output and vibration response frequency response functions (FRFs) in the energy harvesting problem, and vibration response and electromechanical admittance FRFs in the actuation problem in closed form to use in simulations of the next section.

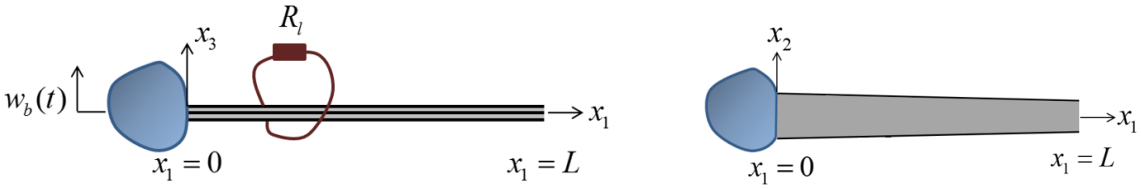

(a) **(b)**

Figure 18: (a) Bimorph cantilever undergoing bending vibrations (exhibiting combined flexoelectric and piezoelectric effects at very small thickness levels) for energy harvesting/sensing in response to mechanical excitation; **(b)** top view of bimorph with varying cross-sectional width

The electromechanical Lagrange's equations based on the extended Hamilton's principle

given by Eq. 62 are

$$\frac{d}{dt}\left(\frac{\partial T}{\partial \dot{a}_i}\right) - \frac{\partial T}{\partial a_i} + \frac{\partial U}{\partial a_i} - \frac{\partial W_{ie}}{\partial a_i} = 0 \tag{90}$$

$$\frac{d}{dt}\left(\frac{\partial T}{\partial \dot{v}}\right) - \frac{\partial T}{\partial v} + \frac{\partial U}{\partial v} - \frac{\partial W_{ie}}{\partial v} = Q \tag{91}$$

where Q is the electric charge output of the piezoceramic layer.

4.3.1 Voltage and vibration response for energy harvesting

Evaluating Eqs. 64, 65, 67 and substituting in to Eqs. 90 and 91, the first set of Lagrange's equations (for the generalized coordinate a_l) becomes

$$\mathbf{m}\ddot{\mathbf{a}} + \mathbf{d}\dot{\mathbf{a}} + \mathbf{k}\mathbf{a} - \tilde{\boldsymbol{\theta}} v = \mathbf{f} \tag{92}$$

where the damping matrix is $\mathbf{d} = \mu\mathbf{m} + \gamma\mathbf{k}$. Here μ and γ are the constants of mass and stiffness proportionality, respectively.

The second Lagrange's equation is

$$C_p\dot{v} + \frac{v}{R_l} + \left(\tilde{\boldsymbol{\theta}}\right)^T \dot{\mathbf{a}} = 0 \tag{93}$$

The $N \times 1$ vector of generalized coordinates is $\mathbf{a} = [a_1\ a_2\ .\ .\ .\ a_N]^T$ and the $N \times 1$ vector of electromechanical coupling is $\tilde{\boldsymbol{\theta}} = \left[\tilde{\theta}_1\ \tilde{\theta}_2\ .\ .\ .\ \tilde{\theta}_N\right]^T$ where

$$\tilde{\theta}_r = \int_0^L \left(\frac{1}{2} e_{311} h_p + \mu_{1133}\right) b(x_1) \phi_r''(x_1) dx_1 \tag{94}$$

The mass, stiffness and damping matrices ($\mathbf{m}$, $\mathbf{k}$, $\mathbf{d}$) are $N \times N$ matrices whose elements are given by

$$m_{rl} = \int_0^L \rho A(x_1) \phi_r(x_1) \phi_l(x_1) dx_1 \tag{95}$$

$$k_{rl} = \int_0^L c_{1111} I(x_1) \phi_r''(x_1) \phi_l''(x_1) dx_1 \tag{96}$$

and the forcing vector $\mathbf{f}$ is an $N \times 1$ vector whose elements are given by

$$f_r = -\int_0^L \rho A(x_1) \phi_r(x_1) \frac{\partial^2 w_b(x_1, t)}{\partial t^2} dx_1 \tag{97}$$

For harmonic base displacement the generalized coordinates are also harmonic at the same frequency. Solving Eqs. 92 and 93 for the steady state transverse vibration and voltage responses

$$w_{rel}(x_1,t) = \mathbf{\Phi}^T(x_1)(\mathbf{\Gamma})^{-1}\mathbf{F}e^{j\omega t} \tag{98}$$

$$v(t) = j\omega\left(j\omega C_p + \frac{1}{R_l}\right)^{-1}\left[\left(-\tilde{\boldsymbol{\theta}}\right)^T(\mathbf{\Gamma})^{-1}\mathbf{F}e^{j\omega t}\right] \tag{99}$$

where $\mathbf{\Phi}^T$ is the vectorial representations of the respectable admissible function sets $\phi_r(x_1)$ and $\mathbf{\Gamma} = \left(-\omega^2\mathbf{m} + j\omega\mathbf{d} + \mathbf{k}\right) + j\omega\left(j\omega C_p + \frac{1}{R_l}\right)^{-1}\tilde{\boldsymbol{\theta}}\left(\tilde{\boldsymbol{\theta}}\right)^T$

4.3.2 Vibration response and current drawn for actuation

The governing equations in energy harvesting (Eqs. 92 and 93) can be modified to represent the actuation problem similarly such that there is no base excitation ($f_r = 0$) and the excitation is due to harmonic voltage input, yielding

$$w_{rel}(x_1,t) = \mathbf{\Phi}^T(x_1)\left(-\omega^2\boldsymbol{m} + j\omega\boldsymbol{d} + \boldsymbol{k}\right)^{-1}\tilde{\boldsymbol{\theta}}Ve^{j\omega t} \tag{100}$$

$$i(t) = j\omega\left[C_p + \left(\tilde{\boldsymbol{\theta}}\right)^T\left(-\omega^2\boldsymbol{m} + j\omega\boldsymbol{d} + \boldsymbol{k}\right)^{-1}\tilde{\boldsymbol{\theta}}\right]Ve^{j\omega t} \tag{101}$$

4.4 Case studies and results

In this section, the electromechanical frequency response behavior of cantilevered bimorph beams are simulated with a focus on the first bending mode ($r = 1$) for a broad range of electrical load resistance values. Four different widths are explored, shown in Fig. 19, spanning from a wider tip to uniform width to a narrow tip. Damping is neglected (in all cases) to better visualize the change in electromechanical coupling (i.e. short- and open-circuit resonances, or the resonance and antiresonance in the admittance). The admissible trial functions used for all simulations is $\phi_r(x_1) = 1 - \cos\left(\frac{(2r-1)\pi x_1}{2L}\right)$. Chapters 2 and 3 showed that the flexoelectric effect is only significant at the nanoscale in Euler-Bernoulli beams; therefore, simulations will be performed at the nanoscale to study the effects of varying cross-section on flexoelectric coupling.

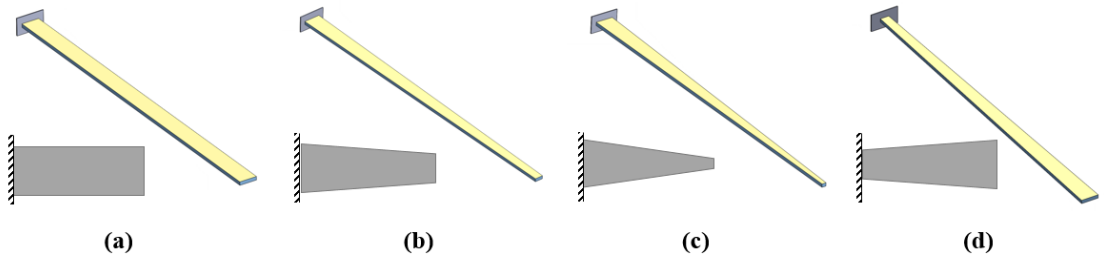

Figure 19: Schematic of bimorph cantilevered BTO harvesters with a varying cross sectional widths: **(a)** $b(x_1) = \tilde{b}$, **(b)** $b(x_1) = -\frac{\tilde{b}}{2L}x_1 + \tilde{b}$, **(c)** $b(x_1) = -\frac{3\tilde{b}}{4L}x_1 + \tilde{b}$, **(d)** $b(x_1) = \frac{\tilde{b}}{2L}x_1 + \frac{\tilde{b}}{2}$

4.4.1 Effects of axial strain gradient in bending vibrations of flexoelectric bimorph beams

First, the effect of axial strain gradient is studied by simulating the electromechanical frequency response of a cantilevered bimorph flexoelectric (and non-piezoelectric) energy harvester under base excitation. For each case the length is $L = 200$ nm, the thickness of each layer is $h = 2$ nm, and the nominal width is $\tilde{b} = 20$ nm. The cantilever is made of Strontium Titanate (STO) and has perfectly conductive surface electrodes on the faces that are perpendicular to the direction of transverse base excitation (Fig. 17). The simulations are for Strontium Titanate (STO) using the elastic [9, 44] and dielectric [89, 3] properties of $c_{1111} = 318$ GPa, $\rho = 5116$ kg/m^3, and $\varepsilon_{33} = 2.66$ nF/m (for the room temperature relative permittivity [89, 88, 3], $\varepsilon_{33}/\varepsilon_0 = 300$), and using the atomistic flexoelectric coefficient value [60] of $\mu_{1133} = -3.75 \times 10^{-9}$ C/m.

To observe the effect of the axial strain gradient term on the flexoelectric energy harvester the electrical power output for the top and bottom layers are calculated using $\left|v_t(t)/-\omega^2 W_0 e^{j\omega t}\right|^2/{R_l}^t$ and $\left|v_b(t)/-\omega^2 W_0 e^{j\omega t}\right|^2/{R_l}^b$. The results are shown in Fig. 20 for a resistive load of 100 kΩ for the four cases of varying widths. The power output with the axial flexoelectric term included is nearly identical to the power output when it is not included, for all varying width cases for both the top and bottom layers (plots appear identical in Figs. 20a and 20b). To view the slight difference the power output when the axial strain gradient term is included and when it is neglected, the plots must be zoomed in. Figure 21

shows a zoomed in version of the power output FRF plot for both top and bottom layers for a single case of varying cross-sectional width. The small effect of the axial strain gradient term can be seen for both the top and bottom layers. A 0.03% power output difference results when including the axial strain gradient term, proving it is negligible at the aspect ratio used. Therefore, it can be neglected in the derivation of long, thin cantilever beams even with varying cross-section.

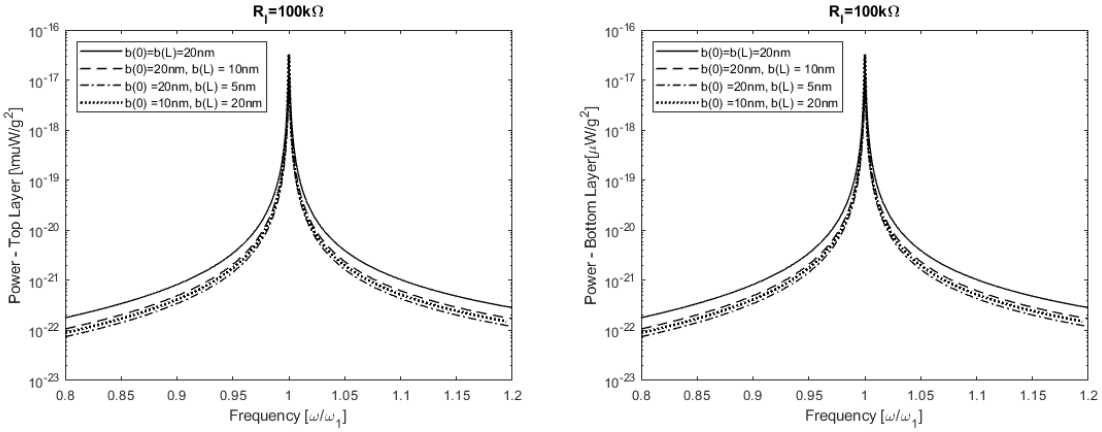

Figure 20: Power output frequency response for STO cantilevered flexoelectric bimorph with varying cross-sectional width undergoing bending vibrations for **(a)** top layer and **(b)** bottom layer each connected to 100 kΩ resistive load.

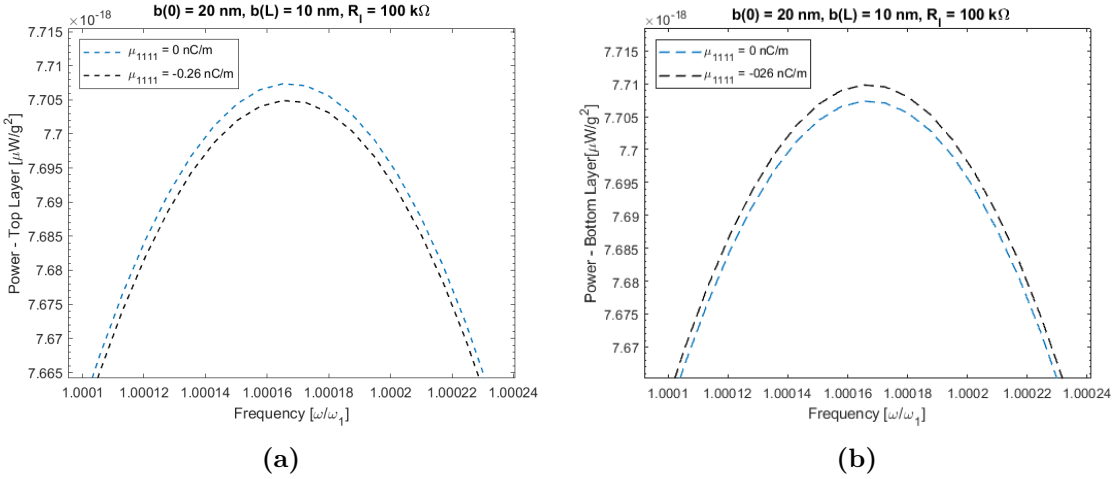

Figure 21: Zoomed in view of power output frequency response for STO cantilevered flexoelectric bimorph with varying cross-sectional width $b(x_1) = -\frac{\tilde{b}}{2L}x_1 + \tilde{b}$ undergoing bending vibrations: **(a)** top layer, **(b)** bottom layer each connected to 100 kΩ resistive load.

4.4.2 Electromechanical frequency response in energy harvesting for varying cross-section flexoelectric-piezoelectric bimorph beams

Next, simulations are performed to show the frequency response behavior for resonant energy harvesting and actuation of bimorph cantilevered beams with varying cross sectional widths (neglecting the axial strain gradient). The simulations in this section are for Barium Titanate (BTO) using the atomistic value presented by Maranganti and Sharma [60] of $\mu_{1133} = -5.463 \times 10^{-9}$ C/m along with the necessary material properties [8]: $e_{311} = -4.4$ C/m^2, $c^E_{1111} = 166$ GPa, $\varepsilon^s_{33} = 12.56$ nF/m, and $\rho = 5720$ kg/m^3. For each case, the $L/\tilde{b}/h$ aspect ratio was fixed at 100/5/1 and the total thickness is $h = 8$ nm. Four bimorphs are simulated with width profiles shown in Fig. 19.

To observe the effect of varying cross-sectional width on the flexoelectric-piezoelectric energy harvester, the electrical power FRF is calculated using $\left|v(t)/-\omega^2 W_0 e^{j\omega t}\right|^2/R_l$ for each of the widths. The results are shown in Fig. 19 for a range of resistive loads. The optimal load for peak power output can be determined for each case from the power output frequency response maps. Each case exhibits two peak values for two distinct optimal electrical loads, 100 kΩ and 100 MΩ, respectively, at the short-circuit and open-circuit frequencies, yielding the same power output. This is an indication of a relatively strongly coupled harvester configuration. The dynamic definition of the modal electromechanical coupling coefficient can be obtained based on the difference between the open-circuit and short-circuit natural frequencies as defined by Eq. 43 in Chapter 2. The uniform cantilever (Fig. 22a) has a coupling coefficient of $k = 0.105$ which is in good agreement with the analytical results from section 3.5.1 (see Fig. 13). The coupling increases with decreased tip width as shown in Fig. 22. The power output FRFs shown in Figs. 22b and 22c for narrower tip beams (Figs. 19b and 19c, respectively) exhibit a flexoelectric-piezoelectric coupling of $k = 0.114$ and $k = 0.119$, respectively. The larger tip width showed a decreased the coupling coefficient, $k = 0.094$ (Fig. 22d) but increased power output due to the larger tip acting like a tip mass (yielding an increased forcing under base excitation).

As in the previous chapter, it is of interest to understand structural response with varying cross-section of the BTO bimorph while generating electricity from strain (piezoelectric

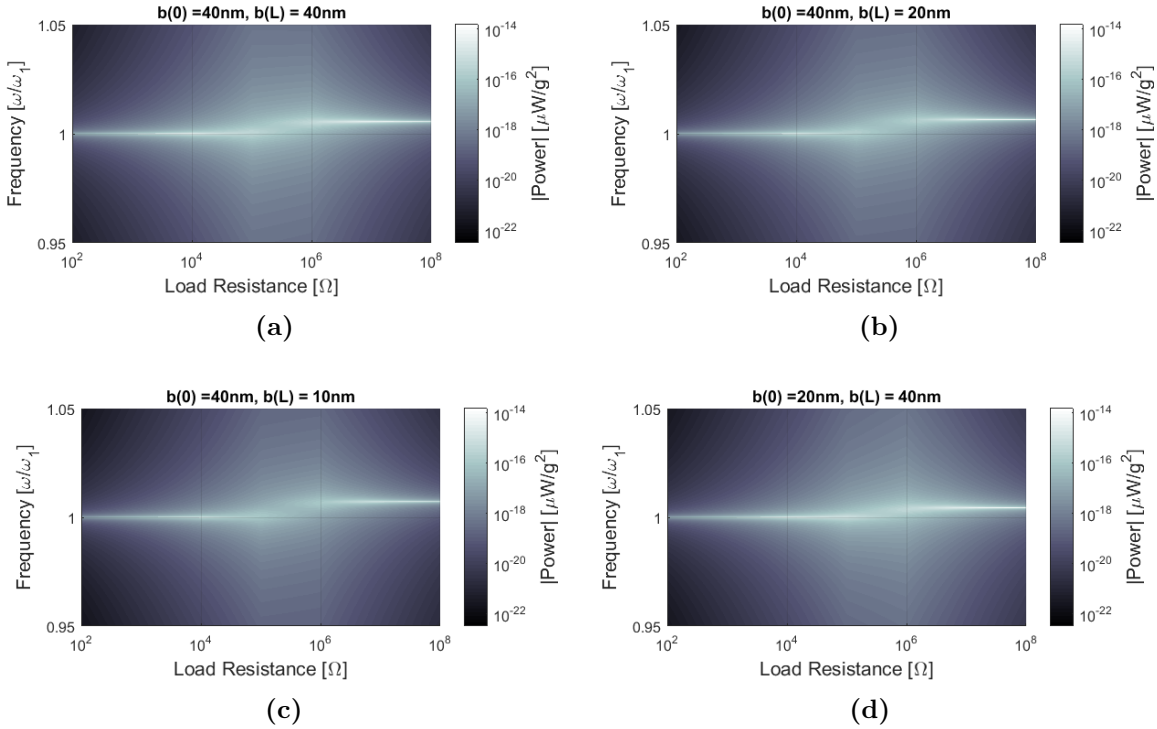

Figure 22: Power output frequency response vs. load resistance maps (in magnitude form and per base acceleration squared) for bimorph cantilevered BTO harvesters with a varying cross sectional widths: **(a)** $b(x_1) = \tilde{b}$, **(b)** $b(x_1) = -\frac{\tilde{b}}{2L}x_1 + \tilde{b}$, **(c)** $b(x_1) = -\frac{3\tilde{b}}{4L}x_1 + \tilde{b}$, **(d)** $b(x_1) = \frac{\tilde{b}}{2L}x_1 + \frac{\tilde{b}}{2}$

effect) and strain gradient (flexoelectric effect) fluctuations in response to mechanical base excitation. The motion of the cantilever is evaluated at the tip ($x_1 = L$) using Eq. 98. Figure 23 shows the tip displacement maps for all four width cases of the bimorph using the same load resistances and normalized excitation frequency range. The electromechanical coupling is relatively strong, as seen from previous electrical power output graphs (Fig. 22), and therefore, mechanical to electrical energy conversion is rather significant. Consequently, the structural response of the bimorph is sensitive to changing the electrical resistive load, as seen in Fig. 23, near the resonant frequency.

4.4.3 Electromechanical frequency response in actuation for varying cross-section flexoelectric-piezoelectric bimorph beams

The approximate analytical modeling framework is used to simulate the electromechanical response of the bimorphs with varying cross-sectional widths in the case of electrical excitation for the same set of system parameters. The tip displacement frequency response is

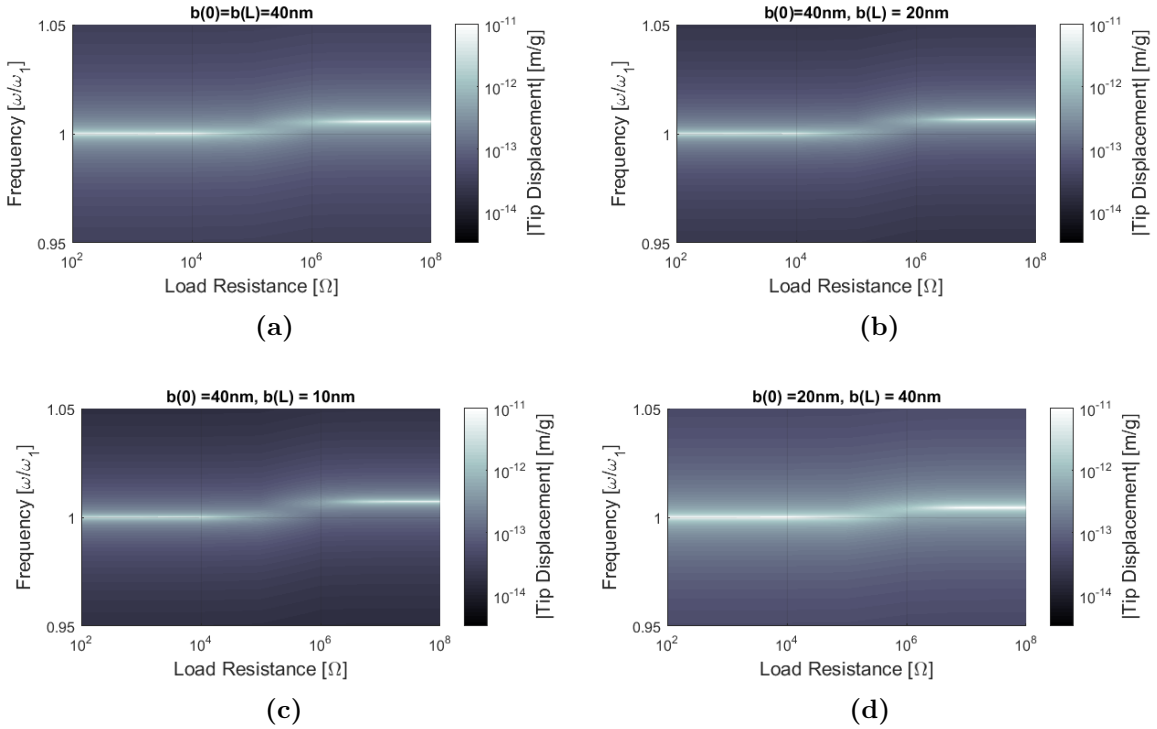

Figure 23: Tip displacement output frequency response vs. load resistance maps (in magnitude form and per base acceleration) for bimorph cantilevered BTO harvesters with a varying cross sectional widths: **(a)** $b(x_1) = \tilde{b}$, **(b)** $b(x_1) = -\frac{\tilde{b}}{2L}x_1 + \tilde{b}$, **(c)** $b(x_1) = -\frac{3\tilde{b}}{4L}x_1 + \tilde{b}$, **(d)** $b(x_1) = \frac{\tilde{b}}{2L}x_1 + \frac{\tilde{b}}{2}$

determined from Eq. 100 and the admittance frequency response from Eq. 101. The tip displacement and admittance frequency responses are shown in Figs. 24a and 24b, respectively. In the admittance plots, the percentage difference between the resonance and antiresonance frequencies is a measure of electromechanical coupling, and it increases significantly for the decreased tip width as indicated by the arrow in the inset of Fig. 24b.

Varying the cross-section results in a change in strain gradient distribution and can be used to increases the electromechanical coupling as shown in the previous power output, tip displacement, and admittance plots (Figs. 22, 23, and 24b). As shown by Eqs. 1 and 12, the *strain gradient*, $\partial S_{11}/\partial x_3$, in this model is nothing but the negative *curvature* of the beam. With decreased tip width the normalized curvature or strain distribution improves resulting in increased flexoelectric coupling. The normalized curvature for the varying cross-sectional widths is shown in Fig. 25b for the approximate analytical model (lines) and finite element analysis results (markers). The normalized curvature shows an increase with decreased tip

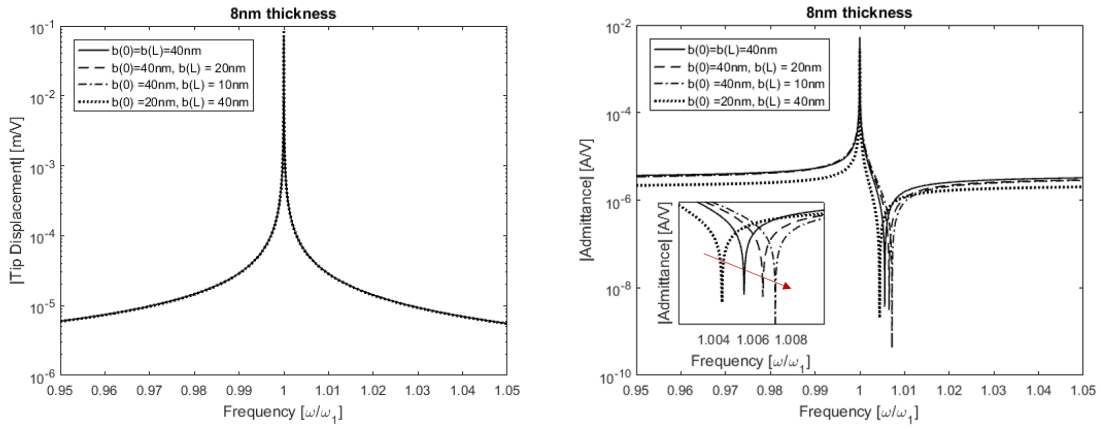

(a) **(b)**

Figure 24: **(a)** Tip displacement and **(b)** admittance frequency response functions (in magnitude form) for actuation of cantilevered BTO with varying cross sectional width.

width which explains the enhancement in the electromechanical coupling (Figs. 22, 23, and 24b).

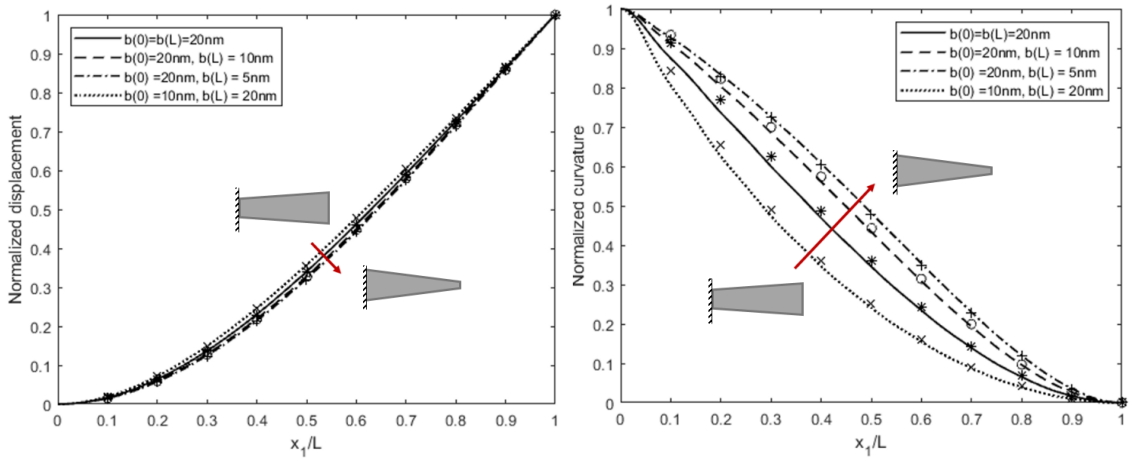

(a) **(b)**

Figure 25: Normalized **(a)** displacement and **(b)** curvature distributions of a thin cantilever with varying cross-sectional width for the fundamental bending vibration mode ($r = 1$) with arrow indicating decreased tip width and markers showing finite element analysis results from COMSOL.

4.5 Conclusions

An approximate analytical modeling framework for flexoelectric and piezoelectric effects and its modal analysis are presented for varying cross-section thin beams under bending

vibrations. For arbitrary cross-sections, the exact solution is beyond reach, and therefore an energy formulation is used. This model is based on the Euler-Bernoulli beam theory for the extended Hamilton's principle formulation and and properly accounts for thermodynamically consistent, symmetric, direct and converse coupling terms that include the combined flexoelectric and piezoelectric transverse coupling terms, revealing symmetric coupling. The same modeling framework was used to understand the electromechanical response of the bimorphs with varying cross-sectional widths in the case of electrical excitation. The effect of the axial strain gradient was shown to be negligible for long, thin beams. Varying cross-section profile (with a reduced tip width) in nanocantilevers yields increased electromechanical coupling. An increase of 14% in the coupling was seen when the uniform cross-section beam ($k \approx 0.105$) was decreased to a beam with tip width 1/4 the base width ($k \approx 0.119$). Larger tip width showed a decrease in coupling ($k \approx 0.094$) but an increase in power output do to the larger tip acting like a tip mass (yielding increased forcing magnitude under base excitation). In addition to varying cross-section, the effect of axial strain gradient was also studied. The axial strain gradient was found to be negligible of long, thin cantilever beams even with varying cross-section.

CHAPTER V

GEOMETRICALLY NONLINEAR FLEXOELECTRIC AND FLEXOELECTRIC-PIEZOELECTRIC CANTILEVER FOR ENERGY HARVESTING

5.1 Introduction

In this chapter we establish and analyze a geometrically nonlinear framework by accounting for the flexoelectric effect in monolayer dielectric cantilevers as well as bimorph piezoelectric cantilevers. Linear constitutive equations are used with the nonlinearity coming from the moderately large deformation of the cantilever with inextensibility condition. The focus is placed on the development of governing electroelastodynamic flexoelectric equations for the problem of resonant energy harvesting. The governing electroelastic equations are derived and then solved using the method of harmonic balance. Case studies are reported for the energy harvesting performance and size effects for a strontium titanate monolayer (non-piezoelectric) cantilever and a barium titanate bimorph cantilever under bending vibrations using atomistic flexoelectric constants from existing literature. The electromechanical frequency response functions for resonant power density and transmissibility are explored to capture size dependence.

5.2 Electroelastodynamic flexoelectric and flexoelectric-piezoelectric equations

We consider the problem of a centrosymmetric thin monolayer cantilever (Fig. 26) and a piezoelectric bimorph cantilever (not shown) under mechanical base excitation for transverse (bending) vibrations. Linear electroelastic material behavior and geometrically large oscillations are considered in this continuum framework.

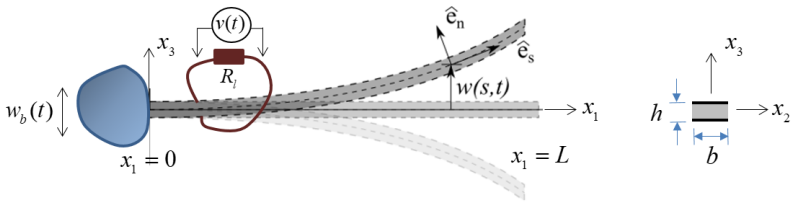

Figure 26: Base-excited centrosymmetric dielectric cantilever with surface electrodes (that are perpendicular to the thickness direction) connected to a resistive electrical load for energy harvesting, and a cross-sectional view for large deformations

5.2.1 Flexoelectric monolayer under base excitation

For a flexoelectric monolayer in bending the electric enthalpy density, H_f, is given by

$$H_f = \frac{1}{2}c_{1111}{S_{11}}^2 + \frac{1}{2}f_{1133}\frac{\partial P_3}{\partial x_3}S_{11} - \frac{1}{2}\mu_{1133}\frac{\partial S_{11}}{\partial x_3}E_3 - \frac{1}{2}\varepsilon_{33}{E_3}^2 \tag{102}$$

The bending strain for an Euler Bernoulli beam is given by $S_{11} = -x_3\theta_{,s}$, where θ is the angular displacement, x_3 is the distance from the neutral axis, and the subscript s denotes a spatial derivative with respect to the arc length s. The electric field across the electrodes is given by $E_3 = \frac{-v}{h} = \frac{\dot{\lambda}}{h}$, where v is the voltage across the electrodes and $\dot{\lambda}$ is the time derivative of the flux linkage [78]. Therefore, the strain energy $\left(U = \int_V H_f dV\right)$ for the flexoelectric beam is given by

$$U = \int_0^L \left[\int_0^b \int_0^h \left(\frac{1}{2}c_{1111}{x_3}^2{\theta_{,s}}^2 - \frac{1}{2}f_{1133}\frac{\partial P_3}{\partial x_3}x_3\theta_{,s} - \frac{1}{2}\mu_{1133}\theta_{,s}\frac{\dot{\lambda}}{h} - \frac{1}{2}\frac{\varepsilon_{33}}{h^2}\dot{\lambda}^2\right)dx_3dx_2\right]dx_1 \tag{103}$$

Evaluating the width and thickness integrals, the strain energy of the flexoelectric beam is

$$U = \int_0^L \left(\frac{1}{2}c_{1111}I\theta_{,s} - \vartheta\dot{\lambda}\left[H(s) - H(s-L)\right]\theta_{,s} - \frac{1}{2}\frac{C}{L}\dot{\lambda}^2\right)ds \tag{104}$$

where $H(s)$ is the Heaviside step function and $\vartheta = b\mu_{1133}$, $C = bL\varepsilon_{33}/h$, and $I = bh^3/12$.

The kinetic energy can be written as

$$T = \frac{1}{2}m\int_0^L \left[{u_{x_1,t}}^2 + \left(u_{x_3,t} + u_{b,t}\right)^2\right]ds \tag{105}$$

where m is the mass per unit length of the beam ($m = \rho bh$), u_{x_1} is the axial displacement, u_{x_3} is the transverse displacement, u_b is the base displacement and the subscript t indicates a derivative with respect to time.

For an inextensible cantilever, the Lagrangian, $\mathcal{L} = T - U$, needs to include a Lagrange multiplier, Λ, to account for the inextensibility condition of the cantilever. The Lagrangian is given by

$$\begin{aligned}\mathcal{L} = \frac{1}{2}m\int_0^L \left[{u_{x_1,t}}^2 + \left(u_{x_3,t} + u_{b,t}\right)^2\right] ds - \frac{1}{2}\Lambda\int_0^L \left[\left(1+u_{x_1,s}\right)^2 + {u_{x_3,s}}^2 - 1\right] ds + \\ - \int_0^L \left(\frac{1}{2}c^E_{1111} I\theta_{,s} - \vartheta\dot{\lambda}\left[H(x_1) - H(x_1 - L)\right]\theta_{,s} - \frac{1}{2}\frac{C}{L}\dot{\lambda}^2\right) ds\end{aligned} \tag{106}$$

The virtual work on the structure includes linear structural damping and electrical dissipation over a resistive load given as

$$\delta W_{NC} = \int_0^L \left(-c_z u_{x_3,t}\delta u_{x_3} - \frac{\dot{\lambda}}{R}\delta\lambda\right) ds \tag{107}$$

Using Eqs. 106 and 107, Hamilton's principle, $\int_{t_1}^{t_2}(\delta\mathcal{L} + \delta W_{NC})dt = 0$, is applied as described by Tan et al. [78]. This yields two equations of motion given as

$$\begin{aligned}m u_{x_3,tt} + c_z u_{x_3,t} + \frac{1}{2}m\left[u_{x_3,s}\int_L^s\left(\int_0^\delta u_{x_3,\xi}d\xi\right)_{,tt} d\delta\right]_{,s} + \\ + EI\left[u_{x_3,sss} + u_{x_3,s}\left(u_{x_3,s}u_{x_3,ss}\right)_{,s}\right]_{,s} - \vartheta v\left[\frac{\partial\delta(x_1)}{\partial s} - \frac{\partial\delta(x_1-L)}{\partial s}\right] + \\ - \vartheta v\left[\delta(x_1) - \delta(x_1 - L)\right]\left(u_{x_3,s}u_{x_3,ss}\right) = -m u_{b,tt}\end{aligned} \tag{108}$$

$$C\dot{v} + \frac{v}{R} + \int_0^L \vartheta\left(u_{x_3,ss} + \frac{1}{2}{u_{x_3,s}}^2 u_{x_3,ss}\right)_{,t} ds = 0 \tag{109}$$

For harmonic base excitation about the first natural frequency of the structure, a single mode assumption can be made for primary resonance behavior, $u_{x_3}(s,t) = \phi(s)\eta(t)$, where $\phi(s)$ is the mass normalized first mode shape of a cantilever given by

$$\phi(s) = \frac{1}{\sqrt{mL}}\left(\cos\frac{\lambda_1 s}{L} - \cosh\frac{\lambda_1 s}{L} + \frac{\sin\lambda_1 - \sinh\lambda_1}{\cos\lambda_1 - \cosh\lambda_1}\left(\sin\frac{\lambda_1 s}{L} - \sinh\frac{\lambda_1 s}{L}\right)\right) \tag{110}$$

where $\lambda_1 = 1.8751$ and the mass normalization condition is $\int_0^L m\phi_i(s)\phi_j(s)ds = \delta_{ij}$.

Applying 110 to Eqs. 108 and 109 yields the equations of motion in modal coordinates,

$$m^*\ddot{\eta} + c^*\dot{\eta} + k^*\eta + \frac{\alpha^*}{L^2}\eta^3 + \frac{\beta^*}{L^2}\left(\eta\dot{\eta}^2 + \eta^2\ddot{\eta}\right) - \theta v - \theta_{NL} v\eta^2 = G^*\cos\Omega t \tag{111}$$

$$C\dot{v} + \frac{v}{R} + \theta\dot{\eta} + \theta_{NL}\eta^2\dot{\eta} = 0 \tag{112}$$

where m^*, c^*, and k^* are the equivalent linear mass, damping and stiffness terms, α^* is the geometric hardening coefficient, β^* is the inertial softening coefficient, θ is the linear coupling coefficient, θ_{NL} is the nonlinear electromechanical coupling coefficient and G^* is the forcing term given as

$$\begin{gathered} m^* = m\int_0^L \phi^2(s)ds,\ c^* = c_z\int_0^L \phi^2(s)ds,\ k^* = EI\int_0^L \phi(s)\phi''''(s)ds \\ \alpha^* = EIL^2\int_0^L \phi(s)\Big\{\phi'(s)\big[\phi'(s)\phi''(s)\big]'\Big\}'ds \\ \beta^* = mL^2\int_0^L \phi(s)\left[\phi'(s)\int_L^s\int_0^\delta \phi'(s)^2 d\xi d\delta\right]'ds \\ \theta = \vartheta\phi'(L),\ \theta_{NL} = \frac{1}{2}\vartheta\big(\phi'(L)\big)^3,\ G^* = ma_b\int_0^L \phi(s)ds \end{gathered} \tag{113}$$

The modal equations given by Eqs. 111 and 112 can be non-dimensionalized using the following non-dimensional terms

$$\bar{\eta} = \frac{\phi(L)}{L}\eta,\ \bar{v} = \frac{C\phi(L)}{h\theta}v,\ \tau = \omega_n t,\ \bar{G} = \frac{L{\omega_n}^2}{\phi(L)}G^* \tag{114}$$

Substituting Eq.114 into Eqs. 111 and 112 yields the non-dimensional modal equations of motion

$$\ddot{\bar{\eta}} + \mathrm{Z}\dot{\bar{\eta}} + \bar{\eta} + \mathrm{A}\bar{\eta}^3 + \mathrm{B}\left(\bar{\eta}\dot{\bar{\eta}}^2 + \bar{\eta}^2\ddot{\bar{\eta}}\right) - \Pi\bar{v} - \Pi_{NL}\bar{v}\bar{\eta}^2 = \Gamma\cos\Omega\frac{\tau}{\omega_n} \tag{115}$$

$$\dot{\bar{v}} + \kappa\bar{v} + \chi\dot{\bar{\eta}} + \chi_{NL}\bar{\eta}^2\dot{\bar{\eta}} = 0 \tag{116}$$

where the non-dimensional parameters are

$$\begin{gathered} \mathrm{Z} = 2\zeta,\ \mathrm{A} = \frac{\alpha^*}{m^*{\omega_n}^2\phi(L)^2},\ \mathrm{B} = \frac{\beta^*}{m^*\phi^2(L)} \\ \Pi = \frac{\theta^2 h}{m^*C{\omega_n}^2L},\ \Pi_{NL} = \frac{\theta_{NL}\theta hL}{m^*C{\omega_n}^2\phi^2(L)},\ \Gamma = \frac{G^*\phi(L)}{m^*{\omega_n}^2L} \\ \kappa = \frac{1}{RC\omega_n},\ \chi = \frac{L}{h},\ \chi_{NL} = \frac{\theta_{NL}L^3}{h\phi^2(L)\theta} \end{gathered} \tag{117}$$

5.2.2 Flexoelectric-piezoelectric bimorph under base excitation

For a piezoelectric bimorph in bending the electric enthalpy density given by Eq. 102 can be modified to include the piezoelectric terms yielding

$$H_p = \frac{1}{2}c^E_{1111}{S_{11}}^2 - e_{311}E_3S_{11} + \frac{1}{2}f_{1133}\frac{\partial P_3}{\partial x_3}S_{11} - \frac{1}{2}\mu_{1133}\frac{\partial S_{11}}{\partial x_3}E_3 - \frac{1}{2}\varepsilon^s_{33}{E_3}^2 \tag{118}$$

Following the same procedure as the previous section, the strain energy for the bimorph beam is

$$U = \int_0^L \left(\frac{1}{2} c_{1111}^E I_p \theta_{,s} - \vartheta_p \dot{\lambda} \left[H(s) - H(s-L) \right] \theta_{,s} - \frac{1}{2} \frac{C_p}{L} \dot{\lambda}^2 \right) ds \tag{119}$$

where $\vartheta_p = \frac{bh_p}{2} e_{311} + b\mu_{1133}$, $C_p = \frac{1}{2} bL\varepsilon_{33}/h_p$, and $I_p = \frac{2}{3} bh_p^3$.

The kinetic energy is given by Eq. 105 where the mass per unit length of the bimorph beam is $m = 2\rho b h_p$.

As with an inextensible monolayer cantilever, the Lagrangian for the inextensible bimorph, $\mathcal{L} = T - U$, needs to include a Lagrange multiplier, Λ, to account for the inextensibility condition of the cantilever. The Lagrangian is given by

$$\begin{aligned} \mathcal{L} = \frac{1}{2} m \int_0^L \left[{u_{x_1,t}}^2 + \left(u_{x_3,t} + u_{b,t} \right)^2 \right] ds - \frac{1}{2} \Lambda \int_0^L \left[\left(1 + u_{x_1,s} \right)^2 + {u_{x_3,s}}^2 - 1 \right] ds + \\ - \int_0^L \left(\frac{1}{2} c_{1111}^E I_p \theta_{,s} - \vartheta_p \dot{\lambda} \left[H(x_1) - H(x_1 - L) \right] \theta_{,s} - \frac{1}{2} \frac{C_p}{L} \dot{\lambda}^2 \right) ds \end{aligned} \tag{120}$$

The virtual work of the bimorph beam is given by Eq. 107. Using Eqs. 107 and 120, Hamilton's principle, $\int_{t_1}^{t_2} (\delta \mathcal{L} + \delta W_{NC}) dt = 0$, is applied as done in the previous section and described by Tan et al. [78]. The resulting equations of motion are given as

$$\begin{aligned} m u_{x_3,tt} + c_z u_{x_3,t} + \frac{1}{2} m \left[u_{x_3,s} \int_L^s \left(\int_0^\delta u_{x_3,\xi} d\xi \right)_{,tt} d\delta \right]_{,s} + \\ + EI_p \left[u_{x_3,sss} + u_{x_3,s} \left(u_{x_3,s} u_{x_3,ss} \right)_{,s} \right]_{,s} - \vartheta_p v \left[\frac{\partial \delta(x_1)}{\partial s} - \frac{\partial \delta(x_1 - L)}{\partial s} \right] + \\ - \vartheta_p v \left[\delta(x_1) - \delta(x_1 - L) \right] \left(u_{x_3,s} u_{x_3,ss} \right) = -m u_{b,tt} \end{aligned} \tag{121}$$

$$C_p \dot{v} + \frac{v}{R} + \int_0^L \vartheta_p \left(u_{x_3,ss} + \frac{1}{2} {u_{x_3,s}}^2 u_{x_3,ss} \right)_{,t} ds = 0 \tag{122}$$

For harmonic base excitation about the first natural frequency of the structure, a single mode assumption can be made for primary resonance behavior, $u_{x_3}(s,t) = \phi(s)\eta(t)$, where $\phi(s)$ is the mass normalized first mode shape of a cantilever given by Eq. 110 with the respective mass and length parameters for the bimorph beam. The modal equations of motion are obtained by applying Eq. 110 to Eqs. 121 and 122 yielding

$$m^* \ddot{\eta} + c^* \dot{\eta} + k_p^* \eta + \frac{\alpha_p^*}{L^2} \eta^3 + \frac{\beta^*}{L^2} \left(\eta \dot{\eta}^2 + \eta^2 \ddot{\eta} \right) - \theta^p v - \theta_{NL}^p v \eta^2 = G^* \cos \Omega t \tag{123}$$

$$C_p\dot{v} + \frac{v}{R} + \theta^p\dot{\eta} + \theta^p_{NL}\eta^2\dot{\eta} = 0 \tag{124}$$

where m^*, c^*, and k^*_p are the equivalent linear mass, damping and stiffness terms, α^*_p is the geometric hardening coefficient, β^* is the inertial softening coefficient, θ^p is the linear coupling coefficient, θ^p_{NL} is the nonlinear electromechanical coupling coefficient and G^* is the forcing term of the bimorph given as

$$\begin{gathered}
m^* = m\int_0^L \phi^2(s)ds,\ c^* = c_z\int_0^L \phi^2(s)ds,\ k^*_p = EI_p\int_0^L \phi(s)\phi''''(s)ds \\
\alpha^*_p = EI_pL^2\int_0^L \phi(s)\Big\{\phi'(s)\big[\phi'(s)\phi''(s)\big]'\Big\}'ds \\
\beta^* = mL^2\int_0^L \phi(s)\left[\phi'(s)\int_L^s\int_0^\delta \phi'(s)^2 d\xi d\delta\right]'ds \\
\theta^p = \vartheta_p\phi'(L),\ \theta^p_{NL} = \frac{1}{2}\vartheta_p\big(\phi'(L)\big)^3,\ G^* = ma_b\int_0^L \phi(s)ds
\end{gathered} \tag{125}$$

The modal equations given by Eqs. 123 and 124 can be non-dimensionalized using the following non-dimensional terms

$$\bar{\eta} = \frac{\phi(L)}{L}\eta,\ \bar{v} = \frac{C_p\phi(L)}{h\theta^p}v,\ \tau = \omega_n t,\ \bar{G} = \frac{L{\omega_n}^2}{\phi(L)}G^* \tag{126}$$

Substituting Eq.126 into Eqs. 123 and 124 yields the non-dimensional modal equations of motion for the flexoelectric-piezoelectric bimorph

$$\ddot{\bar{\eta}} + \mathrm{Z}\dot{\bar{\eta}} + \bar{\eta} + \mathrm{A}_p\bar{\eta}^3 + \mathrm{B}\left(\bar{\eta}\dot{\bar{\eta}}^2 + \bar{\eta}^2\ddot{\bar{\eta}}\right) - \Pi^p\bar{v} - \Pi^p_{NL}\bar{v}\bar{\eta}^2 = \Gamma\cos\Omega\frac{\tau}{\omega_n} \tag{127}$$

$$\dot{\bar{v}} + \kappa_p\bar{v} + \chi^p\dot{\bar{\eta}} + \chi^p_{NL}\bar{\eta}^2\dot{\bar{\eta}} = 0 \tag{128}$$

where the non-dimensional parameters for the bimorph beam are

$$\begin{gathered}
\mathrm{Z} = 2\zeta,\ \mathrm{A}_p = \frac{\alpha^*_p}{m^*{\omega_n}^2\phi(L)^2},\ \mathrm{B} = \frac{\beta^*}{m^*\phi^2(L)} \\
\Pi^p = \frac{(\theta^p)^2h}{m^*C{\omega_n}^2L},\ \Pi^p_{NL} = \frac{\theta^p_N L\theta^p hL}{m^*C_p{\omega_n}^2\phi^2(L)},\ \Gamma = \frac{G^*\phi(L)}{m^*{\omega_n}^2L} \\
\kappa_p = \frac{1}{RC\omega_n},\ \chi^p = \frac{L}{h},\ \chi^p_{NL} = \frac{\theta^p_{NL}L^3}{h\phi^2(L)\theta^p}
\end{gathered} \tag{129}$$

5.2.3 Method of harmonic balance to solve equations

The coupled ODEs given by Eqs. 115 and 116 for the monolayer and Eqs. 127 and 128 for the bimorph are solved using the method of harmonic balance [64] for a range of resistive

loads and acceleration levels. For harmonic base excitation with a driving frequency of Ω, the mechanical response and the voltage output are expected to be periodic at the same frequency and can be approximated by the truncated Fourier series expansions

$$\begin{aligned} w_Q &= \sum_{q=1}^{Q} \left[a_q \cos\left(q\Omega\frac{\tau}{\omega_n}\right) + b_q \sin\left(q\Omega\frac{\tau}{\omega_n}\right)\right] \\ v_Q &= \sum_{q=1}^{Q} \left[c_q \cos\left(q\Omega\frac{\tau}{\omega_n}\right) + d_q \sin\left(q\Omega\frac{\tau}{\omega_n}\right)\right] \end{aligned} \tag{130}$$

where Q is the number of harmonic considered and due to the symmetry of the structure, the typical constants a_0 and b_0 of the Fourier series are zero. Substituting the approximate solutions (Eq.130) into Eqs. 115 and 116 yields the residual functions

$$\begin{aligned} R_1 &= \ddot{w}_Q + \mathrm{Z}\dot{w}_Q + w_Q + \mathrm{A}{w_Q}^3 + \mathrm{B}\left(w_Q\dot{w}_Q^2 + {w_Q}^2\ddot{w}_Q\right) - \Pi v_Q - \Pi_{NL} v_Q {w_Q}^2 - \Gamma\cos\Omega\frac{\tau}{\omega_n} \\ R_2 &= \dot{v}_Q + \kappa v_Q + \chi\dot{w}_Q + \chi_{NL}{w_Q}^2\dot{w}_Q \end{aligned} \tag{131}$$

The equations for the flexoelectric-piezoelectric bimorph yield similar residual functions with the respective non-dimensional parameters.

Using the Galerkin method of weighted residuals, a system of $4Q$ algebraic equations for the Fourier coefficients a_q, b_q, c_q, d_q can be generated from

$$\begin{aligned} &\int_0^{2\pi/Q} R_1 \cos\left(q\Omega\frac{\tau}{\omega_n}\right) dt = 0, \quad \int_0^{2\pi/Q} R_2 \cos\left(q\Omega\frac{\tau}{\omega_n}\right) dt = 0 \\ &\int_0^{2\pi/Q} R_1 \sin\left(q\Omega\frac{\tau}{\omega_n}\right) dt = 0, \quad \int_0^{2\pi/Q} R_2 \sin\left(q\Omega\frac{\tau}{\omega_n}\right) dt = 0, \ q = 1, ..., Q \end{aligned} \tag{132}$$

Here we choose to include $Q = 3$ harmonics resulting in 12 equations and 12 unknowns. These equations are solved using a multivariate Newton-Raphson method. The driving frequency Ω is linearly swept up and down around the first natural frequency.

5.3 Case studies and results

In this section, the electromechanical frequency response functions of cantilevered flexoelectric and flexoelectric-piezoelectric energy harvesters under base excitation are simulated with a focus on the first bending mode ($r = 1$) for a broad range of electrical

load resistance values and base excitation levels. For both beams, three different geometric scales are explored, spanning from mm-scale to nm-scale thickness. For each case the length/width/thickness aspect ($L/b/h$, $h = 2h_p$ for bimorph) ratio is fixed at 600/30/1. The cantilevers have perfectly conductive surface electrodes on the faces that are perpendicular to the direction of transverse base excitation (Fig. 26). A mechanical quality factor (Q) of 50 is assumed, yielding an approximate modal mechanical damping ratio of 1% of the critical damping (i.e. $\zeta_1 = 1/2Q = 0.01$ for the first bending mode). The mechanical excitation is harmonic base excitation. Therefore, the results are given in the form of power density (power/volume) and transmissibility (tip displacement/base displacement) frequency response functions (FRFs). A wide range of electrical load resistance values spanning from short- to open-circuit conditions (10 mΩ to 10 GΩ) are simulated for each case study to capture the optimal load in power generation and the respective trends with changing load.

5.3.1 Electromechanical frequency response for flexoelectric monolayer cantilever in energy harvesting

The monolayer harvester simulations are performed for Strontium Titanate (STO) using the elastic [9, 44] and dielectric [89, 3] properties of $c_{1111} = 318$ GPa, $\rho = 5116$ kg/m^3, and $\varepsilon_{33} = 2.66$ nF/m (for the room temperature relative permittivity [89, 88, 3], $\varepsilon_{33}/\varepsilon_0 = 300$), and using the atomistic flexoelectric coefficient value [60] of $\mu_{1133} = -3.75 \times 10^{-9}$ C/m.

The electrical power density exhibits interesting trends, such as the presence of the optimal electrical load resulting in the maximum power output at a given frequency. The power density is calculated using $\left(|v(t)|^2/R_l\right)/bhL$ for each of the three geometric scales. The resulting graphs are shown in Fig. 27a. The optimal peak power output can be determined for each case from the power density frequency response plots. For both the 1 mm and 1 μm thick harvesters, a single peak power density is seen around 1 MΩ (Figs. 27a.i and 27a.ii). As demonstrated in Chapter 2 for linear vibrations, this is an indication of weak electromechanical coupling at these thickness levels. The 1 nm case study exhibits two peak power density values for two distinct optimal electrical loads, 100 kΩ and 3 MΩ (Fig. 27a.iii). This is an indication of strong electromechanical coupling due as observed in the linear vibrations simulated in Chapter 2.

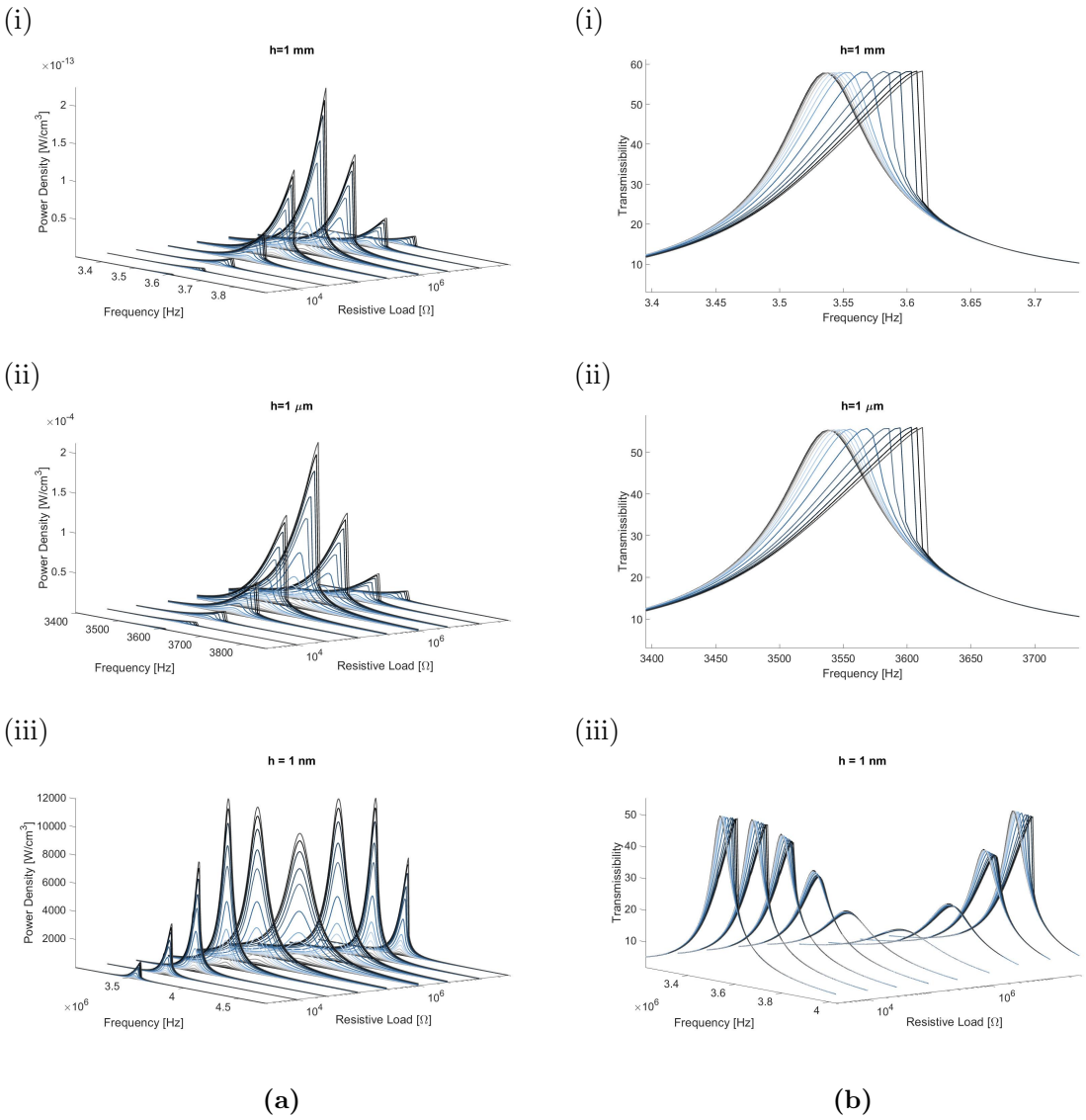

Figure 27: **(a)** Power density frequency response vs. load resistance and frequency (in magnitude form) and **(b)** transmissibility frequency response vs. load resistance and frequency (in magnitude form) for a range of acceleration levels for cantilevered STO harvesters with a fixed aspect ratio of 600/30/1 ($L/b/h$) for three different geometric scales with the following thickness (h) values: (i) 1 mm, (ii) 1 μm, and (iii) 1 nm.

The structural response of the STO cantilever while generating electricity from strain gradient fluctuations (flexoelectricity) in response to mechanical base excitation is also of interest for the large deformation. The transmissibility FRF is given by $|w(L,t)|/\left(A_0/\Omega^2\right)$ where A_0 is the base acceleration level in g ($1g = 9.81$ m/s^2). Figure 27b shows the transmissibility frequency response functions for the cantilevers of all three geometric scales using the same load resistance values. As a manifestation of weak electromechanical coupling, for

the cases of 1 mm and 1 μm thickness levels, the vibration response is insensitive to change in resistive load resulting in the plots as shown in Figs. 27b.i and 27b.ii. In the 1 nm thick case, the electromechanical coupling is large as shown by the vibration response being sensitive to change in resistive load (Fig. 27b.iii). For certain load resistance values, the vibration response and jump phenomenon is suppressed due to the large electromechanical coupling. Certain load resistance values result in significant shunt damping, analogous to piezoelectric shunt damping [37, 50], confirming thermodynamic consistency of the fully coupled electroelastodynamic model.

5.3.2 Electromechanical frequency response for flexoelectric-piezoelectric bimorph cantilever in energy harvesting

The bimorph flexoelectric-piezoelectric harvester simulations are performed for Barium Titanate (BTO) using the atomistic value presented by Maranganti and Sharma [60] of $\mu_{1133} = -5.463 \times 10^{-9}$ C/m along with the necessary material properties [8]: $e_{311} = -4.4$ C/m^2, $c^E_{1111} = 166$ GPa, $\varepsilon^s_{33} = 12.56$ nF/m, and $\rho = 5720$ kg/m^3.

The power density plots for the BTO harvester are shown in Fig. 28a. For all three geometric scales, the jump phenomenon is observed. The 1 mm beam and the 1 μm have a single peak power output around 300 kΩ (Figs. 28a.i and 28a.ii due to weak electromechanical coupling. For the 1 nm thick beam, two peak power outputs are seen at 30 kΩ and 3 MΩ (Fig. 28a.iii) due to strong electromechanical coupling due to flexoelectricity.

The transmissibility plots for the BTO harvester are shown in Fig. 28b. Due to the weak piezoelectric coupling in the 1 mm and 1 μm cases, the structural responses of the beams are slightly sensitive to the change in resistive load and the vibration response and jump phenomenon is slightly suppressed (Figs. 28b.i and 28b.ii). However, large vibration suppression is observed in the 1 nm case due to the large electromechanical coupling due to flexoelectricity (Fig. 28b.iii).

5.4 Conclusions

An electroelastodynamic framework is established and analyzed for a geometrically nonlinear flexoelectric cantilever, by accounting for the inextensibility condition, the presence of

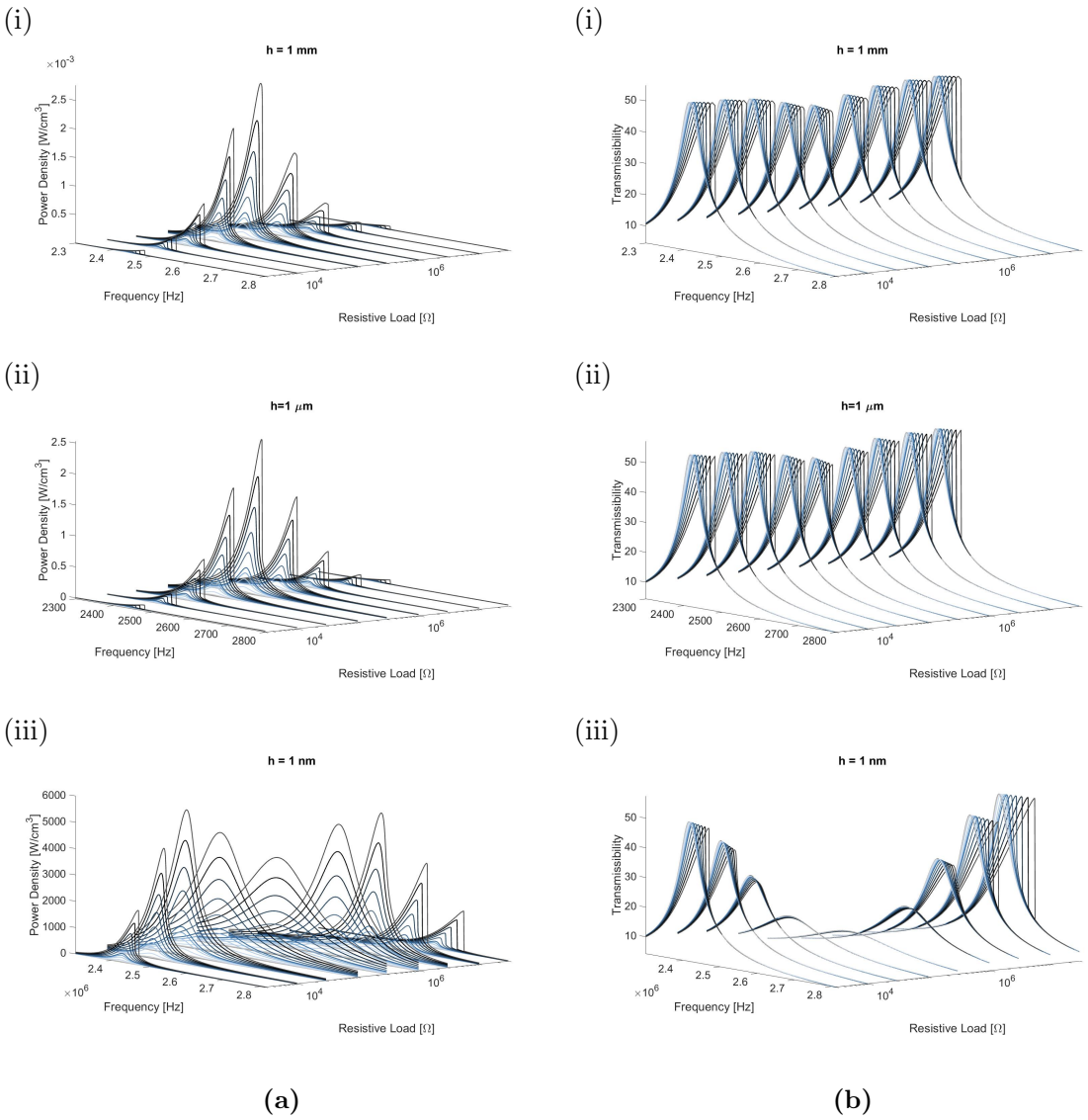

Figure 28: **(a)** Power density frequency response vs. load resistance and frequency (in magnitude form) and **(b)** transmissibility frequency response vs. load resistance and frequency (in magnitude form) for a range of acceleration levels for cantilevered BTO harvesters with a fixed aspect ratio of 600/30/1 ($L/b/h, h = 2h_p$) for three different geometric scales with the following thickness (h) values: (i) 1 mm, (ii) 1 μm, and (iii) 1 nm.

a finite electrical load across the electrodes, as well as, two-way electromechanical coupling. The model is then extended to include the combined flexoelectric-piezoelectric effects in a bimorph cantilever. The focus is placed on the development of governing electroelastodynamic flexoelectric equations for the problem of resonant energy harvesting. It is observed that a nonlinear electromechanical coupling results from the inextensibility condition even for linear constitutive equations for both the monolayer and bimorph configurations. The

governing electroelastic equations are derived and then solved using the method of harmonic balance. Simulations are performed for the energy harvesting performance and size effects for a Strontium Titanate monolayer (non-piezoelectric) cantilever and a Barium Titanate bimorph cantilever under bending vibrations using atomistic flexoelectric constants from existing literature. The electromechanical frequency response functions for resonant power density and transmissibility capture the size dependence, and the jump phenomenon is observed. It is observed that increased electromechanical coupling at nanoscale, due to flexoelectricity, results in significant vibration suppression for certain electrical load values. Enhanced bandwidth due to nonlinear frequency response can improve the harvested power over a broader range of frequencies as compared to linear resonance.

CHAPTER VI

FLEXOELECTRIC AND FLEXOELECTRIC-PIEZOELECTRIC PLATE MODELS FOR BENDING VIBRATIONS

6.1 Introduction

In this chapter we establish and explore a complete analytical framework for two-dimensional dielectric plate configurations by expanding the analysis performed in Chapters 2 and 3. Closed-form expressions are developed for the electromechanically coupled voltage across the electrical load and the shunted vibration response of flexoelectric monolayer and flexoelectric-piezoelectric bimorph plates. The modeling framework is then extended to the dynamic actuation (electrical excitation) problem for a fixed base. Simulation case studies are given for transverse vibrations of Strontium Titanate (non-piezoelectric) and Barium Titanate simply supported plates under mechanical base excitation for energy harvesting and electrical excitation (fixed base) for dynamic actuation. The frequency response functions are simulated at different geometric scales to explore the effects of thickness on the flexoelectric energy conversion and power generation in two-dimensional structures.

6.2 Kirchhoff plate model for flexoelectric and flexoelectric-piezoelectric energy harvesting

We consider the problem of a centrosymmetric thin rectangular plate and a piezoelectric thin rectangular bimorph plate for linear vibrations, i.e. linear electroelastic material behavior and geometrically small oscillations are assumed (Fig 29). The surface electrodes of each plate are shunted to a resistive load to quantify the electrical power output in the harvester model. The sample geometry justifies the thin plate assumption, such that the thickness (h) is much smaller than the lateral dimensions (a and b). The thin plate is considered a Kirchhoff plate so that the transverse shear stress components and the normal stress in the thickness direction are negligible.

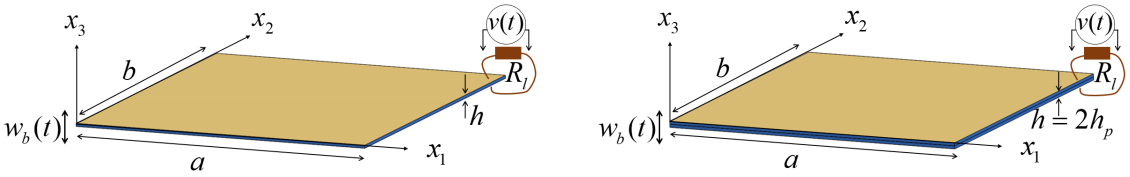

Figure 29: (a) Centrosymmetric dielectric monolayer plate and **(b)** piezoelectric bimorph plate with surface electrodes (that are perpendicular to the thickness direction) connected to a resistive electrical load for energy harvesting under mechanical base excitation

The displacement field for the Kirchhoff plate is

$$\begin{aligned} u &= -x_3 \frac{\partial w}{\partial x_1} \\ v &= -x_3 \frac{\partial w}{\partial x_2} \\ w &= w(x_1, x_2, t) \end{aligned} \tag{133}$$

where u and v are the axial displacements in the 1 and 2 directions, respectively, and $w(x_1, x_2, t)$ is the transverse displacement of the plate (neutral axis).

The partial differential equation governing the forced vibration of a uniform thin dielectric plate (monolayer or bimorph - Fig. 29) is

$$-\left(\frac{\partial^2 M_{11}}{\partial x_1^2} + 2\frac{\partial^2 M_{12}}{\partial x_1 \partial x_2} + \frac{\partial^2 M_{22}}{\partial x_2^2}\right) + c\frac{\partial w(x_1, x_2, t)}{\partial t} + m\frac{\partial^2 w(x_1, x_2, t)}{\partial t^2} = f(x_1, x_2, t) \tag{134}$$

where $f(x_1, x_2, t)$ is the forcing, $M_{11}(x_1, x_2, t)$ and $M_{22}(x_1, x_2, t)$ are the internal bending moments at positions x_1 and x_2 and time t, $M_{12}(x_1, x_2, t)$ is the internal twisting moment, c is the viscous air damping coefficient, m is the mass per unit area of the plate ($m = \rho h$ for a monolayer or $m = 2\rho h_p$ for a bimorph plate, where ρ is the mass density of the plate material). For base excitation, the forcing is $f(x_1, x_2, t) = f(t) = -m\frac{d^2 w_b(t)}{dt^2}$, where $w_b(t)$ is the base displacement.

The internal bending moments in Eq. 134 are given as

$$\begin{aligned} M_{11} &= \int_{-h/2}^{h/2} T_{11} x_3 dx_3 \\ M_{22} &= \int_{-h/2}^{h/2} T_{22} x_3 dx_3 \end{aligned} \tag{135}$$

and the internal twisting moment is

$$M_{12} = \int_{-h/2}^{h/2} T_{12} x_3 dx_3 \tag{136}$$

where T_{11} and T_{22} are the axial stresses in the 1 and 2 directions, respectively, T_{12} is the shear stress, c_{1111} , c_{1122}, and c_{1212} are elastic constants.

The strain in the Kirchhoff plate can be expressed as

$$\begin{aligned} S_{11} &= -x_3 \frac{\partial^2 w}{\partial {x_1}^2} \\ S_{22} &= -x_3 \frac{\partial^2 w}{\partial {x_2}^2} \\ S_{12} &= -2x_3 \frac{\partial^2 w}{\partial x_1 \partial x_2} \end{aligned} \tag{137}$$

where S_{11} and S_{22} are are the axial strains in the 1 and 2 directions, respectively and S_{12} is the shear strain.

6.2.1 Flexoelectric monolayer plate for energy harvesting

The polarization including the *direct* flexoelectric effect for the monolayer Kirchhoff plate can be written as

$$P_3 = \chi_{33} E_3 + \mu_{1133} \frac{\partial S_{11}}{\partial x_3} + \mu_{1133} \frac{\partial S_{22}}{\partial x_3} \tag{138}$$

The mechanical stress state accounting for the *converse* flexoelectric effect of the monolayer Kirchhoff plate can be expressed as

$$\begin{aligned} T_{11} &= c_{1111} S_{11} + c_{1122} S_{22} + f_{1133} \frac{\partial P_3}{\partial x_3} \\ T_{22} &= c_{1122} S_{11} + c_{1111} S_{22} + f_{1133} \frac{\partial P_3}{\partial x_3} \\ T_{12} &= c_{1212} S_{12} \end{aligned} \tag{139}$$

Substituting the stresses and strains given by Eqs. 137 and 139 into the internal bending and twisting moment expressions given by Eqs. 135 and 136 yields

$$M_{11} = \int_{-h/2}^{h/2} \left(-c_{1111} \frac{\partial^2 w}{\partial {x_1}^2} {x_3}^2 - c_{1122} \frac{\partial^2 w}{\partial {x_2}^2} {x_3}^2 + f_{1133} \frac{\partial P_3}{\partial x_3} x_3 \right) dx_3 \tag{140}$$

$$M_{22} = \int_{-h/2}^{h/2} \left(-c_{1122} \frac{\partial^2 w}{\partial {x_1}^2} {x_3}^2 - c_{1111} \frac{\partial^2 w}{\partial {x_2}^2} {x_3}^2 + f_{1133} \frac{\partial P_3}{\partial x_3} x_3 \right) dx_3 \tag{141}$$

$$M_{12} = \int_{-h/2}^{h/2} -2c_{1212}\frac{\partial^2 w}{\partial x_1 \partial x_2}{x_3}^2 dx_3 \tag{142}$$

For a finite sample (in which the polarization varies continuously from its bulk value to zero at the electrode [77]), the flexoelectric term can be evaluated using integration by parts to identify its role in the bending moment equations (as done in the Euler-Bernoulli beam case shown in Chapter 2). The electric field, E_3, can be given in terms of the voltage (v) across the electrodes and the electrode spacing as $E_3 = -v/h$ (where it is assumed that the electrode thickness is negligible). Evaluating the integrals in the internal moment equations yields

$$M_{11} = -D_f\left(\frac{\partial^2 w}{\partial {x_1}^2} + \frac{c_{1122}}{c_{1111}}\frac{\partial^2 w}{\partial {x_2}^2}\right) + \mu_{1133}v(t)\left[H(x_1) - H(x_1 - a)\right]\left[H(x_2) - H(x_2 - b)\right] \tag{143}$$

$$M_{22} = -D_f\left(\frac{c_{1122}}{c_{1111}}\frac{\partial^2 w}{\partial {x_1}^2} + \frac{\partial^2 w}{\partial {x_2}^2}\right) + \mu_{1133}v(t)\left[H(x_1) - H(x_1 - a)\right]\left[H(x_2) - H(x_2 - b)\right] \tag{144}$$

$$M_{12} = -D_f\frac{2c_{1212}}{c_{1111}}\frac{\partial^2 w}{\partial x_1 \partial x_2} \tag{145}$$

where $H(x_1)$ is the Heaviside function and the flexural rigidity of the flexoelectric plate is

$$D_f = c_{1111}\frac{h^3}{12} \tag{146}$$

The flexoelectrically coupled centrosymmetric Kirchhoff plate equation for transverse vibrations can then be obtained from Eq. 134 as

$$\begin{aligned} &D_f\left[\frac{\partial^4 w}{\partial x_1^4} + 2\left(\frac{c_{1122}}{c_{1111}} + \frac{2c_{1212}}{c_{1111}}\right)\frac{\partial^4 w}{\partial x_1^2 \partial x_2^2} + \frac{\partial^4 w}{\partial x_2^4}\right] + c\frac{\partial w}{\partial t} + m\frac{\partial^2 w}{\partial t^2} + \\ &-\mu_{1133}v(t)\left(\begin{array}{l}\left[\dfrac{d\delta(x_1)}{d(x_1)} - \dfrac{d\delta(x_1 - a)}{dx_1}\right]\left[H(x_2) - H(x_2 - b)\right] \\ +\left[H(x_1) - H(x_1 - a)\right]\left[\dfrac{d\delta(x_2)}{d(x_2)} - \dfrac{d\delta(x_2 - b)}{dx_2}\right]\end{array}\right) = f(x_1, x_2, t)\end{aligned} \tag{147}$$

where $\delta(x_1)$ is the Dirac delta function.

Assuming a transversely isotropic material where $c_{1212} = \frac{1}{2}(c_{1111} - c_{1122})$ and $\nu =$

c_{1122}/c_{1111}, Eq. 147 simplifies to become

$$D_f\left[\frac{\partial^4 w}{\partial x_1^4}+2\frac{\partial^4 w}{\partial x_1^2\partial x_2^2}+\frac{\partial^4 w}{\partial x_2^4}\right]+c\frac{\partial w}{\partial t}+m\frac{\partial^2 w}{\partial t^2}+$$
$$-\mu_{1133}v(t)\left(\begin{array}{l}\left[\frac{d\delta(x_1)}{d(x_1)}-\frac{d\delta(x_1-a)}{dx_1}\right][H(x_2)-H(x_2-b)]\\+[H(x_1)-H(x_1-a)]\left[\frac{d\delta(x_2)}{d(x_2)}-\frac{d\delta(x_2-b)}{dx_2}\right]\end{array}\right)=f(x_1,x_2,t) \tag{148}$$

The vibration response (transverse displacement of the neutral axis) can be represented as

$$w(x_1,x_2,t)=\sum_{m=1}^{\infty}\sum_{n=1}^{\infty}\phi_{mn}(x_1,x_2)\eta_{mn}(t) \tag{149}$$

Here, $\eta_{mn}(t)$ is the modal mechanical coordinate and $\phi_{mn}(x_1,x_2)$ is the mass-normalized eigenfunction (obtained from the short-circuit problem) for the mn-th vibration mode.

The mass-normalized eigenfunctions in Eq. 149 satisfy the following orthogonality conditions

$$\int_0^a\int_0^b \rho h\phi_{mn}(x_1,x_2)\phi_{rs}(x_1,x_2)=\delta_{mr}\delta_{ns} \tag{150}$$

$$\int_0^a\int_0^b D_f\left(\begin{array}{r}\frac{\partial^2\phi_{mn}(x_1,x_2)}{\partial x_1^2}\frac{\partial^2\phi_{rs}(x_1,x_2)}{\partial x_1^2}+2\frac{\partial^2\phi_{mn}(x_1,x_2)}{\partial x_1^2}\frac{\partial^2\phi_{rs}(x_1,x_2)}{\partial x_2^2}+\\+\frac{\partial^2\phi_{mn}(x_1,x_2)}{\partial x_2^2}\frac{\partial^2\phi_{rs}(x_1,x_2)}{\partial x_2^2}\end{array}\right)dx_1dx_2 \tag{151}$$
$$=\omega_{mn}^2\delta_{mr}\delta_{ns}$$

For a simply supported plate on all boundaries (SSSS) the mass-normalized eigenfunction is

$$\phi_{mn}(x_1,x_2)=\frac{2}{\sqrt{\rho abh}}\sin\left(\frac{m\pi}{a}x_1\right)\sin\left(\frac{n\pi}{b}x_2\right) \tag{152}$$

The undamped natural frequency of the mn-th vibration mode of the plate under short-circuit conditions ($R_l\to 0$), ω_{mn}, for a simply supported plate is

$$\omega_{mn}=\pi^2\left[\left(\frac{m}{a}\right)^2+\left(\frac{n}{b}\right)^2\right]\sqrt{\frac{D_f}{\rho h}} \tag{153}$$

The mechanical equation in modal coordinates can be obtained after substituting Eq. 149 into Eq. 148 then multiplying the latter by the mode shape, integrating over the surface area of the plate and applying the orthogonality conditions. The resulting modal mechanical

equation is

$$\frac{d^2\eta_{mn}}{dt^2} + 2\zeta_{mn}\omega_{mn}\frac{d\eta_{mn}}{dt} + \omega_{mn}\eta_{mn} - \theta_{mn}v(t) = f_{mn}(t) \tag{154}$$

where the modal electromechanical coupling term due to flexoelectricity is

$$\theta_{mn} = \mu_{1133}\left(\int_{x_1=0}^{a} \frac{\partial\phi_{mn}}{\partial x_2}\bigg|_0^b dx_1 + \int_{x_2=0}^{b} \frac{\partial\phi_{mn}}{\partial x_1}\bigg|_0^a dx_2\right) \tag{155}$$

and the mechanical forcing due to base excitation is

$$f_{mn}(t) = -m\frac{d^2w_b(t)}{dt^2}\int_0^a\int_0^b \phi_{mn}(x_1, x_2)dx_2dx_1 \tag{156}$$

In the presence of a finite resistive load connected across the electrodes of the plate, the flexoelectrically coupled circuit equation can be obtained from the integral

$$\frac{d}{dt}\left(\int_A \mathbf{D}\cdot\mathbf{n}dA\right) = \frac{v(t)}{R_l} \tag{157}$$

where the only contribution to the electric displacement is

$$D_3 = \varepsilon_{33}E_3 + \mu_{1133}\frac{\partial S_1}{\partial x_3} + \mu_{1133}\frac{\partial S_2}{\partial x_3} \tag{158}$$

Evaluating Eq. 157, the flexoelectrically coupled circuit equation is obtained as

$$\frac{\varepsilon_{33}ab}{h}\frac{dv(t)}{dt} + \frac{v(t)}{R_l} + \mu_{1133}\int_0^a\int_0^b\left(\frac{\partial^3 w}{\partial x_1^2\partial t} + \frac{\partial^3 w}{\partial x_2^2\partial t}\right)dx_2dx_1 = 0 \tag{159}$$

The modal electrical circuit equation is obtained by substituting Eq. 149 into Eq. 159 yielding

$$C\frac{dv(t)}{dt} + \frac{v}{R_l} + \sum_{m=1}^{\infty}\sum_{n=1}^{\infty}\theta_{mn}\frac{d\eta_{mn}}{dt} = 0 \tag{160}$$

where the capacitance is

$$C = \frac{ab}{h}\varepsilon_{33} \tag{161}$$

and the modal electromechanical coupling (θ_{mn}) due to the *direct* flexoelectric effect is the same as Eq. 155 that was obtained for the *converse* effect. This confirms symmetry in the fully coupled governing electroelastodynamic equations given by Eqs. 148 and 159 in physical coordinates and Eqs. 154 and 160 in modal coordinates.

For harmonic base excitation ($w_b(t) = W_0 e^{j\omega t}$), the modal forcing given by Eq. 156 is $f_{mn}(t) = F_{mn} e^{j\omega t}$, where the amplitude F_{mn} is

$$F_{mn} = \omega^2 m W_0 \int_0^a \int_0^b \phi_{mn}(x_1, x_2) dx_2 dx_1 \tag{162}$$

The steady-state modal mechanical response of the beam and the steady-state voltage response across the resistive load are also harmonic at the same frequency given as $\eta_{mn}(t) = H_{mn} e^{j\omega t}$ and $v(t) = V e^{j\omega t}$, respectively. The amplitudes H_{mn} and V are complexed valued. Substituting the harmonic responses into Eqs. 154 and 160 then solving for the amplitudes, the steady state vibration and voltage responses can be obtained as

$$w(x_1, x_2, t) = \sum_{m=1}^{\infty} \sum_{n=1}^{\infty} \left[\left(F_{mn} - \frac{j\omega\theta_{mn} \sum_{m=1}^{\infty} \sum_{n=1}^{\infty} \frac{\theta_{mn} F_{mn}}{{\omega_{mn}}^2 - \omega^2 + j2\zeta_{mn}\omega_{mn}\omega}}{j\omega C + \frac{1}{R_l} + \sum_{m=1}^{\infty} \sum_{n=1}^{\infty} \frac{j\omega\theta_{mn}^2}{{\omega_{mn}}^2 - \omega^2 + j2\zeta_{mn}\omega_{mn}\omega}} \right) \times \left(\frac{\phi_{mn}(x_1, x_2) e^{j\omega t}}{{\omega_{mn}}^2 - \omega^2 + j2\zeta_{mn}\omega_{mn}\omega} \right) \right] \tag{163}$$

$$v(t) = \frac{j\omega \sum_{m=1}^{\infty} \sum_{n=1}^{\infty} \frac{\theta_{mn} F_{mn}}{{\omega_{mn}}^2 - \omega^2 + j2\zeta_{mn}\omega_{mn}\omega}}{j\omega C + \frac{1}{R_l} + \sum_{m=1}^{\infty} \sum_{n=1}^{\infty} \frac{j\omega\theta_{mn}^2}{{\omega_{mn}}^2 - \omega^2 + j2\zeta_{mn}\omega_{mn}\omega}} e^{j\omega t} \tag{164}$$

6.2.2 Flexoelectric monolayer plate vibration response and current drawn for actuation

The governing equations in energy harvesting can be modified to represent the actuation problem similarly, such that there is no base excitation ($f_{mn}(t) = 0$) and the excitation is due to harmonic voltage input. The steady state mechanical response and current are obtained as

$$w_{rel}(x_1, x_2, t) = \sum_{m=1}^{\infty} \sum_{n=1}^{\infty} \frac{\theta_{mn} \phi_{mn}(x_1, x_2)}{\omega_{mn}^2 - \omega^2 + j2\zeta_{mn}\omega_{mn}\omega} V e^{j\omega t} \tag{165}$$

$$i(t) = j\omega \left(C + \sum_{m=1}^{\infty} \sum_{n=1}^{\infty} \frac{\theta_{mn}^2}{\omega_{mn}^2 - \omega^2 + j2\zeta_{mn}\omega_{mn}\omega} \right) V e^{j\omega t} \tag{166}$$

6.2.3 Flexoelectric-piezoelectric bimorph plate for energy harvesting

For the flexoelectric-piezoelectric Kirchhoff thin bimorph plate, the mechanical stress state accounting for the *converse* flexoelectric and piezoelectric effects is expressed as

$$\begin{aligned} T_{11} &= c_{1111}S_{11} + c_{1122}S_{22} - e_{311}E_3 + f_{1133}\frac{\partial P_3}{\partial x_3} \\ T_{22} &= c_{1122}S_{11} + c_{1111}S_{22} - e_{311}E_3 + f_{1133}\frac{\partial P_3}{\partial x_3} \\ T_{12} &= c_{1212}S_{12} \end{aligned} \tag{167}$$

where e_{31} is the piezoelectric constant.

Substituting the stresses and strains given by Eqs. 137 and 167 into the internal bending and twisting moment expressions given Eqs. 135 and 136 and evaluating the integrals yields

$$\begin{aligned} M_{11} = -D_p\left(\frac{\partial^2 w}{\partial {x_1}^2} + \frac{c_{1122}}{c_{1111}}\frac{\partial^2 w}{\partial {x_2}^2}\right) + \left(\frac{1}{2}e_{311}h_p + \mu_{1133}\right)v(t)\times \\ [H(x_1) - H(x_1 - a)]\,[H(x_2) - H(x_2 - b)] \end{aligned} \tag{168}$$

$$\begin{aligned} M_{22} = -D_p\left(\frac{c_{1122}}{c_{1111}}\frac{\partial^2 w}{\partial {x_1}^2} + \frac{\partial^2 w}{\partial {x_2}^2}\right) + \left(\frac{1}{2}e_{311}h_p + \mu_{1133}\right)v(t)\times \\ [H(x_1) - H(x_1 - a)]\,[H(x_2) - H(x_2 - b)] \end{aligned} \tag{169}$$

$$M_{12} = -D_p\frac{2c_{1212}}{c_{1111}}\frac{\partial^2 w}{\partial x_1 \partial x_2} \tag{170}$$

where the flexural rigidity of the piezoelectric bimorph plate is

$$D_p = c_{1111}\frac{2{h_p}^3}{3} \tag{171}$$

The electromechanically coupled Kirchhoff bimorph plate equation for transverse vibrations is then obtained from Eq. 134 (assuming a transversely isotropic material)as

$$\begin{aligned} D_p\left[\frac{\partial^4 w}{\partial x_1^4} + 2\frac{\partial^4 w}{\partial x_1^2 \partial x_2^2} + \frac{\partial^4 w}{\partial x_2^4}\right] + c\frac{\partial w}{\partial t} + m\frac{\partial^2 w}{\partial t^2} - \left(\frac{1}{2}e_{311}h_p + \mu_{1133}\right)v(t)\times \\ \left(\begin{array}{l} \left[\dfrac{d\delta(x_1)}{d(x_1)} - \dfrac{d\delta(x_1 - a)}{dx_1}\right][H(x_2) - H(x_2 - b)] \\ + [H(x_1) - H(x_1 - a)]\left[\dfrac{d\delta(x_2)}{d(x_2)} - \dfrac{d\delta(x_2 - b)}{dx_2}\right] \end{array}\right) = f(x_1, x_2, t) \end{aligned} \tag{172}$$

Following similar modal analysis as the done in the previous section for a simply supported plate (SSSS), the mechanical equation in modal coordinates is obtained as

$$\frac{d^2\eta_{mn}}{dt^2} + 2\zeta_{mn}\omega_{mn}\frac{d\eta_{mn}}{dt} + \omega_{mn}\eta_{mn} - \theta^p_{mn}v(t) = f_{mn}(t) \tag{173}$$

where the modal electromechanical coupling due to the combined flexoelectricity and piezoelectricity is

$$\theta_{mn}^{p} = \left(\frac{1}{2}e_{311}h_p + \mu_{1133}\right)\left(\int_{x_1=0}^{a} \left.\frac{\partial\phi_{mn}}{\partial x_2}\right|_0^b dx_1 + \int_{x_2=0}^{b} \left.\frac{\partial\phi_{mn}}{\partial x_1}\right|_0^a dx_2\right) \tag{174}$$

where ϕ_{mn} is the mass normalized mode shape of the simply supported bimorph plate

$$\phi_{mn}(x_1, x_2) = \frac{2}{\sqrt{\rho 2abh_p}} \sin\left(\frac{m\pi}{a}x_1\right)\sin\left(\frac{n\pi}{b}x_2\right) \tag{175}$$

that satisfies Eqs. 150 and 151. The undamped natural frequency of the mn-th vibration mode of the bimorph plate under short-circuit conditions ($R_l \to 0$), ω_{mn}, for a simply supported plate is

$$\omega_{mn} = \pi^2\left[\left(\frac{m}{a}\right)^2 + \left(\frac{n}{b}\right)^2\right]\sqrt{\frac{D_p}{2\rho h_p}} \tag{176}$$

The electric displacement of the flexoelectric-piezoelectric bimorph Kirchhoff plate is

$$D_3 = \varepsilon_{33}E_3 + e_{311}S_{11} + e_{311}S_{22} + \mu_{1133}\frac{\partial S_{11}}{\partial x_3} + \mu_{1133}\frac{\partial S_{22}}{\partial x_3} \tag{177}$$

Applying the current balance given by Eq. 157 and performing modal analysis, similar to the previous section, yields the flexoelectrically and piezoelectrically coupled circuit equation for the Kirchhoff bimorph plate:

$$C_p\frac{dv(t)}{dt} + \frac{v}{R_l} + \sum_{m=1}^{\infty}\sum_{n=1}^{\infty}\theta_{mn}^{p}\frac{d\eta_{mn}}{dt} = 0 \tag{178}$$

where the capacitance is

$$C_p = \frac{ab}{2h_p}\varepsilon_{33} \tag{179}$$

and the modal electromechanical coupling (θ_{mn}^{p}) due to the *direct* flexoelectric and piezoelectric effects is the same as Eq. 174 that was obtained for the *converse* effects.

The steady state vibration and voltage responses for the bimorph plate can be obtained as described in the previous section yielding

$$w(x_1, x_2, t) = \sum_{m=1}^{\infty}\sum_{n=1}^{\infty}\left[\left(F_{mn} - \frac{j\omega\theta_{mn}^{p}\sum_{m=1}^{\infty}\sum_{n=1}^{\infty}\frac{\theta_{mn}^{p}F_{mn}}{{\omega_{mn}}^2-\omega^2+j2\zeta_{mn}\omega_{mn}\omega}}{j\omega C_p + \frac{1}{R_l} + \sum_{m=1}^{\infty}\sum_{n=1}^{\infty}\frac{j\omega\left(\theta_{mn}^{p}\right)^2}{{\omega_{mn}}^2-\omega^2+j2\zeta_{mn}\omega_{mn}\omega}}\right)\times \left(\frac{\phi_{mn}(x_1,x_2)e^{j\omega t}}{{\omega_{mn}}^2-\omega^2+j2\zeta_{mn}\omega_{mn}\omega}\right)\right] \tag{180}$$

$$v(t) = \frac{j\omega \sum_{m=1}^{\infty}\sum_{n=1}^{\infty} \frac{\theta_{mn}^{p} F_{mn}}{{\omega_{mn}}^{2}-\omega^{2}+j2\zeta_{mn}\omega_{mn}\omega}}{j\omega C_p + \frac{1}{R_l} + \sum_{m=1}^{\infty}\sum_{n=1}^{\infty} \frac{j\omega\left(\theta_{mn}^{p}\right)^{2}}{{\omega_{mn}}^{2}-\omega^{2}+j2\zeta_{mn}\omega_{mn}\omega}} e^{j\omega t} \tag{181}$$

6.2.4 Flexoelectric-piezoelectric bimorph plate vibration response and current drawn for actuation

The governing equations in energy harvesting can be modified to represent the actuation problem similarly, such that there is no base excitation ($f_{mn}(t) = 0$) and the excitation is due to harmonic voltage input. The steady state mechanical response and current for dynamic actuation of the Kirchhoff bimorph plate are obtained as

$$w_{rel}(x_1, x_2, t) = \sum_{m=1}^{\infty}\sum_{n=1}^{\infty} \frac{\theta_{mn}^{p}\phi_{mn}(x_1, x_2)}{\omega_{mn}^{2} - \omega^{2} + j2\zeta_{mn}\omega_{mn}\omega} V e^{j\omega t} \tag{182}$$

$$i(t) = j\omega\left(C_p + \sum_{m=1}^{\infty}\sum_{n=1}^{\infty} \frac{\left(\theta_{mn}^{p}\right)^{2}}{\omega_{mn}^{2} - \omega^{2} + j2\zeta_{mn}\omega_{mn}\omega}\right) V e^{j\omega t} \tag{183}$$

6.3 Size effects on electromechanical coupling coefficient

Recall from previous chapters, the dynamic definition of the modal electromechanical coupling coefficient can be obtained based on the difference between the open-circuit and short-circuit natural frequencies [1, 49]

$$k^2 = \frac{\left(\omega_{mn}^{oc}\right)^2 - \left(\omega_{mn}^{sc}\right)^2}{\left(\omega_{mn}^{oc}\right)^2} \tag{184}$$

Substituting the respective functions into Eq. 184, for the first vibration mode ($m = 1$, $n = 1$) of a simply supported flexoelectric monolayer plate, the coupling coefficient is

$${k_f}^2 = \frac{1}{\frac{c_{1111}\varepsilon_{33}}{\mu_{1133}^{2}}\frac{\pi^4}{768}h^2 + 1} \tag{185}$$

Similarly, for the first vibration mode ($m = 1$, $n = 1$) of a simply supported piezoelectric bimorph plate, the coupling coefficient is

$${k_p}^2 = \frac{1}{\frac{c_{1111}\varepsilon_{33}\pi^4}{48(e_{311}+2\mu_{1133}/h_p)^2} + 1} \tag{186}$$

Equations 185 and 186 capture the thickness dependence of the modal electromechanical coupling coefficient.

6.4 Case studies and results

In this section, simulations are performed to show the effect of thickness on the electromechanical coupling and the frequency response behavior of a flexoelectric monolayer and flexoelectric-piezoelectric bimorph plate under bending vibrations for energy harvesting and actuation. The monolayer harvester simulations are performed for Strontium Titanate (STO) using the elastic [9, 44] and dielectric [89, 3] properties of $c_{1111} = 318$ GPa, $c_{1122} = 102.4$ GPa, $\rho = 5116$ kg/m^3, and $\varepsilon_{33} = 2.66$ nF/m (for the room temperature relative permittivity [89, 88, 3], $\varepsilon_{33}/\varepsilon_0 = 300$), and using the atomistic flexoelectric coefficient value [60] of $\mu_{1133} = -3.75 \times 10^{-9}$ C/m. The bimorph flexoelectric-piezoelectric harvester simulations are performed for Barium Titanate (BTO) using the atomistic value presented by Maranganti and Sharma [60] of $\mu_{1133} = -5.463 \times 10^{-9}$ C/m along with the necessary material properties [8, 29]: $e_{311} = -4.4$ C/m^2, $c^E_{1111} = 166$ GPa ,$c^E_{1122} = 76.5$ GPa, $\varepsilon^s_{33} = 12.56$ nF/m, and $\rho = 5720$ kg/m^3.

6.4.1 Size effects on electromechanical coupling

The electromechanical coupling coefficients due to flexoelectric and combined flexoelectric and piezoelectric energy conversion are plotted for a range of plate thicknesses in Figs. 30a and 30b, respectively. The focus is placed on the fundamental bending vibration mode ($m = 1,\ n = 1$), and the plate thicknesses in the simulations range from 1 mm to 1 nm. As stated previously based on Eqs. 185 and 186, the coupling coefficient increases with decreased thickness for both the monolayer and bimorph plates. The isolated flexoelectric and piezoelectric coupling coefficients are also shown in Fig. 30b and it is seen that only submicron scale (mainly below ~ 100 nm) does the flexoelectric effect become appreciable, and it strongly enhances the overall electromechanical coupling of the piezoelectric bimorph. For micron thickness and above the overall electromechanical coupling is merely due to bulk piezoelectricity; however, the electromechanical coupling is dramatically enhanced due to flexoelectricity for thickness levels approaching the nanoscale.

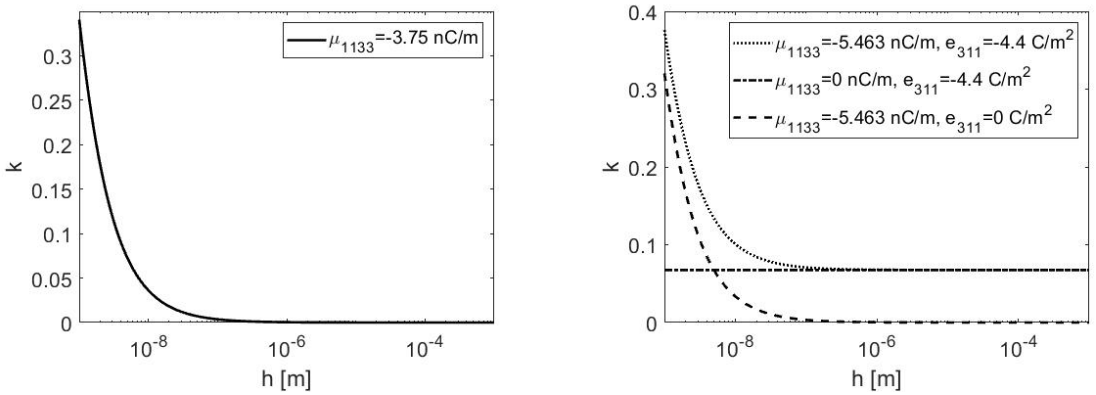

(a) **(b)**

Figure 30: (a) Centrosymmetric STO monolayer plate and **(b)** piezoelectric BTO bimorph plate with surface electrodes (that are perpendicular to the thickness direction) connected to a resistive electrical load for energy harvesting

6.4.2 Electromechanical frequency response for flexoelectric monolayer plate in energy harvesting

In this section, the electromechanical frequency response functions of flexoelectric thin monolayer plate energy harvesters under base excitation are simulated with a focus on the first bending mode ($m = 1,\ n = 1$) for a broad range of electrical load resistance values. Three different geometric scales are explored, spanning from mm-scale to nm-scale thickness. For each case the length/width/thickness aspect ($a/b/h$) ratio is fixed at 100/100/1. The plates have perfectly conductive surface electrodes on the faces that are perpendicular to the direction of transverse base excitation(Fig. 29). A mechanical quality factor (Q) of 50 is assumed, yielding an approximate modal mechanical damping ratio of 1% of the critical damping (i.e. $\zeta_1 = 1/2Q = 0.01$ for the first bending mode). The results are presented as frequency response magnitude maps normalized by the base acceleration quantified in terms of gravitational acceleration as in the previous chapters. To capture optimal load in power generation and respective trends with changing load, a range of electrical resistive load values spanning from short- to open-circuit conditions (10 Ω to 100 MΩ) are simulated for each case.

The voltage output (per base acceleration) frequency response maps (obtained from Eq. 164) for all three geometric scales are shown in Fig. 31a. The excitation frequency is

normalized by the fundamental short-circuit natural frequency (ω_{11}) on the vertical axis. For all cases, the voltage increases monotonically with increases resistive load as expected for an energy harvester [37]. As an indication of very low electromechanical coupling, the resonance frequencies of the 1 mm and 1 μm cases are insensitive to change in resistive load. The flexoelectric coupling coefficients for the 1 mm and 1 μm cases are (obtained from Eq. 185 or Figs. 31a.i and 31a.ii) $k \approx 3.6 \times 10^{-7}$ and $k \approx 3.6 \times 10^{-4}$, respectively. The 1 nm thickness case is shown in Fig. 31a.iii. For this case, the resonance frequency is sensitive in change in resistive load from short- to open-circuit, as an indication of increased electromechanical coupling. The electromechanical coupling for the 1 nm case is $k \approx 0.34$. The coupling coefficients indicate an increase in electromechanical coupling of nearly 6 orders of magnitude when reducing the thickness from mm-scale to nm-scale.

As done in previous chapters, the electric current flowing to the resistive load is obtained from the voltage output using Ohm's law. The current output (per base acceleration) frequency response maps are shown the for STO monolayer plate harvesters in Fig. 31b. For all cases, the current decreases monotonically with increased resistive load. As with the voltage output frequency response maps, similar trends in the flexoelectric coupling coefficient are seen for each case study. The 1 mm and 1 μm cases display no noticeable shift in resonance frequencies (Figs. 31b.i and 31b.ii), as a result of low electromechanical coupling. However, for the 1 nm thickness case significant shift in frequency is observed (Fig. 31b.iii) due to the increased electromechanical coupling.

Next, the electrical power output (per base acceleration squared) is simulated,as done in previous chapters, for all three geometric scales. The resulting graphs are shown in Fig. 32a. The optimal load for peak power output can be determined for each case from the power output frequency response maps. The 1 mm and 1 μm cases power output frequency response maps show the resonance frequency to be insensitive to change in resistive load, as seen with the previous frequency response maps. As a result, a single optimal load for peak power output is observed for both cases around 10 kΩ. The 1 nm case, however, exhibits two peak values for two distinct optimal loads, $\sim$ 1kΩ and $\sim$ 10kΩ, at the short- and open-circuit resonances, respectively. The same power output can be extracted at the

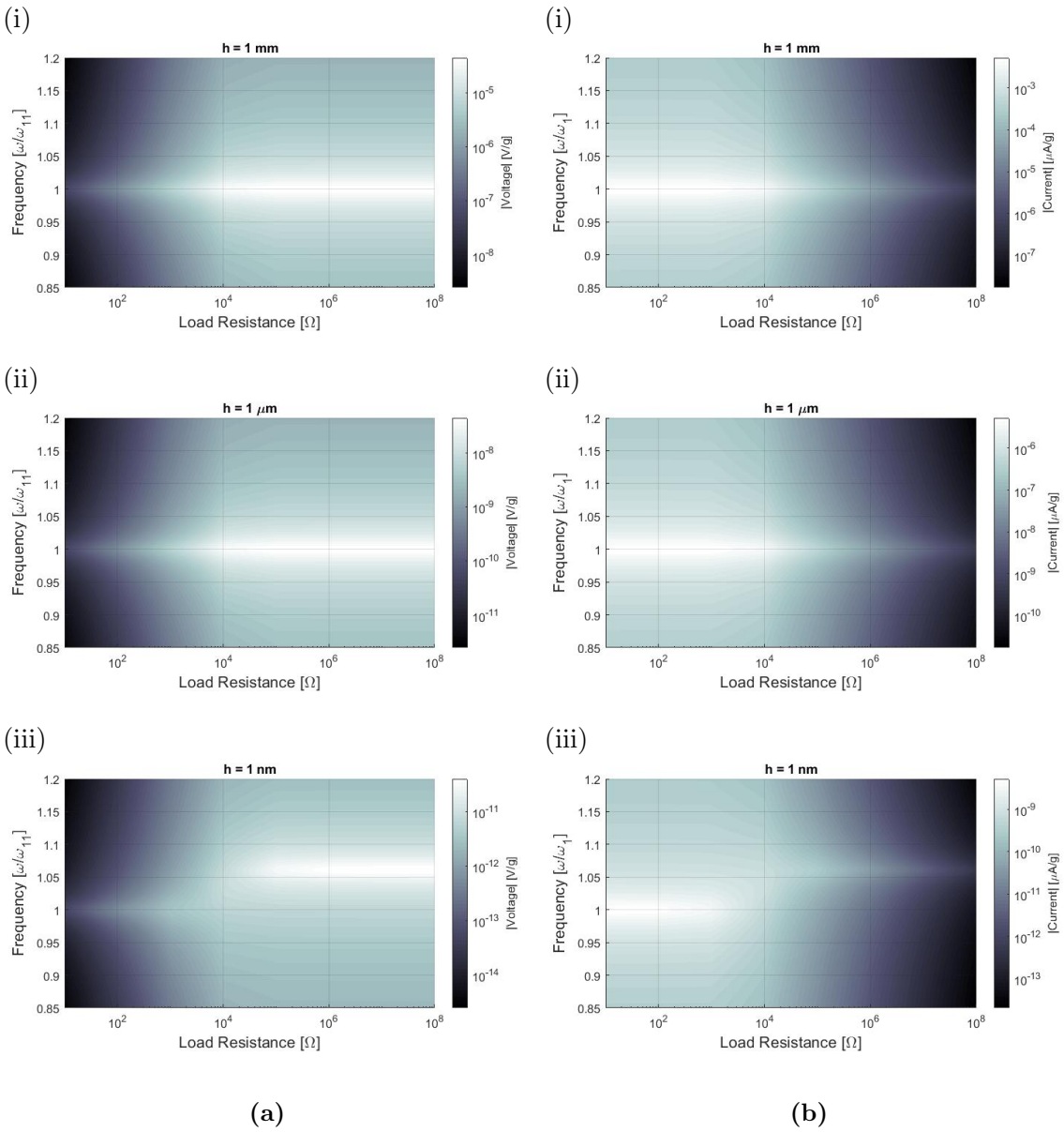

Figure 31: **(a)** Voltage output frequency response vs. load resistance maps (in magnitude form and per base acceleration) and **(b)** current output frequency response vs. load resistance maps (in magnitude form and per base acceleration) for cantilevered STO thin plate harvesters with a fixed aspect ratio of 100/100/1 ($a/b/h$) for three different geometric scales with the following thickness (h) values: (i) 1 mm, (ii) 1 μm, and (iii) 1 nm.

short-circuit frequency or at the open circuit frequency. The existence of two peaks in the power output is indication of a strongly coupled and lightly damped system.

Finally, the structural response of the STO plate while generating electricity from strain gradient fluctuations in response to mechanical base excitation is simulated for each geometric case. The motion of the plate can be evaluated at any position (x_1,x_2) using Eq.

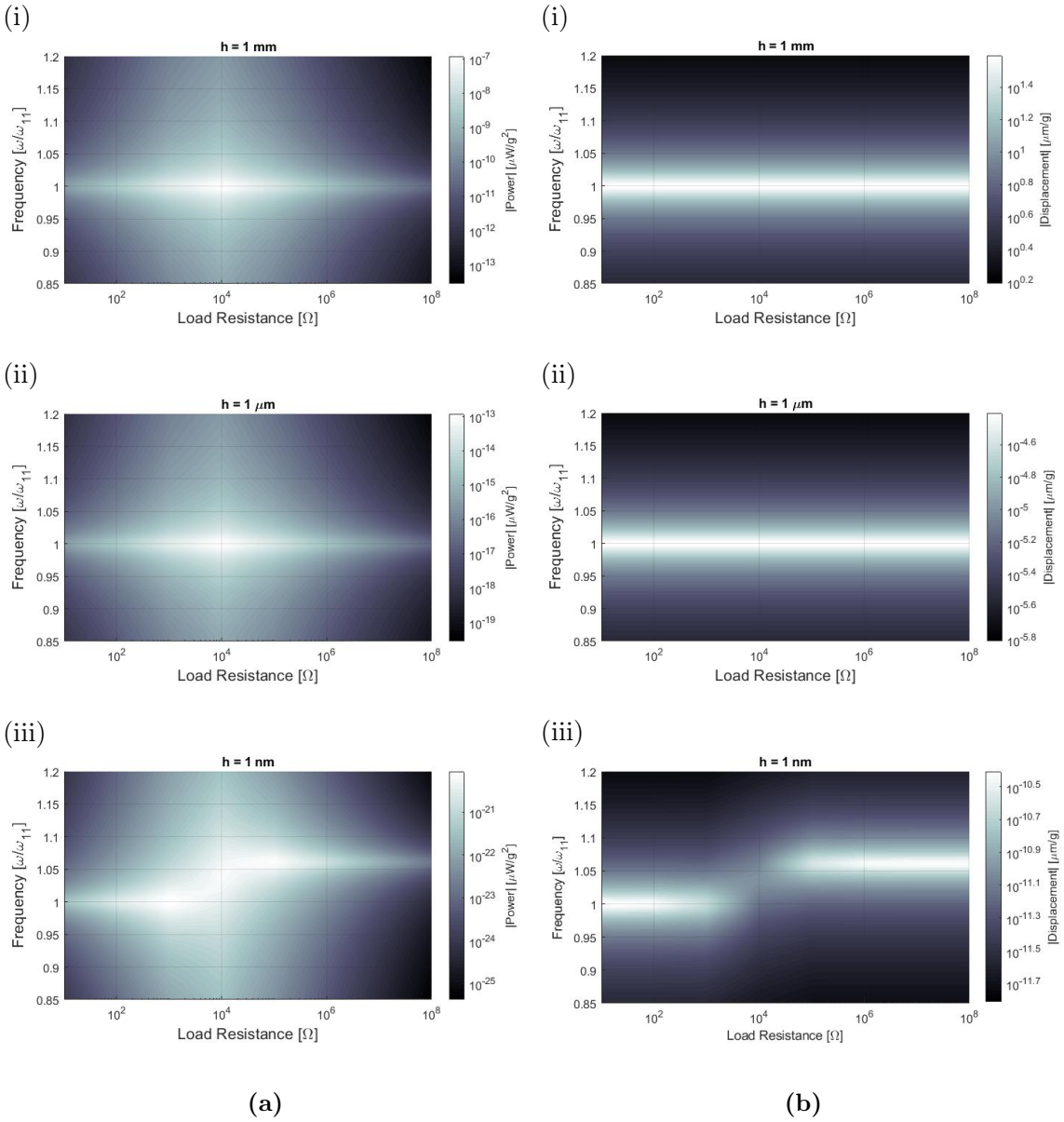

Figure 32: **(a)** Power output frequency response vs. load resistance maps (in magnitude form and per base acceleration squared) and **(b)** displacement frequency response vs. load resistance maps (in magnitude form and per base acceleration) for cantilevered STO thin plate harvesters with a fixed aspect ratio of 100/100/1 ($a/b/h$) for three different geometric scales with the following thickness (h) values: (i) 1 mm, (ii) 1 μm, and (iii) 1 nm.

163. The displacement frequency response maps (per base acceleration) measured at the center of the plate ($x_1 = a/2$, $x_2 = b/2$) are shown in Fig. 32b for all three cases. As another manifestation of weak electromechanical coupling, for the 1 mm and 1 μm cases, the vibration response of the plate is insensitive to change in electrical load resistance (Figs. 32b.i and 32b.ii). Although some power output is delivered to the electrical load according to

Figs. 32a.i and 32a.ii, the level of this electrical output is so small that it is negligible as compared to mechanical (vibrational) energy of the harvester (confirmed by the coupling coefficient values). This small level of electricity production does not alter the vibration response although the converse effect is taken into account in the model (i.e., the converse flexoelectric effect is negligible at these geometric scales). Therefore, Joule heating in the resistive load does not create any significant dissipation in the vibration response of the STO plate as a result of weak electromechanical coupling. However, as shown previously for the 1 nm case, the electromechanical coupling is relatively strong which results in the plate vibrational response being sensitive to change in electrical load (Fig. 32b.iii). Significant shunt damping is observed at certain load resistance values, analogous to piezoelectric shunt damping [50].

6.4.3 Electromechanical frequency response for flexoelectric monolayer plate in actuation

The same modeling framework is also employed to understand the electromechanical response of the monolayer plate in the case of electrical excitation for the same set of system parameters. Of interest, is the displacement frequency response (structural response for unit actuation voltage input) from Eq. 165 and the admittance frequency response (amount of current drawn for unit actuation voltage input) calculated from Eq. 166. The displacement (measured at the center, $x_1 = a/2$ and $x_2 = b/2$) and admittance frequency responses are shown in Figs. 33a and 33b, respectively. These frequency response functions show, once again, that significant electromechanical coupling only occurs at the nm-scale.

6.4.4 Electromechanical frequency response at steady state for flexoelectric-piezoelectric bimorph plate for energy harvesting

In this section, the electromechanical frequency response functions of flexoelectric-piezoelectric thin plate energy harvesters under base excitation are simulated with a focus on the first bending mode ($m = 1,\ n = 1$) for a broad range of electrical load resistance values. As in the previous section, three different geometric scales are explored, spanning from mm-scale to nm-scale thickness. For each case the length/width/thickness aspect ($a/b/h,\ h = 2h_p$) ratio is fixed at 100/100/1. The plates have perfectly conductive surface electrodes on the

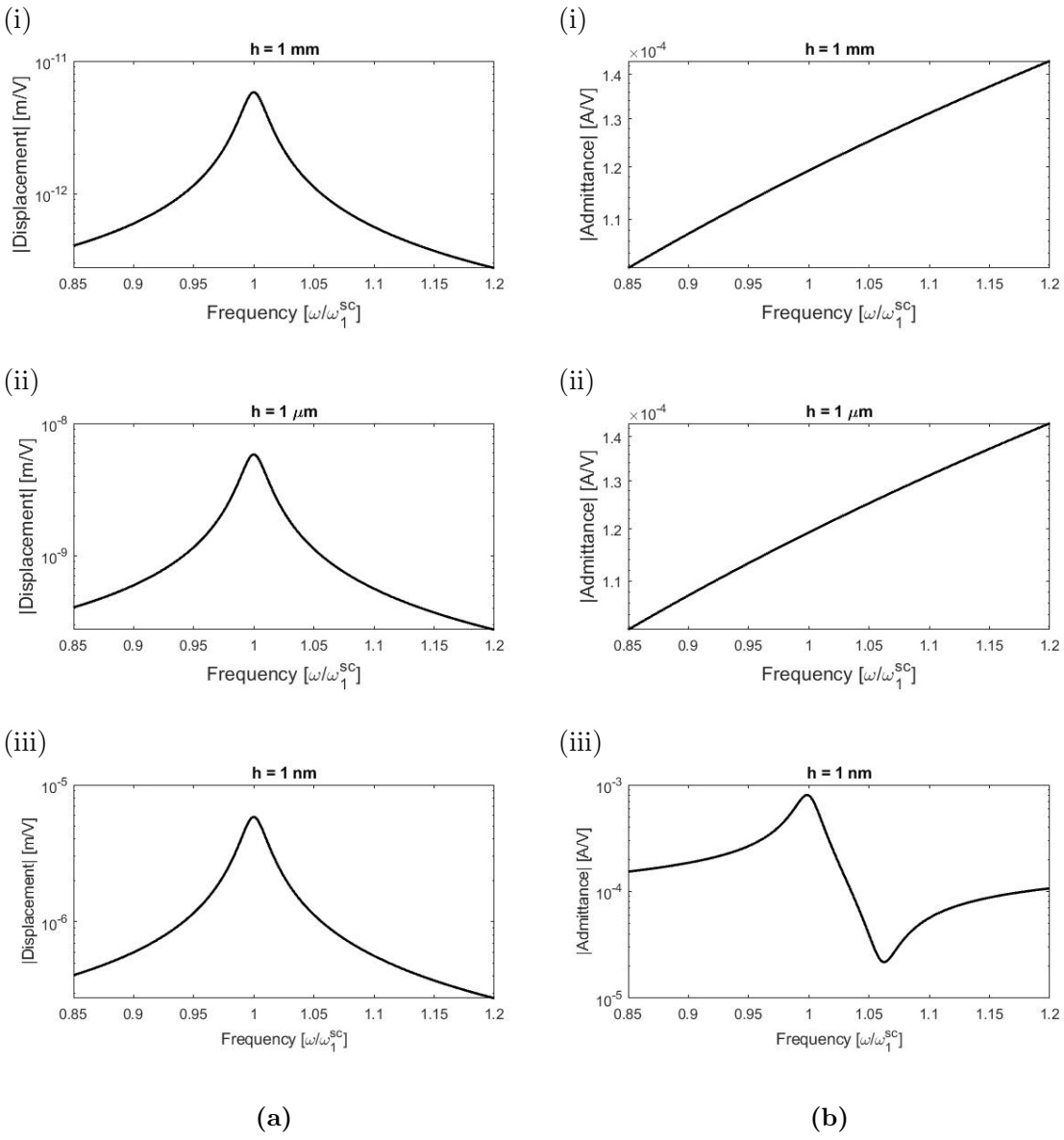

Figure 33: **(a)** Displacement and **(b)** admittance frequency response functions (in magnitude form) for actuation of simply supported STO monolayer plate with a fixed aspect ratio of 100/100/1 ($a/b/h$) for three different geometric scales with the following thickness (h) values: (i) 1 mm, (ii) 1 μm, and (iii) 1 nm.

faces that are perpendicular to the direction of transverse base excitation(Fig. 29). A mechanical quality factor (Q) of 50 is assumed, yielding an approximate modal mechanical damping ratio of 1% of the critical damping (i.e. $\zeta_1 = 1/2Q = 0.01$ for the first bending mode). The results are presented as frequency response magnitude maps normalized by the base acceleration quantified in terms of gravitational acceleration as in the previous chapters. To capture optimal load in power generation and respective trends with changing load,

a range of electrical resistive load values spanning from short- to open-circuit conditions (10 Ω to 100 MΩ) are simulated for each case.

The voltage output (per base acceleration) frequency response maps (obtained from Eq. 181) for all three geometric scales are shown in Fig. 34a. The excitation frequency is normalized by the fundamental short-circuit natural frequency (ω_{11}) on the vertical axis. For all cases, the voltage increases monotonically with increases resistive load as expected for a piezoelectric energy harvester [37]. The resonance frequencies of the 1 mm and 1 μm cases are insensitive to change in resistive load as an indication of very low electromechanical coupling. The combined flexoelectric-piezoelectric coupling coefficients for the 1 mm and 1 μm cases are (obtained from Eq. 186 or Figs. 34a.i and 34a.ii) $k \approx 0.0675$ and $k \approx 0.0678$, respectively. These values are roughly the bulk piezoelectric value confirming negligible contribution from flexoelectricity at these geometric scales. The 1 nm thickness case, shown in Fig. 31a.iii, displays a sensitivity in resonance frequency to change in electrical load from short- to open-circuit, as an indication of increased electromechanical coupling. The significant electromechanical coupling is confirmed by the flexoelectric-piezoelectric coupling coefficient value of $k \approx 0.376$, most of which is due to flexoelectricity.

The electric current flowing to the resistive load is obtained from the voltage output using Ohm's law. The current output (per base acceleration) frequency response maps are shown the for BTO bimorph plate harvesters in Fig. 34b. For all cases, the current decreases monotonically with increased resistive load. As with the voltage output frequency response maps, the 1 mm and 1 μm cases display no noticeable shift in resonance frequencies, Figs. 31b.i and 31b.ii, as a result of low electromechanical coupling. However, for the 1 nm thickness case significant shift in frequency is observed (Fig. 31b.iii) due to the increased electromechanical coupling, as a result of flexoelectric contribution.

The electrical power output (per base acceleration squared) is simulated, for all three geometric scales of the BTO bimorph plate with the resulting graphs shown in Fig. 32a. The optimal load for peak power output can be determined for each case from these power output frequency response maps. The 1 mm and 1 μm cases power output frequency response maps show the resonance frequency to be insensitive to change in resistive load, as seen with the

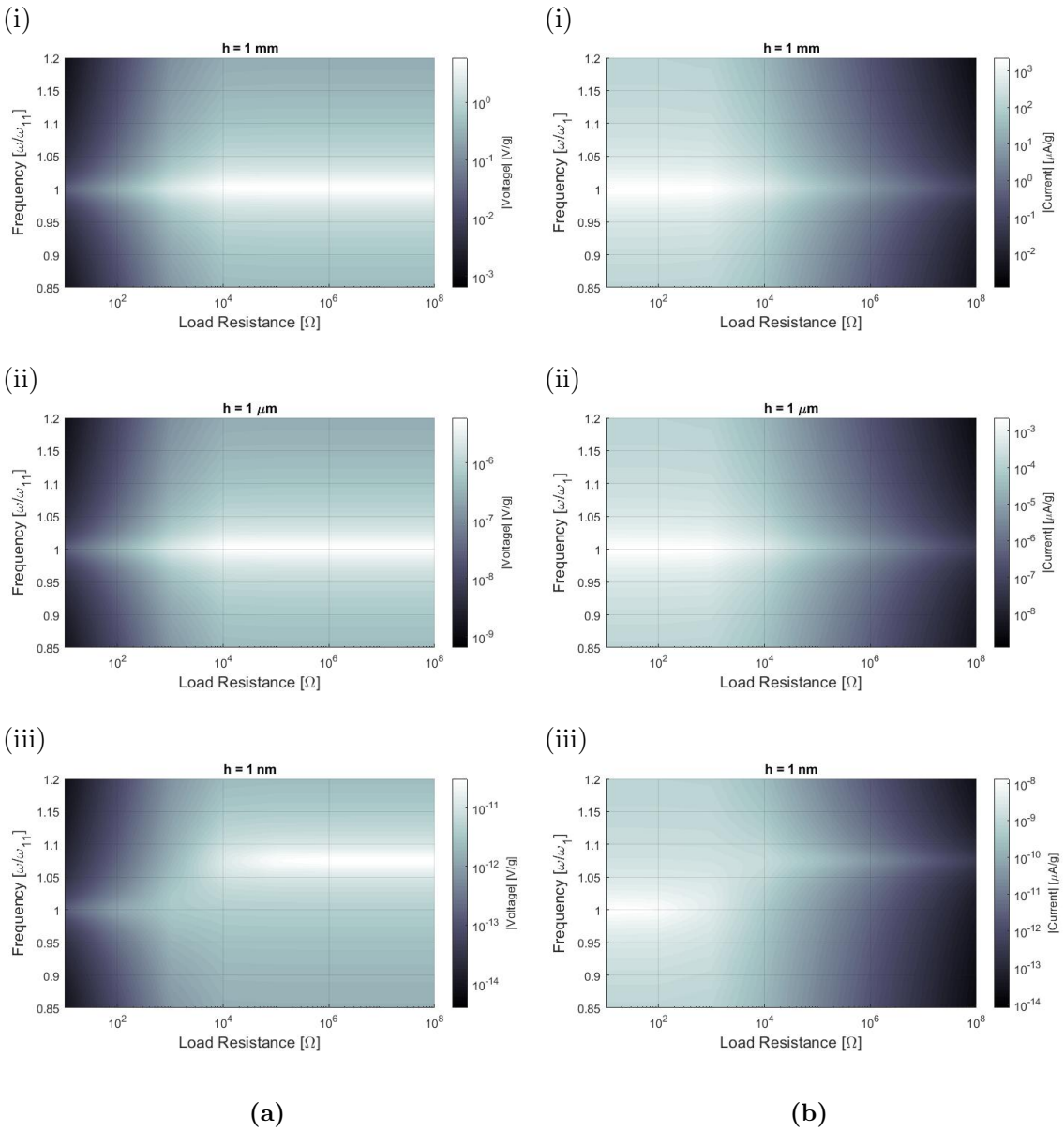

Figure 34: **(a)** Voltage output frequency response vs. load resistance maps (in magnitude form and per base acceleration) and **(b)** current output frequency response vs. load resistance maps (in magnitude form and per base acceleration) for cantilevered BTO thin bimorph plate harvesters with a fixed aspect ratio of 100/100/1 ($a/b/h$, $h = 2h_p$) for three different geometric scales with the following thickness (h) values: (i) 1 mm, (ii) 1 μm, and (iii) 1 nm.

previous frequency response maps. For this reason, a single optimal load for peak power output is observed for both cases around 1 kΩ. However, two peak values for two distinct optimal loads, $\sim$ 1kΩ and $\sim$ 10kΩ, at the short- and open-circuit resonances, respectively, are observed for the 1 nm case. As a result, the same power output can be extracted

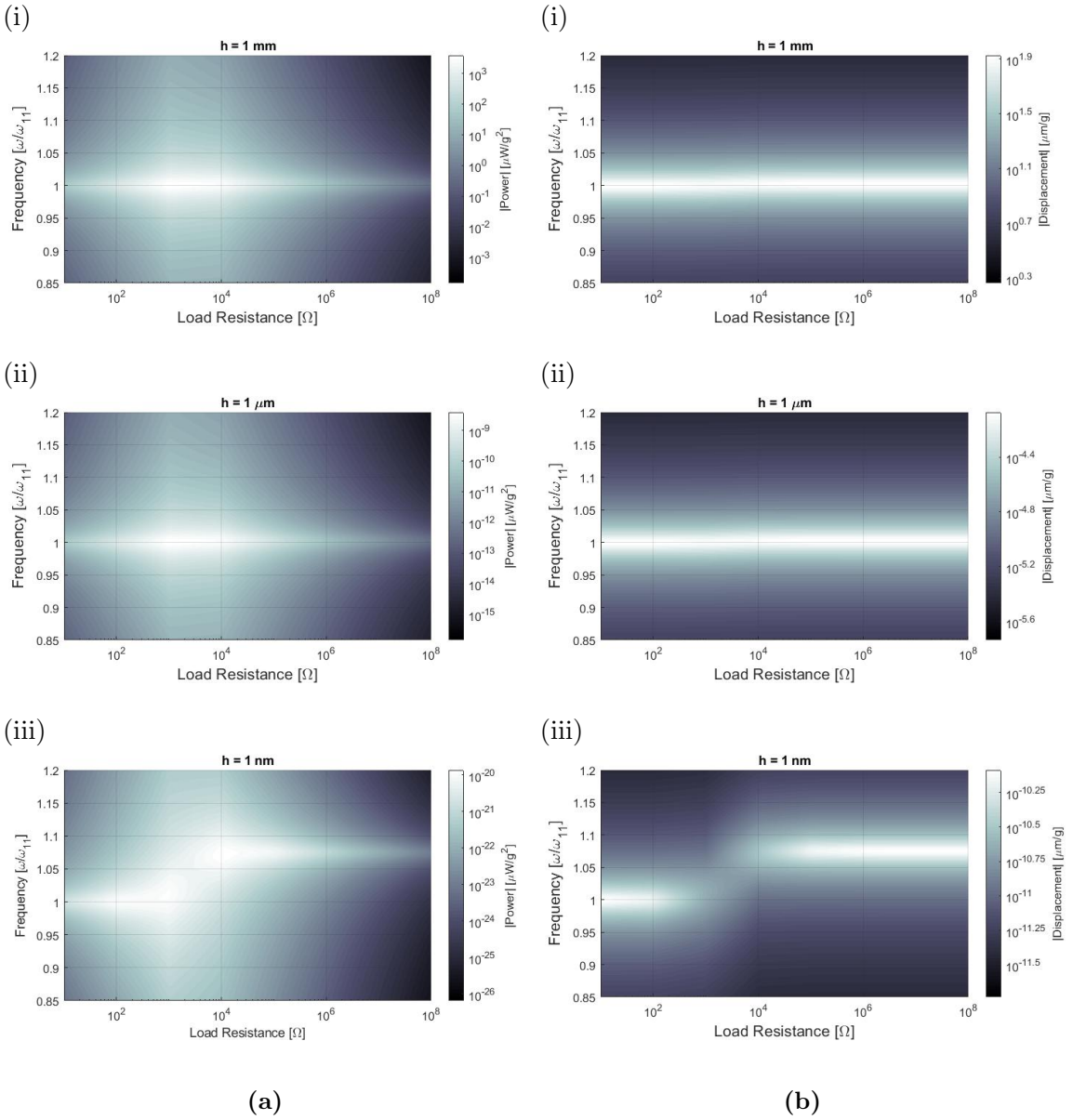

Figure 35: (a) Power output frequency response vs. load resistance maps (in magnitude form and per base acceleration squared) and **(b)** displacement frequency response vs. load resistance maps (in magnitude form and per base acceleration) for cantilevered BTO thin plate harvesters with a fixed aspect ratio of 100/100/1 ($a/b/h$, $h = 2h_p$) for three different geometric scales with the following thickness (h) values: (i) 1 mm, (ii) 1 μm, and (iii) 1 nm.

at the short-circuit frequency or at the open circuit frequency. This is an indication of a relatively strongly coupled harvester configuration, as a result of the electromechanical coupling enhancement due to the flexoelectric effect.

Lastly, the structural response of the BTO bimorph plate while generating electricity from strain gradient (flexoelectricity) and strain (piezoelectricity) fluctuations in response to

mechanical base excitation is simulated for each geometric case. Using Eq. 180, the motion of the plate can be evaluated at any position (x_1,x_2). The displacement frequency response maps (per base acceleration) measured at the center of the plate ($x_1 = a/2$, $x_2 = b/2$) are shown in Fig. 32b for all three cases. The vibration response of the plate is insensitive to change in electrical load resistance (Figs. 35b.i and 35b.ii), as another manifestation of weak electromechanical coupling, for the 1 mm and 1 μm cases. Even though some power output is delivered to the electrical load according to Figs. 35a.i and 35a.ii, the level of this electrical output is negligible as compared to vibrational energy of the harvester (confirmed by the coupling coefficient values). This small level of electricity production does not alter the vibration response although the converse effect is taken into account in the model (i.e., the converse flexoelectric effect is negligible at these geometric scales). Consequently, Joule heating in the electrical load does not create any significant dissipation in the vibration response of the BTO plate as a result of weak electromechanical coupling. However, as shown previously for the 1 nm case, the electromechanical coupling is relatively strong which results in the plate vibrational response being sensitive to change in electrical load (Fig. 32b.iii) and significant shunt damping is observed at certain load resistance values.

6.4.5 Electromechanical frequency response for flexoelectric piezoelectric bimorph plate in actuation

The same modeling framework is also employed to understand the electromechanical response of the bimorph plate in the case of electrical excitation for the same set of system parameters. Of interest, is the displacement frequency response (structural response for unit actuation voltage input) from Eq. 182 and the admittance frequency response (amount of current drawn for unit actuation voltage input) calculated from Eq. 183. The displacement (measured at the center, $x_1 = a/2$ and $x_2 = b/2$ and admittance frequency responses are shown in Figs. 36a and 36b, respectively. These frequency response functions show, once again, that significant electromechanical coupling only occurs at the nm-scale. Particularly, in the admittance graphs shown in Fig. 36b, the relative frequency difference between the resonance and antiresonance frequencies is a measure of electromechanical coupling. These frequency response functions show, once again, that the overall coupling is enhanced due

to flexoelectricity only at the nanometer scale.

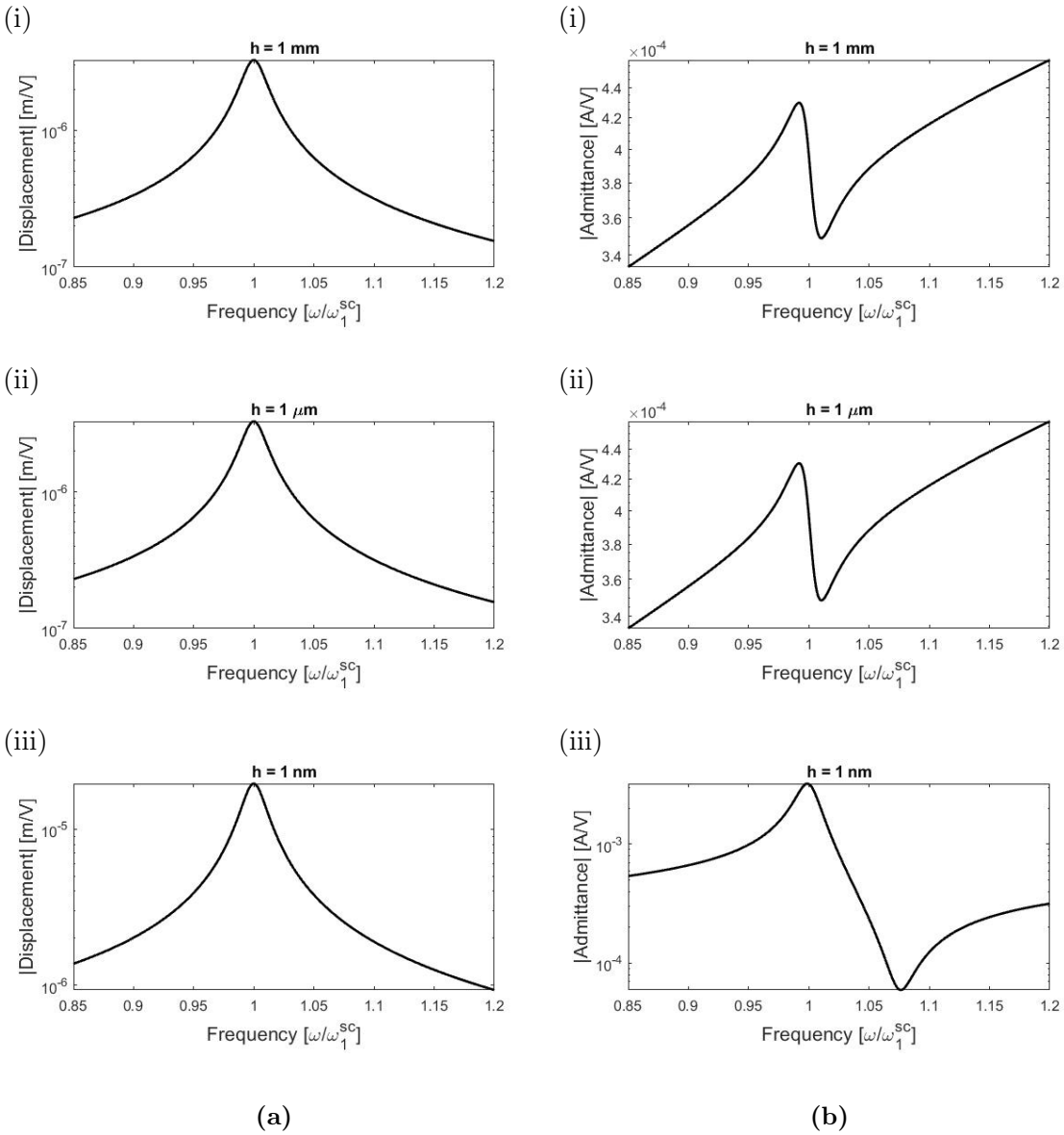

Figure 36: **(a)** Displacement and **(b)** admittance frequency response functions (in magnitude form) for actuation of simply supported BTO bimorph plate with a fixed aspect ratio of 100/100/1 ($a/b/h$, $h = 2h_p$) for three different geometric scales with the following thickness (h) values: (i) 1 mm, (ii) 1 μm, and (iii) 1 nm.

6.5 Conclusions

An electroelastodynamic framework is developed and analyzed for flexoelectric energy harvesting from strain gradient fluctuations in centrosymmetric dielectrics and piezoelectric

materials, by accounting for the presence of a finite electrical load across the surface electrodes as well as two-way electromechanical coupling. The model is then extended to the dynamic actuation problem for a fixed base. The flexoelectric and combined flexoelectric-piezoelectric energy harvester and actuation models presented in this work are based on the Kirchhoff plate theory and assume the main source of polarization to be static bulk flexoelectricity. Following recent efforts on the converse flexoelectric effect in finite samples, the proposed models properly accounts for thermodynamically consistent, symmetric, direct and converse coupling terms, and it capture the size effect on the coupling coefficient.

Based on a modal analysis procedure, closed-form solutions of the electromechanical frequency response functions (voltage across the electrical load and coupled vibration response) are given for both monolayer and bimorph cases. Results of an extensive analysis are presented at different geometric scales (mm, μm, and nm thickness levels with a fixed aspect ratio) for non-piezoelectric Strontium Titanate (STO) and piezoelectric Barium Titanate (BTO) plates that are shunted to a resistive electrical load for quantifying the electrical power output and its feedback on the vibration response due to the converse effect.

The transverse mode flexoelectric coupling coefficient, k_f, and the flexoelectric-piezoelectric coupling coefficient, k_p, (as a direct and compact measure of energy conversion) are analytically extracted from the short- and open-circuit natural frequencies. The flexoelectric energy conversion and harvesting become significant only at nm thickness levels for typical flexoelectric coefficients obtained from atomistic simulations (with order of magnitude 10^{-9} C/m). For instance, the negligible flexoelectric coupling of an STO monolayer plate at the mm thickness level increases by 6 orders of magnitude (from $k_f \approx 3.6 \times 10^{-7}$ to $k_f \approx 0.34$) when the thickness is reduced to nm-level. The flexoelectric-piezoelectric coupling increases from the bulk piezoelectric value of $k_p \approx 0.0675$ at the mm-scale to $k_p \approx 0.376$ at the nm-scale owing to flexoelectric contribution. Overall, since the coupling coefficient is thickness dependent, the energy conversion dramatically increases in submicron thickness levels due to the flexoelectric effect. The proposed models can be used for parameter identification as well as performance quantification and optimization in combined flexoelectric and piezoelectric energy harvesting and actuation.

CHAPTER VII

DYNAMICS OF LONGITUDINAL (AXIAL) MODE FLEXOELECTRIC STRUCTURES

7.1 Introduction

In this chapter we establish and analyze the governing electroelastodynamic flexoelectric equations for a truncated cone (i.e. varying cross-sectional area) for energy harvesting and actuation. The coupled governing equations are obtained using the Rayleigh (accounting for lateral inertia effects) and Bishop (accounting for lateral inertia and shear effects) models. This approach results in a coupling between the lateral (transverse) and longitudinal (axial) flexoelectric modes. Simulation case studies are performed for axial vibrations of Strontium Titanate truncated cones (with small cone angles) for energy harvesting under mechanical base excitation and dynamic actuation under electrical excitation (fixed base). The effect of flexoelectric polarization is explored for various geometric scales to observe and quantify the size dependence of the axial flexoelectric effects.

7.2 Electromechanical Lagrange's equations based on extended Hamilton's principle

We consider the problem of a dielectric cylindrical truncated cone under mechanical base excitation and voltage actuation for linear axial (longitudinal) vibrations (Fig. 37) by accounting for flexoelectricity. In Fig. 37a, the surface electrodes on the circular faces of the cone are shunted to a resistive electrical load to quantify the electrical power output in the harvester model. The dynamic actuation problem for a fixed base is depicted in Fig. 37b. In the following, the energy harvesting problem is first formulated and then rearranged for the dynamic voltage actuation problem.

For a dielectric truncated cone with slight angle and thin electrodes on the faces perpendicular to x_3 (Fig. 37), the lateral components of the electric field are negligible. Therefore,

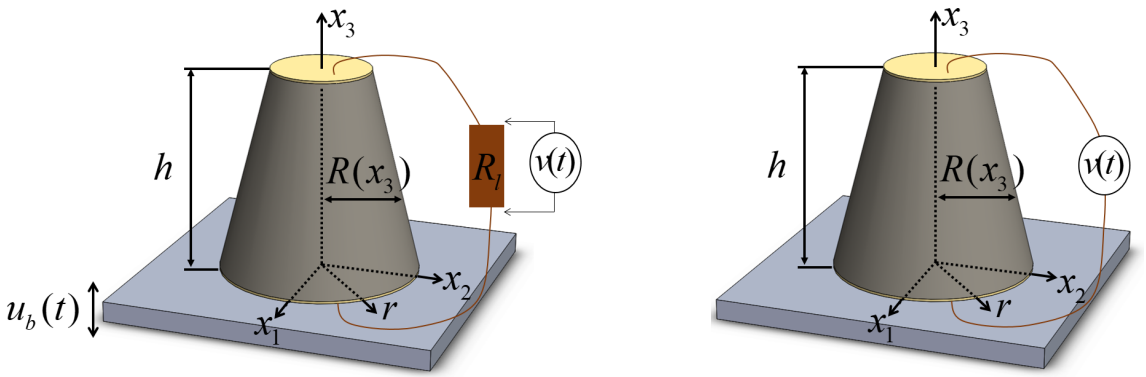

Figure 37: Truncated cone configuration (varying radius $R(x_3)$) for exploiting longitudinal (or thickness) flexoelectric mode (with cylindrical coordinates) for **(a)** energy harvesting from base excitation and **(b)** dynamic voltage actuation (fixed base)

the stress field is given by

$$T_{11} = c_{1111}S_{11} + c_{1122}S_{22} + c_{1133}S_{33} + f_{1133}\frac{\partial P_3}{\partial x_3} \tag{187}$$

$$T_{22} = c_{1122}S_{11} + c_{1111}S_{22} + c_{1133}S_{33} + f_{1133}\frac{\partial P_3}{\partial x_3} \tag{188}$$

$$T_{33} = c_{1133}S_{11} + c_{1133}S_{22} + c_{3333}S_{33} + f_{3333}\frac{\partial P_3}{\partial x_3} \tag{189}$$

$$T_{23} = c_{2323}S_{23} \tag{190}$$

$$T_{13} = c_{2323}S_{13} \tag{191}$$

$$T_{12} = \frac{c_{1111} - c_{1122}}{2}S_{12} \tag{192}$$

where c_{1111}, c_{1122}, c_{1133}, c_{3333}, c_{2323} are elastic constants, f_{1133} and f_{3333} are "flexocoupling coefficients" [82], and P_3 is the polarization in the thickness direction.

The electric displacement is given by

$$D_3 = \varepsilon_{33}E_3 + \mu_{1133}\left(\frac{\partial S_{11}}{\partial x_3} + \frac{\partial S_{22}}{\partial x_3}\right) + \mu_{3333}\frac{\partial S_{33}}{\partial x_3} \tag{193}$$

where E_3 is the electric field in the thickness direction, μ_{1133} and μ_{3333} are flexoelectric coefficients, and ε_{33} is the dielectric permittivity.

In cylindrical coordinates (r, ϑ, x_3), the engineering strain is related to the displacement field by [71, 68]

$$S_{11} = \frac{\partial u_r}{\partial r} \tag{194}$$

$$S_{22} = \frac{1}{r}\left(\frac{\partial u_\vartheta}{\partial \vartheta} + u_r\right) \tag{195}$$

$$S_{33} = \frac{\partial u_z}{\partial x_3} \tag{196}$$

$$S_{23} = \frac{1}{r}\frac{\partial u_z}{\partial \vartheta} + \frac{\partial u_\vartheta}{\partial x_3} \tag{197}$$

$$S_{13} = \frac{\partial u_r}{\partial x_3} + \frac{\partial u_z}{\partial r} \tag{198}$$

$$S_{12} = \frac{1}{r}\left(\frac{\partial u_r}{\partial \vartheta} - u_\vartheta\right) + \frac{\partial u_\vartheta}{\partial r} \tag{199}$$

where u_r, u_ϑ, and u_z are the displacements in the r, ϑ, and x_3 directions, respectively.

In the absence of mechanical dissipative effects, the extended Hamilton's principle with the internal electrical energy is

$$\int_{t_1}^{t_2} (\delta T - \delta U + \delta W_{ie} + \delta W_{nc}) dt = 0 \tag{200}$$

where δT, δU, and δW_{ie} are the first variations of the total kinetic energy, the total potential energy, and the internal electrical energy while δW_{nc} is the virtual work of the non-conservative mechanical force and electrical charge components.

The strain, internal electrical, and kinetic energies are given by

$$U = \frac{1}{2}\int_V \left(T_{11}S_{11} + T_{22}S_{22} + T_{33}S_{33} + T_{23}S_{23} + T_{13}S_{13} + T_{12}S_{12}\right) dV \tag{201}$$

$$W_{ie} = \frac{1}{2}\int_V E_3 D_3 dV \tag{202}$$

$$T = \frac{1}{2}\int_V \rho \left[\left(\frac{\partial u_r}{\partial t}\right)^2 + \left(\frac{\partial u_\vartheta}{\partial t}\right)^2 + \left(\frac{\partial u_z}{\partial t}\right)^2\right] dV \tag{203}$$

7.3 Rayleigh theory for axial vibrations

The Rayleigh method for axial vibrations of an axisymmetric thin rod assumes a displacement field given by [71]

$$\begin{aligned} u_z &= u(x_3, t) \\ u_r &= -\nu r \frac{\partial u_z}{\partial x_3} \\ u_\vartheta &= 0 \end{aligned} \tag{204}$$

where $\nu = \frac{c_{1133}}{c_{1111}+c_{1122}}$ is Poisson's ratio.

Substituting the displacement field given by Eq. 204 into the lateral and shear strains given by Eqs. 194 - 195 and 197 - 199 yields

$$S_{11} = S_{22} = -\nu \frac{\partial u_z}{\partial x_3} \tag{205}$$

$$S_{23} = S_{12} = 0 \tag{206}$$

$$S_{13} = -\nu r \frac{\partial^2 u_z}{\partial {x_3}^2} \tag{207}$$

This yields the lateral strains to be equal, $S_{11} = S_{22}$. The electric displacement given by Eq. 193 can be simplified to yield

$$D_3 = \varepsilon_{33} E_3 + 2\mu_{1133} \frac{\partial S_{11}}{\partial x_3} + \mu_{3333} \frac{\partial S_{33}}{\partial x_3} \tag{208}$$

The Rayleigh method accounts for the inertia of the lateral motions but neglects the shear stiffness contribution to the strain energy (i.e. assumes the shear stresses, T_{23}, T_{13}, and T_{12} are zero) [71, 68].

Substituting the nonzero stresses and strains into the strain, internal electrical, and kinetic energy expressions given by Eqs. 201 - 203 and simplifying yields

$$\begin{aligned} U = \frac{1}{2} \int_V \Bigg[& \left(2\nu^2 \left(c_{1111} + c_{1122}\right) - 4c_{1133}\nu + c_{3333}\right) \left(\frac{\partial u_z}{\partial x_3}\right)^2 + \\ & + \left(f_{3333} - 2\nu f_{1133}\right) \frac{\partial P_3}{\partial x_3} \frac{\partial u_z}{\partial x_3} \Bigg] dV \end{aligned} \tag{209}$$

$$W_{ie} = \frac{1}{2} \int_V \left[\varepsilon_{33} {E_3}^2 + \left(\mu_{3333} - 2\nu\mu_{1133}\right) \frac{\partial^2 u_z}{\partial {x_3}^2} E_3 \right] dV \tag{210}$$

$$T = \frac{1}{2} \int_V \rho \left[\left(\nu r \frac{\partial^2 u_z}{\partial t \partial x_3} \right)^2 + \left(\frac{\partial u_z}{\partial t} \right)^2 \right] dV \tag{211}$$

Evaluating the integrals of the energy equations yields

$$\begin{aligned} U = \frac{1}{2} \int_0^h A(x_3) \Bigg[& \left(2\nu^2 \left(c_{1111} + c_{1122}\right) - 4c_{1133}\nu + c_{3333}\right) \left(\frac{\partial u_z}{\partial x_3}\right)^2 + \\ & + \left(f_{3333} - 2\nu f_{1133}\right) \frac{\partial P_3}{\partial x_3} \frac{\partial u_z}{\partial x_3} \Bigg] dx_3 \end{aligned} \tag{212}$$

$$W_{ie} = \frac{1}{2}\int_0^h A(x_3)\left[\varepsilon_{33}{E_3}^2 + (\mu_{3333} - 2\nu\mu_{1133})\frac{\partial^2 u_z}{\partial z^2}E_3\right]dx_3 \tag{213}$$

$$T = \frac{1}{2}\int_0^h \rho\left[\nu^2 J(x_3)\left(\frac{\partial^2 u_z}{\partial t \partial x_3}\right)^2 + A(x_3)\left(\frac{\partial u_z}{\partial t}\right)^2\right]dx_3 \tag{214}$$

where $J(x_3)$ is the polar moment of inertia given by

$$J(x_3) = \frac{\pi}{2}R^4(x_3) \tag{215}$$

and $A(x_3)$ is the cross-sectional area given by

$$A(x_3) = \pi R^2(x_3) \tag{216}$$

As done in the previous chapters, the polarization gradient $\left(\frac{\partial P_3}{\partial x_3}\right)$ in Eq. 212 is evaluated using integration by parts to identify the role in the strain energy by following Tagantsev and Yurkov [77], for a finite sample in which the polarization in the thickness direction varies continuously from its bulk value to zero at the top and bottom surfaces of the truncated cone at $x_3 = h$ and $x_3 = 0$.

The resulting strain energy is

$$\begin{aligned} U = \frac{1}{2}\int_0^h A(x_3)\Bigg[&\left(2\nu^2\left(c_{1111} + c_{1122}\right) - 4c_{1133}\nu + c_{3333}\right)\left(\frac{\partial u_z}{\partial x_3}\right)^2 + \\ &- \left(\mu_{3333} - 2\nu\mu_{1133}\right)E_3\frac{\partial^2 u_z}{\partial {x_3}^2}\Bigg]dx_3 \end{aligned} \tag{217}$$

Here, for a small cone angle, the electric field can be approximated as $E_3 = -v/h$. The strain and internal electrical energies become

$$\begin{aligned} U = \frac{1}{2}\int_0^h A(x_3)\Bigg[&\left(2\nu^2\left(c_{1111} + c_{1122}\right) - 4c_{1133}\nu + c_{3333}\right)\left(\frac{\partial u_z}{\partial x_3}\right)^2 + \\ &+ \left(\mu_{3333} - 2\nu\mu_{1133}\right)\frac{v}{h}\frac{\partial^2 u_z}{\partial {x_3}^2}\Bigg]dx_3 \end{aligned} \tag{218}$$

$$W_{ie} = \frac{1}{2}\int_0^h A(x_3)\left[\varepsilon_{33}\frac{v^2}{h^2} - \left(\mu_{3333} - 2\nu\mu_{1133}\right)\frac{\partial^2 u_z}{\partial {x_3}^2}\frac{v}{h}\right]dx_3 \tag{219}$$

Following the method of assumed modes for an electromechanical system [34], the components of the extended Hamilton's principle are discretized. The distributed parameter in

the mechanical domain is $u_z(x_3,t)$ while the electrical variable is $v(t)$. Let the vibration response be represented by the finite series expansion:

$$u_z(x_3,t) = \sum_{i=1}^{N} a_i(t)\beta_i(x_3) \tag{220}$$

where $\beta_i(x_3)$ is the kinematically admissible trial functions which satisfy the respective essential boundary conditions (at the fixed end), $a_i(t)$ is the unknown generalized coordinates, and N is the number of modes considered in the solution.

The electromechanical Lagrange's equations based on the extended Hamilton's principle given by Eq. 200 are

$$\frac{d}{dt}\left(\frac{\partial T}{\partial \dot{a}_i}\right) - \frac{\partial T}{\partial a_i} + \frac{\partial U}{\partial a_i} - \frac{\partial W_{ie}}{\partial a_i} = 0 \tag{221}$$

$$\frac{d}{dt}\left(\frac{\partial T}{\partial \dot{v}}\right) - \frac{\partial T}{\partial v} + \frac{\partial U}{\partial v} - \frac{\partial W_{ie}}{\partial v} = Q \tag{222}$$

where Q is the electric charge output of the flexoelectric truncated cone.

The discretized strain, internal electrical, and kinetic energies are

$$U = \frac{1}{2}\sum_{i=1}^{N}\sum_{j=1}^{N}\left[k_{ij}a_i a_j + \theta_i a_i v\right] \tag{223}$$

$$W_{ie} = \frac{1}{2}\sum_{i=1}^{N}\left[Cv^2 - \theta_i a_i v\right] \tag{224}$$

$$T = \frac{1}{2}\sum_{i=1}^{N}\sum_{j=1}^{N}\left[\left(I_{ij} + m_{ij}\right)\dot{a}_i\dot{a}_j\right] \tag{225}$$

where

$$k_{ij} = \left(2\nu^2\left(c_{1111}+c_{1122}\right) - 4c_{1133}\nu + c_{3333}\right)\int_0^h \left[A(x_3)\beta_i{}'(x_3)\beta_j{}'(x_3)\right]dx_3 \tag{226}$$

$$C = \frac{\varepsilon_{33}}{h^2}\int_0^h A(x_3)dx_3 \tag{227}$$

$$I_{ij} = \rho\nu^2\int_0^h \left[J(x_3)\beta_i{}'(x_3)\beta_j{}'(x_3)\right]dx_3 \tag{228}$$

$$m_{ij} = \rho\int_0^h \left[A(x_3)\beta_i(x_3)\beta_j(x_3)\right]dx_3 \tag{229}$$

$$\theta_i = \left(\mu_{3333} - 2\nu\mu_{1133}\right)\frac{1}{h}\int_0^h A(x_3)\beta_i{}''(x_3)dx_3 \tag{230}$$

7.3.1 Voltage and vibration response for energy harvesting

The first set of Lagrange's equations (for the generalized coordinate a_l) becomes

$$(\tilde{\mathbf{m}} + \mathbf{I})\,\ddot{\mathbf{a}} + \mathbf{d}\dot{\mathbf{a}} + \mathbf{k}\mathbf{a} + \boldsymbol{\theta} v = \mathbf{f} \tag{231}$$

where the mass, stiffness and inertial ($\tilde{\mathbf{m}}$, $\mathbf{k}$, and $\mathbf{I}$) are $N \times N$ matrices whose elements are given by Eqs. 229, 226, and 228, respectively. The $N \times 1$ vector of generalized coordinates is $\mathbf{a} = [a_1\ a_2\ \ldots\ a_N]^T$ and the $N \times 1$ vector of electromechanical coupling is $\boldsymbol{\theta} = [\theta_1\ \theta_2\ \ldots\ \theta_N]^T$ where the elements are given by Eq. 230. Equation 231 can be simplified to become

$$\mathbf{m}\ddot{\mathbf{a}} + \mathbf{d}\dot{\mathbf{a}} + \mathbf{k}\mathbf{a} + \boldsymbol{\theta} v = \mathbf{f} \tag{232}$$

where $\mathbf{m} = \tilde{\mathbf{m}} + \mathbf{I}$ and the damping matrix ($N \times N$) is $\mathbf{d} = \mu\mathbf{m} + \gamma\mathbf{k}$. Here μ and γ are the constants of mass and stiffness proportionality, respectively. The forcing vector $\mathbf{f}$ is an $N \times 1$ vector whose elements are given by

$$f_i = -\int_0^h \rho A(x_3)\beta_i(x_3)\frac{\partial^2 u_b(x_1,t)}{\partial t^2}dx_3 \tag{233}$$

The second Lagrange's equation is

$$C\dot{v} + \frac{v}{R_l} - (\boldsymbol{\theta})^T\dot{\mathbf{a}} = 0 \tag{234}$$

For harmonic forcing the generalized coordinates are also harmonic at the same frequency. Solving Eqs. 232 and 234, the steady state transverse vibration and voltage responses are

$$u_z(x_3,t) = \mathbf{B}(x_3)^T\boldsymbol{\Gamma}^{-1}\mathbf{F}e^{j\omega t} \tag{235}$$

$$v(t) = Ve^{i\omega t} = j\omega\left(j\omega C + \frac{1}{R_l}\right)^{-1}\left[(\boldsymbol{\theta})^T\boldsymbol{\Gamma}^{-1}\mathbf{F}\right] \tag{236}$$

where $\mathbf{B}(x_3)$ is the vectorial representations of the respectable admissible function sets $\beta_i(x_3)$ and $\boldsymbol{\Gamma} = \left(-\omega^2\mathbf{m} + j\omega\mathbf{d} + \mathbf{k}\right) + j\omega\left(j\omega C + \frac{1}{R_l}\right)^{-1}\boldsymbol{\theta}(\boldsymbol{\theta})^T$

7.3.2 Vibration response and current drawn for actuation

The governing equations in energy harvesting (Eqs. 232 and 234) can be modified to represent the actuation problem similarly such that there is no base excitation ($f_i = 0$) and the excitation is due to harmonic voltage input, yielding

$$u_z(x_3,t) = \mathbf{B}^T(x_3)\left(-\omega^2\boldsymbol{m} + j\omega\boldsymbol{d} + \boldsymbol{k}\right)^{-1}\boldsymbol{\theta}Ve^{j\omega t} \tag{237}$$

$$i(t) = j\omega\left[C + (\boldsymbol{\theta})^T\left(-\omega^2\boldsymbol{m} + j\omega\boldsymbol{d} + \boldsymbol{k}\right)^{-1}\boldsymbol{\theta}\right]Ve^{j\omega t} \tag{238}$$

7.4 Bishop theory for axial vibrations

The Bishop theory extends the Rayleigh theory to consider both the inertia of the lateral motions and the shear stiffness [68]. The stresses and strains are given by Eqs. 187-199 and Eqs. 205-207, respectively. Including the effects of the shear stiffness leads to an additional term in the strain energy equation that was not included in the Rayleigh theory (Eq. 218). Following the same procedure as the previous section, the resulting strain energy, when accounting for the shear stress, is

$$\begin{aligned} U = \frac{1}{2}\int_0^h \Bigg[A(x_3)\Bigg(&\left(2\nu^2\left(c_{1111}+c_{1122}\right) - 4c_{1133}\nu + c_{3333}\right)\left(\frac{\partial u_z}{\partial x_3}\right)^2 + \\ &- \left(\mu_{3333} - 2\nu\mu_{1133}\right)E_3\frac{\partial^2 u_z}{\partial {x_3}^2}\Bigg) + c_{2323}\nu^2 J(x_3)\left(\frac{\partial^2 u_z}{\partial {x_3}^2}\right)^2\Bigg] dx_3 \end{aligned} \tag{239}$$

where $J(x_3)$ is the polar moment of inertia given by Eq. 215.

Substituting $E_3 = -v/h$ and discretizing the strain energy by substituting Eq. 220 into Eq. 239 yields

$$U = \frac{1}{2}\sum_{i=1}^{N}\sum_{j=1}^{N}\left[\left(k_{ij} + g_{ij}\right)a_i a_j + \theta_i a_i v\right] \tag{240}$$

where

$$g_{ij} = c_{2323}\nu^2\int_0^h J(x_3)\left[{\beta_i}''(x_3){\beta_j}''(x_3)\right]dx_3 \tag{241}$$

The internal electrical and kinetic energies for the Bishop model are the same as those for the Rayleigh model given by Eqs. 224 and 225. As a result, the flexoelectric coupling term is unaffected by the including the effects of shear stiffness. However, the model is

expected to be more accurate in predicting the natural frequencies and overall mechanical behavior.

7.4.1 Voltage and vibration response for energy harvesting

The first set of Lagrange's equations (for the generalized coordinate a_l) becomes

$$(\tilde{\mathbf{m}} + \mathbf{I})\,\ddot{\mathbf{a}} + \mathbf{d}\dot{\mathbf{a}} + \left(\tilde{\mathbf{k}} + \mathbf{g}\right)\mathbf{a} + \boldsymbol{\theta} v = \mathbf{f} \tag{242}$$

where the mass, stiffness, inertial, and shear matrices ($\tilde{\mathbf{m}}$, $\tilde{\mathbf{k}}$, $\mathbf{I}$, and $\mathbf{g}$) are $N \times N$ whose elements are given by Eqs. 229, 226, 228, and 241, respectively. The $N \times 1$ vector of generalized coordinates is $\mathbf{a} = [a_1\ a_2\ .\ .\ .\ a_N]^T$ and the $N \times 1$ vector of electromechanical coupling is $\boldsymbol{\theta} = [\theta_1\ \theta_2\ .\ .\ .\ \theta_N]^T$ where the elements are given by Eq. 230. Equation 242 can be simplified to become

$$\mathbf{m}\ddot{\mathbf{a}} + \mathbf{d}\dot{\mathbf{a}} + \mathbf{k}\mathbf{a} + \boldsymbol{\theta} v = \mathbf{f} \tag{243}$$

where $\mathbf{m} = \tilde{\mathbf{m}} + \mathbf{I}$, $\mathbf{k} = \tilde{\mathbf{k}} + \mathbf{g}$, and the damping matrix is $\mathbf{d} = \mu\mathbf{m} + \gamma\mathbf{k}$. Here μ and γ are the constants of mass and stiffness proportionality, respectively.

The Bishop theory does not affect the electrical domain; therefore, the second Lagrange equation (solved from Eq. 222) is the same as for the Rayleigh theory given by Eq. 234.

For harmonic forcing the generalized coordinates are also harmonic at the same frequency. Solving Eqs. 243 and 234, the steady state transverse vibration and voltage responses are

$$u_z(x_3, t) = \mathbf{B}(x_3)^T \boldsymbol{\Gamma}^{-1} \mathbf{F} e^{j\omega t} \tag{244}$$

$$v(t) = V e^{i\omega t} = j\omega \left(j\omega C + \frac{1}{R_l}\right)^{-1} \left[(\boldsymbol{\theta})^T \boldsymbol{\Gamma}^{-1} \mathbf{F}\right] \tag{245}$$

where $\mathbf{B}(x_3)$ is the vectorial representations of the respectable admissible function sets $\beta_i(x_3)$ and $\boldsymbol{\Gamma} = \left(-\omega^2\mathbf{m} + j\omega\mathbf{d} + \mathbf{k}\right) + j\omega\left(j\omega C + \frac{1}{R_l}\right)^{-1} \boldsymbol{\theta}(\boldsymbol{\theta})^T$

7.4.2 Vibration response and current drawn for actuation

The governing equations in energy harvesting (Eqs. 243 and 234) can be modified to represent the actuation problem similarly such that there is no base excitation ($f_i = 0$) and

the excitation is due to harmonic voltage input, yielding

$$u_z(x_3,t) = \mathbf{B}^T(x_3)\big(-\omega^2\boldsymbol{m} + j\omega\boldsymbol{d} + \boldsymbol{k}\big)^{-1}\boldsymbol{\theta}Ve^{j\omega t} \tag{246}$$

$$i(t) = j\omega\left[C + (\boldsymbol{\theta})^T\big(-\omega^2\boldsymbol{m} + j\omega\boldsymbol{d} + \boldsymbol{k}\big)^{-1}\boldsymbol{\theta}\right]Ve^{j\omega t} \tag{247}$$

7.5 Case studies and results

In this section, simulations are performed to show the effect of thickness on the electromechanical coupling and frequency response behavior of flexoelectric truncated cones under axial vibrations for energy harvesting and actuation. Because the Rayleigh and Bishop models resulted in the same electromechanical coupling (Eq. 230), the simulations are performed using the Bishop equations. The Bishop truncated cone simulations for non-piezoelectric materials are for performed for Strontium Titantate (STO) using the using the elastic [9, 44] and dielectric [89, 3] properties of $c_{1111} = 318$ GPa, $c_{1122} = 102.4$ GPa, $c_{1133} = 100$ GPa, $c_{3333} = 317$ GPa, $c_{2323} = 123.8$ GPa, $\rho = 5116$ kg/m^3, and $\varepsilon_{33} = 2.66$ nF/m (for the room temperature relative permittivity [89, 88, 3], $\varepsilon_{33}/\varepsilon_0 = 300$), and using the atomistic flexoelectric coefficient values [60] of $\mu_{1133} = -3.75\times10^{-9}$ C/m and $\mu_{3333} = -0.264\times10^{-9}$ C/m. The admissible trial functions used for all simulations are $\beta_i(x_3) = 1 - \cos\left(\frac{(2i-1)\pi x_3}{2h}\right)$.

7.5.1 Electromechanical frequency response for energy harvesting

The electromechanical frequency response behavior of a truncated cone flexoelectric energy harvester under base excitation is simulated with a focus on the first axial mode ($r = 1$) for a range of electrical load resistance values. Three different geometric scales are explored ranging from mm-scale to nm-scale. For each case, the base radius/tip radius/height aspect ratio ($R(0)/R(h)/h$) was fixed at 1/0.875/4. The truncated cone is made of STO and has perfectly conductive surface electrodes on the faces that are perpendicular to the x_3 (longitudinal) axis. Damping is neglected (in all cases) to better visualize the change in the electromechanical coupling (i.e. short- and open-circuit resonances, or the resonance and antiresonance in the admittance). Three cases with thicknesses (h) of 4 mm, 4 μm, and 4 nm are analyzed while keeping the same aspect ratio. The mechanical excitation is harmonic base acceleration, $d^2u_b(t)/dt^2 = -\omega^2U_0e^{j\omega t}$. The results are presented as frequency response

magnitude maps normalized by the base acceleration quantified in terms of gravitational acceleration as in the previous chapters. To capture optimal load in power generation and respective trends with changing load, a range of electrical resistive load values spanning from short- to open-circuit conditions (100 Ω to 1 GΩ) are simulated for each case. The optimal load for peak power output can be determined for each case from the power output frequency response maps.

The power output (per base acceleration squared) is calculated from Eq. 245 using $\left|v(t)/-\omega^2 W_0 e^{j\omega t}\right|^2/R_l$ for each of the three geometric scales and the fixed aspect ratio discussed previously. The resulting graphs are shown in Fig. 38a. The optimal laod for peak power output can be determined for each case from the power output frequency response maps. The cases of both 4 mm and 4 μm-thick harvesters result in a peak power output around 100 kΩ. The 4 mm and 4 μm power output frequency response maps show the resonance frequency to be insensitive to the resistive load due to very low electromechanical coupling (Figs. 38a.i and 38a.ii). Consequently, a single optimal load is observed in the power map for the fundamental vibration mode. The dynamic definition of the modal electromechanical coupling coefficient can be obtained based on the difference between the open-circuit and short-circuit natural frequencies as defined by Eq. 43 in Chapter 2. The coupling coefficient for the 4 mm and 4 μm thick cones are $k \approx 0$ and $k \approx 3.97 \times 10^{-6}$, respectively. On the other hand, the 1 nm case study exhibits two peak values for two distinct optimal electrical loads, 1 kΩ and 10 MΩ, respectively at the short-circuit and open-circuit resonance frequencies, yielding the same power output (Fig. 38a.iii). As seen in previous chapters, the existence of two peaks in the power output is also the case in strongly coupled and lightly damped piezoelectric energy harvesters [37, 72, 73]. The electromechanical coupling for the 4 nm case is $k \approx 0.00397$. The same power output can be extracted at the short-circuit resonance frequency ($\sim \omega_1^{sc}$) for a lower electrical load resistance or at the open-circuit resonance frequency ($\sim \omega_1^{oc}$) for a larger electrical load resistance. As a result, the former optimal condition results in larger current and lower voltage, while the latter gives larger voltage and lower current.

Next, the axial structural response of the truncated cone by generating electricity from

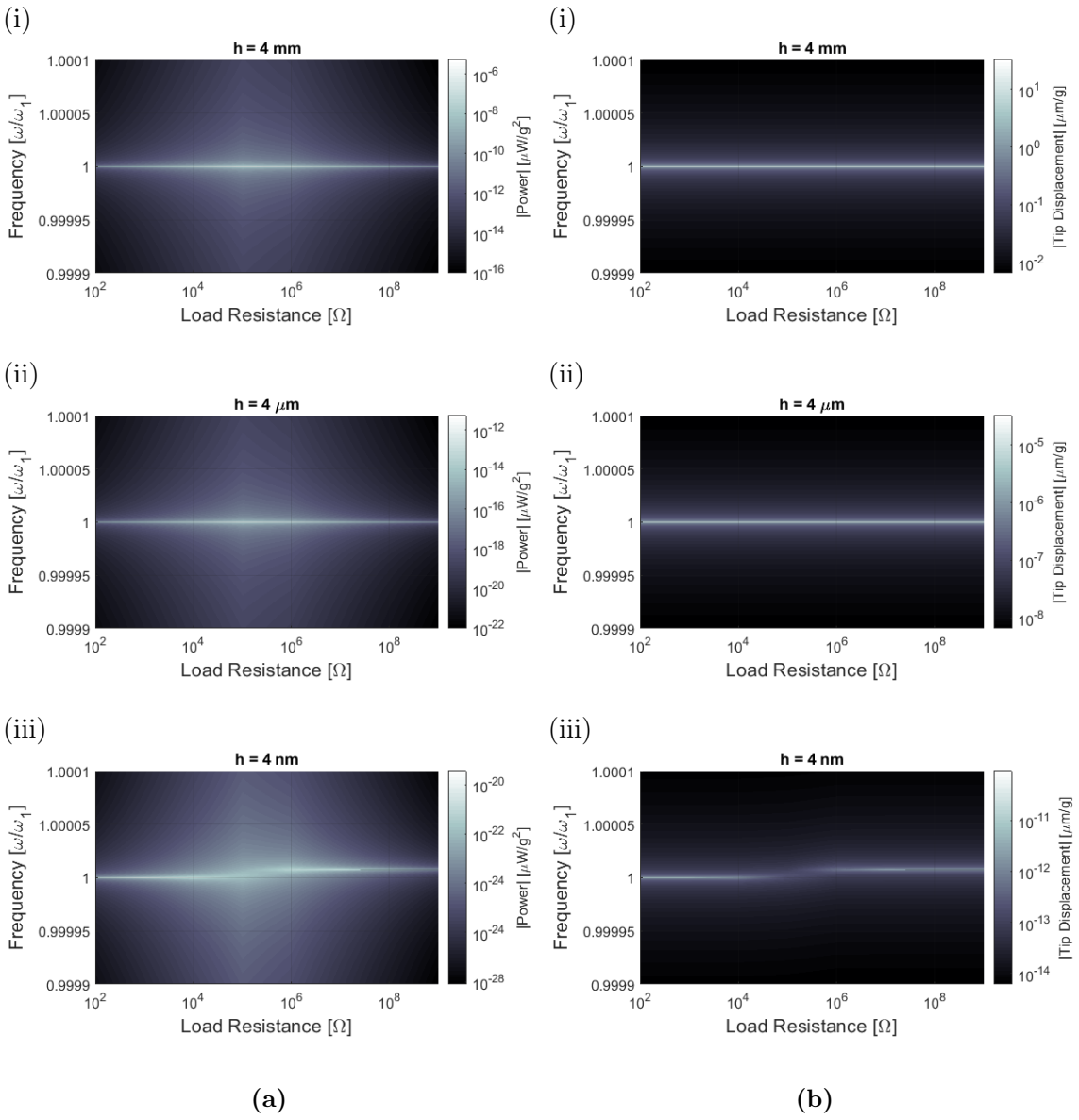

Figure 38: **(a)** Power output frequency response vs. load resistance maps (in magnitude form and per base acceleration squared) and **(b)** displacement frequency response vs. load resistance maps (in magnitude form and per base acceleration) for STO truncated cones with fixed aspect ratio of 1/0.875/4 ($R(0)/R(h)/h$) for three different geometric scales with the following thickness (h) values: (i) 4 mm, (ii) 4 μm, and (iii) 4 nm.

strain gradient fluctuations in response to base excitation is simulated for each geometric case. The motion of the truncated cone is evaluated at the tip ($x_3 = h$) using Eq. 244 for all three cases as shown in Fig. 38b. The axial vibration response of the truncated cone for the 4 mm and 4 μm thick case are insensitive to change in electrical load resistance as another manifestation of weak electromechanical coupling (Figs. 38b.i and 38b.ii). The small

electricity production, shown by the power output frequency response maps (Figs. 38a.i and 38a.ii) does not alter the vibration response of the truncated cone although the converse effect is taken account in the model. This confirms the flexoelectric effect is negligible at these geometric scales. The 4 nm case, however, due to increased electromechanical coupling, shows the vibration response to be sensitive to change in resistive load (Fig. 38b.iii). It should be noted that the overall electromechanical coupling even at the nanoscale is low (as compared to flexural mode flexoelectric effect). This is partially due to low variation in the cross-sectional area as required by the model assumptions to have a 1D problem. Another reason for lower electromechanical coupling is the low axial flexoelectric coefficient $\mu_{3333} = -0.264 \times 10^{-9}$ C/m, as compared to the transverse flexoelectric coefficient $\mu_{1133} = -3.75 \times 10^{-9}$ C/m (atomistic values from [60]). Discrepancies in the sign of the axial coefficient also affect the overall "effective" axial coupling given by $\mu_{3333} - 2\nu\mu_{1133}$, as well [60, 89]. The flexoelectric coupling in the cone can be enhanced with changing the cone angle such that it increases from $k \approx 0.00397$ to $k \approx 0.0351$ as the cone angle is changed from $\sim 1.8^\circ$ to $\sim 10^\circ$ as shown in Fig. 40. However, the problem would eventually deviate from the modeling assumptions in terms of the polarization and strain fields for very large cone angles.

7.5.2 Electromechanical frequency response in actuation

The same approximate analytical modeling framework is also employed to understand the electromechanical response of the centrosymmetric cone in the case of electrical excitation for the same set of system parameters. Of interest, is the displacement frequency response (structural response for unit actuation voltage input) from Eq. 246 and the admittance frequency response (amount of current drawn for unit actuation voltage input) calculated from Eq. 247. The displacement (measured at the tip, $x_3 = h$) and admittance frequency responses are shown in Figs. 39a and 39b, respectively. These frequency response functions show, once again, that significant electromechanical coupling only occurs at the nm-scale.

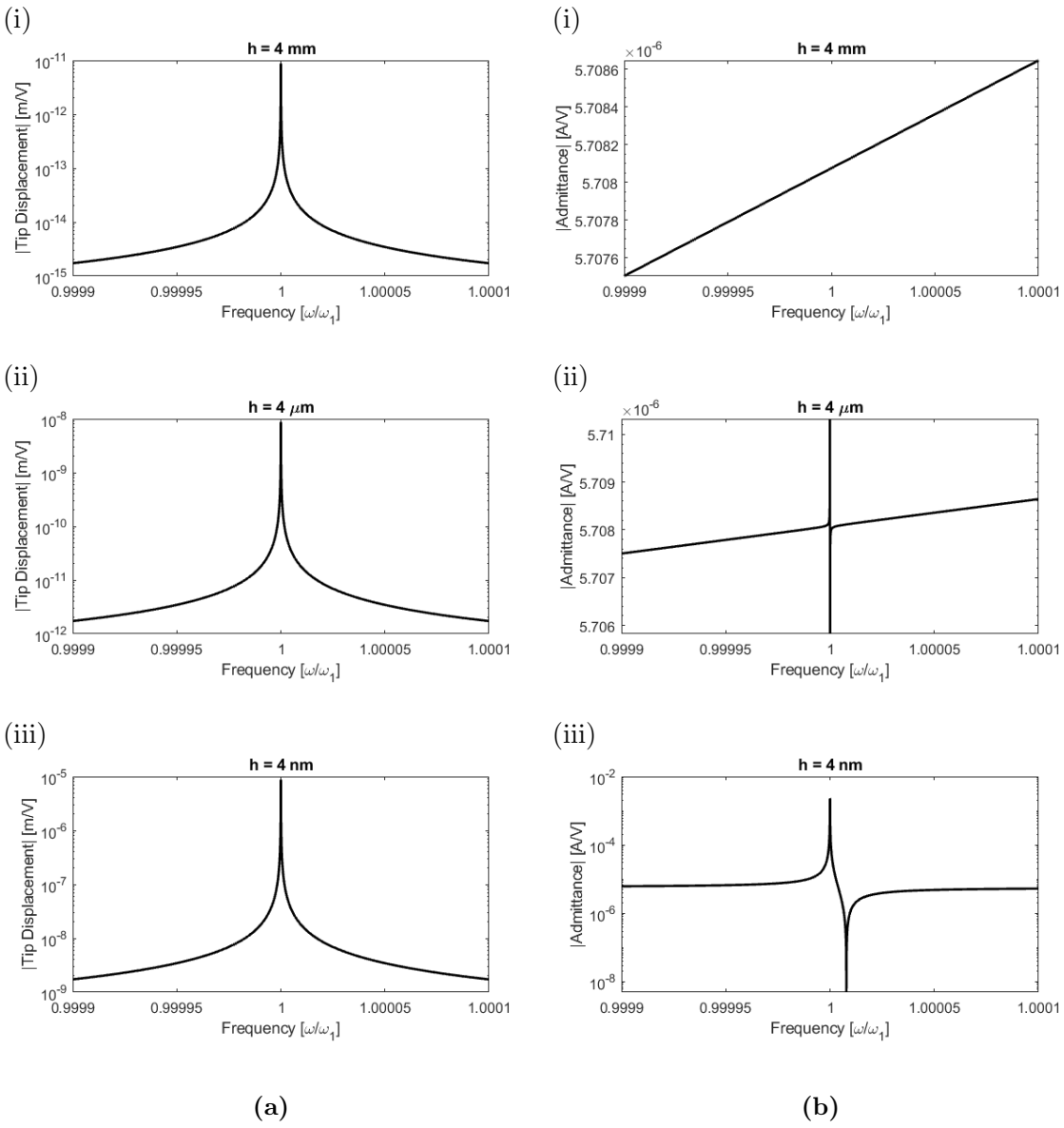

Figure 39: **(a)** Tip displacement and **(b)** admittance frequency response functions (in magnitude form) for actuation of STO truncated cones with fixed aspect ratio of 1/0.875/4 ($R(0)/R(h)/h$) for three different geometric scales with the following thickness (h) values: (i) 4 mm, (ii) 4 μm, and (iii) 4 nm.

7.6 Conclusions

An approximate analytical modeling framework for flexoelectric effects and its analysis are presented for truncated cones under axial vibrations. For arbitrary cross-sections, the exact solution is beyond reach, and therefore an energy formulation is used. This model developed for both Rayleigh (accounting for lateral inertia effects) and Bishop (accounting for lateral

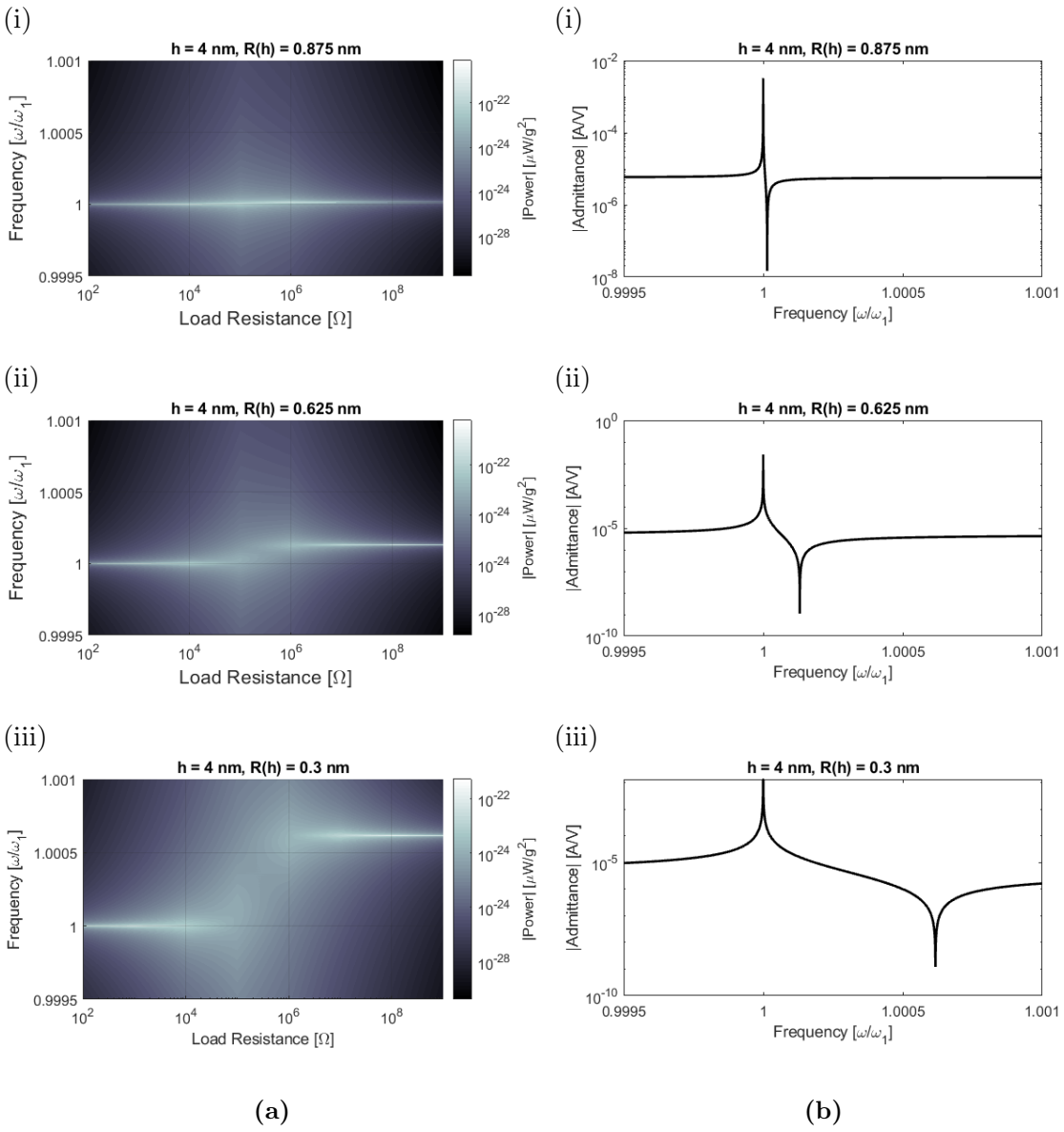

Figure 40: **(a)** Power output frequency response maps and **(b)** admittance frequency response functions (in magnitude form) of STO truncated cones for three different cone angles: (i) $\sim 1.8°$, (ii) $\sim 5°$, and (iii) $\sim 10°$.

inertia and shear effects) axial rod theories using the extended Hamilton's principle formulation properly accounts for thermodynamically consistent, symmetric, direct and converse coupling terms that include the flexoelectric axial coupling term, revealing symmetric coupling. The Rayleigh and Bishop models resulted in the same coupling expressions. The modeling framework was then used to understand the electromechanical response of the truncated cones in the case of electrical excitation. The axial electromechanical coupling

was found to be appreciable only at the nano-scale. The resulting axial electromechanical coupling at the nanoscale ($k \approx 0.00397$ for 4 nm thick STO cone) was significantly smaller than the transverse electromechanical coupling for nano-scale Euler-Bernoulli beams as shown in Chapter 2 ($k \approx 0.0.0869$ for 4 nm thick STO beam). Increased axial cross-section variation (i.e. cone angle) increases the coupling coefficient (in the same vein as in Chapter 4) as shown in Fig. 40. However, for very large cone angles, the problem would eventually deviate from the modeling assumptions in terms of the polarization and strain fields. As with the transverse flexoelectric coupling coefficients, the axial flexoelectric coefficients have discrepancies in the sign between values reported from experiments and atomistic results [60, 89] which could also effect the magnitude of the axial flexoelectric coupling.

CHAPTER VIII

CONCLUSIONS, CONTRIBUTIONS, AND FUTURE WORK

8.1 Summary and conclusions

This dissertation research is centered on modeling and analysis framework development to leverage flexoelectricity (strain gradient-induced polarization as a size-dependent effect) in next-generation ultralow-power MEMS/NEMS (micro/nano electromechanical systems) devices and concepts by converting ambient vibrations into electricity. Besides energy harvesting, the problem of flexoelectric actuation has also been considered as a natural product of the developed framework. As the main contribution, this work provided analytical and approximate analytical insights into size-dependent dynamics of dielectric cantilevers along with a coupling coefficient analysis (as a measure of energy conversion). Overall this research provides electroelastodynamic frameworks for flexoelectric and flexoelectric-piezoelectric structures for energy harvesting and actuation by accounting for thermodynamically consistent, symmetric, direct and converse coupling terms, and it captures the size effect on the coupling coefficient. Specifically, the problems of a monolayer centrosymmetric flexoelectric beam, flexoelectric-piezoelectric bimorph beam, flexoelectric monolayer plate, flexoelectric-piezoelectric bimorph plate, geometrically nonlinear flexoelectric monolayer beam, geometrically nonlinear flexoelectric-piezoelectric bimorph beam, and flexoelectric truncated cone have been explored. In all cases, the modeling and analysis frameworks have employed atomistic calculations of the respective flexoelectric constants in the absence of reliable experimental data in the literature.

8.2 Contributions and specific results

The following highlights from this dissertation summarize the major contributions:

- An analytical framework has been developed and analyzed for flexoelectric and flexoelectric-piezoelectric energy harvesting from bending vibrations, by accounting for

the presence of a finite electrical load across the surface electrodes as well as two-way coupling, yielding closed-form frequency response equations of the fully coupled system (Chapters 2 and 3).

- Beyond energy harvesting, the framework has also been modified to implement for resonant actuation, and the relevant electromechanical frequency response functions have been identified (vibration and electromechanical admittance) (Chapters 2 and 3).

- The flexoelectric energy conversion (coupling coefficient) and harvesting become significant only for nm thickness levels (< 100 nm, especially < 10 nm) for typical flexoelectric coefficients obtained from atomistic simulations (with order of magnitude 10^{-9} C/m) of STO (Chapter 2).

- Based on coupling coefficient (k) arguments, it is suggested that flexoelectric constants reported for experiments on certain mm-thick samples (by Ma and Cross [52, 53, 56, 54, 55, 57]) are unlikely to be bulk flexoelectricity and are not valid at other scales (Chapter 2).

- In the case of a piezoelectric material (e.g. BTO), flexoelectricity enhances the overall electromechanical coupling again for thickness levels below 100 nm such that the bulk piezoelectric constant of $k \approx 0.0652$ at the mm-scale increases to $k \approx 0.365$ at nm thickness level (Chapter 3).

- An approximate analytical modeling framework (using Hamilton's principle and Lagrange's equations via assumed-modes method) for flexoelectric and combined flexoelectric-piezoelectric effects is developed for varying cross-section thin beams under bending vibration (Chapter 4).

- Cross-section variation/geometry can be used to tailor the strain gradient distribution to increase electromechanical coupling; tapered beam geometry results in a coupling coefficient 10-20% more than that of the uniform case (Chapter 4).

- An approximate analytical modeling framework for geometrically nonlinear beam accounting for flexoelectric effects was developed and the jump phenomenon is captured (Chapter 5).

- The analytical framework for flexoelectric and flexoelectric-piezoelectric beams for energy harvesting and actuation was extend to 2-D configurations (Kirchhoff plates) and coupling was increased for a simply supported plate to $k \approx 0.34$ in nm thickness (Chapter 6).

- An approximate analytical modeling framework for axial flexoelectric effect (accounting for Poisson effect) via Rayleigh and Bishop theories is developed for truncated cones under longitudinal vibrations and size dependent electromechanical coupling was observed (Chapter 7).

- The flexoelectric coupling in the cone can be enhanced with changing the cone angle such that it increases from $k \approx 0.00397$ to $k \approx 0.0351$ as the cone angle is changed from $\sim 1.8^\circ$ to $\sim 10^\circ$ (Chapter 7).

8.3 Suggested future work

As pointed out in the introduction chapter, the existing literature of flexoelectricity has a major mismatch between the atomistic values of flexoelectric constants and experimentally identified ones. A particular reason for that is that the measured flexoelectric constants in literature are for thickness levels much larger than the scales for which flexoelectricity is expected to be pronounced. Therefore, it is usually assumed that most of the existing measured so-called flexoelectric constants contain a number of other components (e.g. surface piezoelectricity etc.) beyond bulk flexoelectricity [81]. As a consequence, this dissertation employed atomistic calculations of flexoelectric constants as reliable data. In the existing literature, there is an urgent need to obtain truly flexoelectric experimental data to quantify flexoelectric polarization and its scaling for submicron thickness.

A suggested future work for this research is to conduct experiments on nanowires and

thin films made from various materials including BTO (barium titanate) and STO (strontium titanate). Scanning electron microscope (SEM) images of a cluster of BTO nanowires and a single BTO nanowire are shown in Fig. 41a and Fig. 41b, respectively. The handling and testing of individual nanowires is already a challenge and controversies exist in measurement approaches as well.

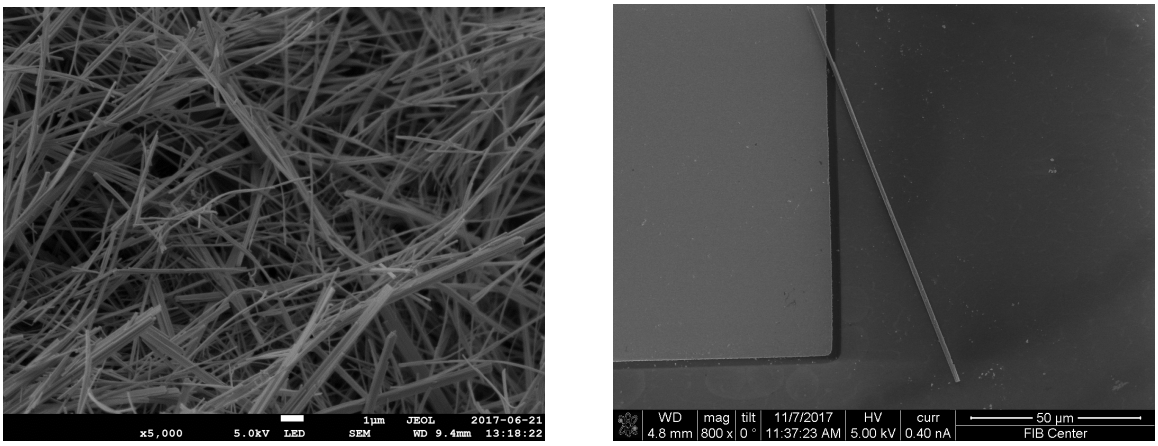

(a) **(b)**

Figure 41: Scanning electron microscope (SEM) images of **(a)** a cluster of BTO nanowires and **(b)** an individual BTO nanowire

Recently, Bhaskar et al. [10, 11] experimentally measured the flexoelectric coefficients using the converse effect (Fig. 42). The beams were made of thin film STO with a thickness of ~ 70 nm. The results showed transverse flexoelectric values on the order of nC/m which agrees with the modeling frameworks presented in this work. These results provide promise that accurate flexoelectric coefficients can be measured at the nano-scale using thin films. Therefore, experimental focus should be placed on thin films with thicknesses <100 nm for experimental measurement of the flexoelectric coefficients. Such experiments can make use of the analytical and approximate analytical models presented in this dissertation for parameter identification and performance quantification.

Metamaterials implementing nanoscale inhomogeneities in a non-piezoelectric elastic matrix have been theoretically studied to achieve piezoelectric-like properties from the flexoelectric effect [70]. It was shown that the shape and distribution of the nanoinclusions must be noncentrosymmetric to avoid the cancellation of the polarization locally induced

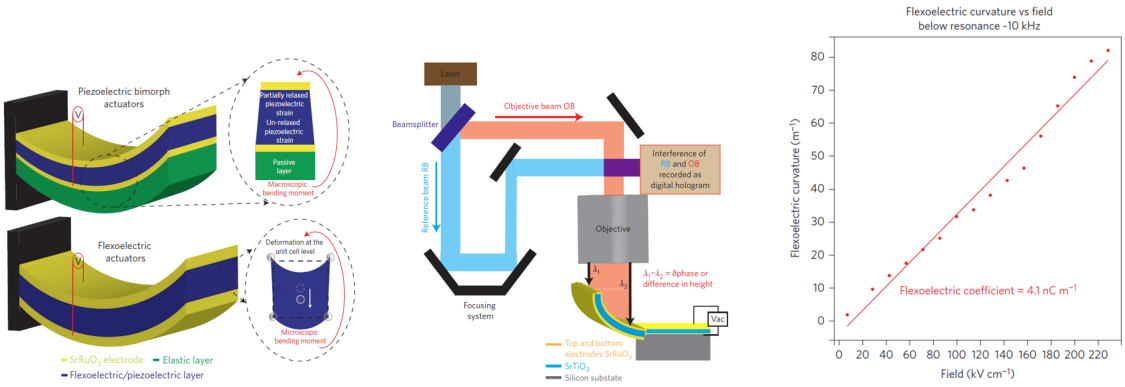

(a) **(b)** **(c)**

Figure 42: Experimental schematics and results from Bhaskar et al. [11]: **(a)** schematic of piezoelectric and flexoelectric nanoscale actuators, **(b)** schematic of experimental setup, and **(c)** experimental flexoelectric coefficient measurement of STO monolayer beam (Refer to [11] for more information)

by the strain gradient. Another a suggested future work is to extend the current modeling framework to study the effects of nanoinclusions on the flexoelectric coupling of dynamic nanoscale devices. This can be realized by modeling the nanoinclusions in the centrosymmetric material as a composite material and applying the current modeling framework for design, analysis, and performance quantification purposes.

REFERENCES

[1] "Standards Committee of the IEEE Ultrasonics, Ferroelectrics, and Frequency Control Society, IEEE Standard on Piezoelectricity," *ANSI/IEEE Std 176-1987*, pp. 1–66, 1984.

[2] Abdollahi, A. and Arias, I., "Constructive and destructive interplay between piezoelectricity and flexoelectricity in flexural sensors and actuators," *Journal of Applied Mechanics*, vol. 82, no. 12, p. 121003, 2015.

[3] Abe, K. and Komatsu, S., "Epitaxial growth of SrTiO3 films on Pt electrodes and their electrical properties," *Japanese Journal of Applied Physics*, vol. 31, no. 9S, p. 2985, 1992.

[4] Allen, J. J. and Smits, A. J., "Energy harvesting eel," *Journal of Fluids and Structures*, vol. 15, no. 3-4, pp. 629–640, 2001.

[5] Aridogan, U., Basdogan, I., and Erturk, A., "Multiple patchbased broadband piezoelectric energy harvesting on plate-based structures," *Journal of Intelligent Material Systems and Structures*, vol. 25, no. 14, pp. 1664–1680, 2014.

[6] Arrieta, A., Hagedorn, P., Erturk, A., and Inman, D., "A piezoelectric bistable plate for nonlinear broadband energy harvesting," *Applied Physics Letters*, vol. 97, no. 10, p. 104102, 2010.

[7] Barati, M. R., "On non-linear vibrations of flexoelectric nanobeams," *International Journal of Engineering Science*, vol. 121, pp. 143–153, 2017.

[8] Bechmann, R., "Elastic, piezoelectric, and dielectric constants of polarized barium titanate ceramics and some applications of the piezoelectric equations," *The Journal of the Acoustical Society of America*, vol. 28, no. 3, pp. 347–350, 1956.

[9] Bell, R. O. and Rupprecht, G., "Elastic constants of strontium titanate," *Physical Review*, vol. 129, no. 1, p. 90, 1963.

[10] Bhaskar, U. K., Banerjee, N., Abdollahi, A., Solanas, E., Rijnders, G., and Catalan, G., "Flexoelectric MEMS: towards an electromechanical strain diode," *Nanoscale*, vol. 8, no. 3, pp. 1293–1298, 2016.

[11] Bhaskar, U. K., Banerjee, N., Abdollahi, A., Wang, Z., Schlom, D. G., Rijnders, G., and Catalan, G., "A flexoelectric microelectromechanical system on silicon," *Nature Nanotechnology*, vol. 11, no. 3, pp. 263–266, 2016.

[12] Bishop, R. E. D., "Longitudinal waves in beams," *The Aeronautical Quarterly*, vol. 3, no. 4, pp. 280–293, 1952.

[13] Buka, A. and ber, N., *Flexoelectricity in Liquid Crystals: Theory, Experiments and Applications*. World Scientific, 2012.

[14] Bursian, E. V. and Zaikovskii, O. I., "Changes in the curvature of a ferroelectric film due to polarization," *Soviet Physics Solid State, USSR*, vol. 10, no. 5, pp. 1121–1124, 1968.

[15] Carrara, M., Cacan, M. R., Toussaint, J., Leamy, M. J., Ruzzene, M., and Erturk, A., "Metamaterial-inspired structures and concepts for elastoacoustic wave energy harvesting," *Smart Materials and Structures*, vol. 22, no. 6, p. 065004, 2013.

[16] Chandratre, S. and Sharma, P., "Coaxing graphene to be piezoelectric," *Applied Physics Letters*, vol. 100, no. 2, p. 023114, 2012.

[17] Choi, W., Jeon, Y., Jeong, J.-H., Sood, R., and Kim, S.-G., "Energy harvesting MEMS device based on thin film piezoelectric cantilevers," *Journal of Electroceramics*, vol. 17, no. 2-4, pp. 543–548, 2006.

[18] Chu, B., Zhu, W., Li, N., and Cross, L. E., "Flexure mode flexoelectric piezoelectric composites," *Journal of Applied Physics*, vol. 106, no. 10, p. 104109, 2009.

[19] Cook-Chennault, K. A., Thambi, N., and Sastry, A. M., "Powering MEMS portable devices-a review of non-regenerative and regenerative power supply systems with special emphasis on piezoelectric energy harvesting systems," *Smart Materials and Structures*, vol. 17, no. 4, p. 043001, 2008.

[20] Cross, L. E., "Flexoelectric effects: Charge separation in insulating solids subjected to elastic strain gradients," *Journal of Materials Science*, vol. 41, no. 1, pp. 53–63, 2006.

[21] Cui, X.-B., Huang, C.-P., and Hu, J.-H., "Sound energy harvesting using an acoustic grating," *Journal of Applied Physics*, vol. 117, no. 10, p. 104502, 2015.

[22] Cunefare, K. A., Skow, E. A., Erturk, A., Savor, J., Verma, N., and Cacan, M. R., "Energy harvesting from hydraulic pressure fluctuations," *Smart Materials and Structures*, vol. 22, no. 2, p. 025036, 2013.

[23] Dai, H., Yan, Z., and Wang, L., "Nonlinear analysis of flexoelectric energy harvesters under force excitations," *International Journal of Mechanics and Materials in Design*, pp. 1–15, 2019.

[24] Daqaq, M. F., Masana, R., Erturk, A., and Quinn, D. D., "On the role of nonlinearities in vibratory energy harvesting: a critical review and discussion," *Applied Mechanics Reviews*, vol. 66, no. 4, p. 040801, 2014.

[25] De Marqui Jr, C. and Erturk, A., "Electroaeroelastic analysis of airfoil-based wind energy harvesting using piezoelectric transduction and electromagnetic induction," *Journal of Intelligent Material Systems and Structures*, vol. 24, no. 7, pp. 846–854, 2013.

[26] Deng, Q., "Size-dependent flexoelectric response of a truncated cone and the consequent ramifications for the experimental measurement of flexoelectric properties," *Journal of Applied Mechanics*, vol. 84, no. 10, p. 101007, 2017.

[27] Deng, Q., Kammoun, M., Erturk, A., and Sharma, P., "Nanoscale flexoelectric energy harvesting," *International Journal of Solids and Structures*, vol. 51, no. 18, pp. 3218–3225, 2014.

[28] Deng, Q., Liu, L., and Sharma, P., "Flexoelectricity in soft materials and biological membranes," *Journal of the Mechanics and Physics of Solids*, vol. 62, pp. 209–227, 2014.

[29] Dent, A., Bowen, C., Stevens, R., Cain, M., and Stewart, M., "Effective elastic properties for unpoled barium titanate," *Journal of the European Ceramic Society*, vol. 27, no. 13-15, pp. 3739–3743, 2007.

[30] Elvin, N. and Erturk, A., *Advances in energy harvesting methods*. Springer Science & Business Media, 2013.

[31] Eom, C.-B. and Trolier-McKinstry, S., "Thin-film piezoelectric mems," *Mrs Bulletin*, vol. 37, no. 11, pp. 1007–1017, 2012.

[32] Erturk, A. and Delporte, G., "Underwater thrust and power generation using flexible piezoelectric composites: an experimental investigation toward self-powered swimmer-sensor platforms," *Smart Materials and Structures*, vol. 20, no. 12, 2011.

[33] Erturk, A., Vieira, W. G. R., De Marqui, C., and Inman, D. J., "On the energy harvesting potential of piezoaeroelastic systems," *Applied Physics Letters*, vol. 96, no. 18, 2010.

[34] Erturk, A., "Assumed-modes modeling of piezoelectric energy harvesters: Euler–Bernoulli, Rayleigh, and Timoshenko models with axial deformations," *Computers & Structures*, vol. 106, pp. 214–227, 2012.

[35] Erturk, A., Hoffmann, J., and Inman, D. J., "A piezomagnetoelastic structure for broadband vibration energy harvesting," *Applied Physics Letters*, vol. 94, no. 25, p. 254102, 2009.

[36] Erturk, A. and Inman, D. J., "A distributed parameter electromechanical model for cantilevered piezoelectric energy harvesters," *ASME Journal of Vibration and Acoustics*, vol. 130, no. 4, p. 041002, 2008.

[37] Erturk, A. and Inman, D. J., *Piezoelectric Energy Harvesting*. Chichester, U.K.: Wiley, 2011.

[38] Fu, J. Y., Zhu, W., Li, N., and Cross, L. E., "Experimental studies of the converse flexoelectric effect induced by inhomogeneous electric field in a barium strontium titanate composition," *Journal of Applied Physics*, vol. 100, no. 2, p. 024112, 2006.

[39] Fukada, E., "History and recent progress in piezoelectric polymers," *Ultrasonics, Ferroelectrics and Frequency Control, IEEE Transactions on*, vol. 47, no. 6, pp. 1277–1290, 2000.

[40] Harris, P., "Mechanism for the shock polarization of dielectrics," *Journal of Applied Physics*, vol. 36, no. 3, pp. 739–741, 1965.

[41] Hu, T., Deng, Q., Liang, X., and Shen, S., "Measuring the flexoelectric coefficient of bulk barium titanate from a shock wave experiment," *Journal of Applied Physics*, vol. 122, no. 5, p. 055106, 2017.

[42] Huang, W., Kim, K., Zhang, S., Yuan, F., and Jiang, X., "Scaling effect of flexoelectric (Ba, Sr) TiO3 microcantilevers," *physica status solidi (RRL)-Rapid Research Letters*, vol. 5, no. 9, pp. 350–352, 2011.

[43] Indenbom, V. L., Loginov, E. B., and Osipov, M. A., "Flexoelectric effect and crystal-structure," *Kristallografiya*, vol. 26, no. 6, pp. 1157–1162, 1981.

[44] Kityk, A. V., Schranz, W., Sondergeld, P., Havlik, D., Salje, E. K. H., and Scott, J. F., "Low-frequency superelasticity and nonlinear elastic behavior of SrTiO3 crystals," *Physical Review B*, vol. 61, no. 2, p. 946, 2000.

[45] Kogan, S. M., "Piezoelectric effect during inhomogeneous deformation and acoustic scattering of carriers in crystals," *Soviet Physics-Solid State*, vol. 5, no. 10, pp. 2069–2070, 1964.

[46] Leadenham, S. and Erturk, A., "M-shaped asymmetric nonlinear oscillator for broadband vibration energy harvesting: Harmonic balance analysis and experimental validation," *Journal of Sound and Vibration*, vol. 333, no. 23, pp. 6209–6223, 2014.

[47] Leadenham, S. and Erturk, A., "Nonlinear m-shaped broadband piezoelectric energy harvester for very low base accelerations: primary and secondary resonances," *Smart Materials and Structures*, vol. 24, no. 5, p. 055021, 2015.

[48] Leadenham, S. and Erturk, A., "Unified nonlinear electroelastic dynamics of a bimorph piezoelectric cantilever for energy harvesting, sensing, and actuation," *Nonlinear Dynamics*, vol. 79, no. 3, pp. 1727–1743, 2015.

[49] Lesieutre, G. A. and Davis, C. L., "Can a coupling coefficient of a piezoelectric device be higher than those of its active material?," in *Smart Structures and Materials' 97*, pp. 281–292, International Society for Optics and Photonics.

[50] Lesieutre, G. A., Ottman, G. K., and Hofmann, H. F., "Damping as a result of piezoelectric energy harvesting," *Journal of Sound and Vibration*, vol. 269, no. 3, pp. 991–1001, 2004.

[51] Liu, J. Q., Fang, H. B., Xu, Z. Y., Mao, X. H., Shen, X. C., Chen, D., Liao, H., and Cai, B. C., "A MEMS-based piezoelectric power generator array for vibration energy harvesting," *Microelectronics Journal*, vol. 39, no. 5, pp. 802–806, 2008.

[52] Ma, W. and Cross, L. E., "Large flexoelectric polarization in ceramic lead magnesium niobate," *Applied Physics Letters*, vol. 79, no. 26, pp. 4420–4422, 2001.

[53] Ma, W. H. and Cross, L. E., "Observation of the flexoelectric effect in relaxor Pb(Mg1/3Nb2/3)O-3 ceramics," *Applied Physics Letters*, vol. 78, no. 19, pp. 2920–2921, 2001.

[54] Ma, W. H. and Cross, L. E., "Strain-gradient-induced electric polarization in lead zirconate titanate ceramics," *Applied Physics Letters*, vol. 82, no. 19, pp. 3293–3295, 2003.

[55] Ma, W. H. and Cross, L. E., "Flexoelectric effect in ceramic lead zirconate titanate," *Applied Physics Letters*, vol. 86, no. 7, 2005.

[56] Ma, W. and Cross, L. E., "Flexoelectric polarization of barium strontium titanate in the paraelectric state," *Applied Physics Letters*, vol. 81, pp. 3440–3442, 2002.

[57] Ma, W. and Cross, L. E., "Flexoelectricity of barium titanate," *Applied Physics Letters*, vol. 88, no. 23, p. 2902, 2006.

[58] Maeder, M. D., Damjanovic, D., and Setter, N., "Lead free piezoelectric materials," *Journal of Electroceramics*, vol. 13, no. 1-3, pp. 385–392, 2004.

[59] Majdoub, M. S., Sharma, P., and Cagin, T., "Enhanced size-dependent piezoelectricity and elasticity in nanostructures due to the flexoelectric effect," *Physical Review B*, vol. 77, no. 12, p. 125424, 2008.

[60] Maranganti, R. and Sharma, P., "Atomistic determination of flexoelectric properties of crystalline dielectrics," *Physical Review B*, vol. 80, no. 5, p. 054109, 2009.

[61] Mashkevich, V. S. and Tolpygo, K. B., "Electrical, optical and elastic properties of diamond type crystals," *Sov. Phys. JETP*, vol. 5, no. 3, pp. 435–439, 1957.

[62] Mindlin, R. D., "Polarization gradient in elastic dielectrics," *International Journal of Solids and Structures*, vol. 4, no. 6, pp. 637–642, 1968.

[63] Moro, L. and Benasciutti, D., "Harvested power and sensitivity analysis of vibrating shoe-mounted piezoelectric cantilevers," *Smart Materials & Structures*, vol. 19, no. 11, 2010.

[64] Nayfeh, A. H. and Mook, D. T., *Nonlinear Oscillations*. Wiley, 2008.

[65] Nguyen, T. D., Mao, S., Yeh, Y., Purohit, P. K., and McAlpine, M. C., "Nanoscale flexoelectricity," *Advanced Materials*, vol. 25, no. 7, pp. 946–974, 2013.

[66] Petrov, A. G., "Flexoelectricity of model and living membranes," *Biochimica et Biophysica Acta (BBA)-Biomembranes*, vol. 1561, no. 1, pp. 1–25, 2002.

[67] Qin, Y., Wang, X., and Wang, Z. L., "Microfibrenanowire hybrid structure for energy scavenging," *Nature*, vol. 451, no. 7180, pp. 809–813, 2008.

[68] Rao, S. S., *Vibration of continuous systems*, vol. 464. Wiley Online Library, 2007.

[69] Shahab, S., Gray, M., and Erturk, A., "Ultrasonic power transfer from a spherical acoustic wave source to a free-free piezoelectric receiver: Modeling and experiment," *Journal of Applied Physics*, vol. 117, no. 10, p. 104903, 2015.

[70] Sharma, N., Maranganti, R., and Sharma, P., "On the possibility of piezoelectric nanocomposites without using piezoelectric materials," *Journal of the Mechanics and Physics of Solids*, vol. 55, no. 11, pp. 2328–2350, 2007.

[71] Shatalov, M., Marais, J., Fedotov, I., Tenkam, M. D., and Schmidt, M., "Longitudinal vibration of isotropic solid rods: from classical to modern theories," *Advances in Computer Science and Engineering, M. Schmidt, ed., InTech Open, Rijeka, Croatia*, pp. 187–214, 2011.

[72] Shu, Y. C. and Lien, I. C., "Analysis of power output for piezoelectric energy harvesting systems," *Smart materials and structures*, vol. 15, no. 6, p. 1499, 2006.

[73] Shu, Y. C. and Lien, I. C., "Efficiency of energy conversion for a piezoelectric power harvesting system," *Journal of micromechanics and microengineering*, vol. 16, no. 11, p. 2429, 2006.

[74] Skow, E. A., Cunefare, K. A., and Erturk, A., "Power performance improvements for high pressure ripple energy harvesting," *Smart Materials and Structures*, vol. 23, no. 10, p. 104011, 2014.

[75] Tagantsev, A. K., "Piezoelectricity and flexoelectricity in crystalline dielectrics," *Physical Review B*, vol. 34, no. 8, p. 5883, 1986.

[76] Tagantsev, A. K., Meunier, V., and Sharma, P., "Novel electromechanical phenomena at the nanoscale: phenomenological theory and atomistic modeling," *MRS bulletin*, vol. 34, no. 09, pp. 643–647, 2009.

[77] Tagantsev, A. K. and Yurkov, A. S., "Flexoelectric effect in finite samples," *Journal of Applied Physics*, vol. 112, no. 4, p. 044103, 2012.

[78] Tan, D., Yavarow, P., and Erturk, A., "Resonant nonlinearities of piezoelectric macro-fiber composite cantilevers with interdigitated electrodes in energy harvesting," *Nonlinear Dynamics*, no. 92, pp. 1–11, 2018.

[79] Tol, S., Degertekin, F. L., and Erturk, A., "Gradient-index phononic crystal lens-based enhancement of elastic wave energy harvesting," *Applied Physics Letters*, vol. 109, no. 6, p. 063902, 2016.

[80] Trolier-McKinstry, S. and Muralt, P., "Thin film piezoelectrics for MEMS," *Journal of Electroceramics*, vol. 12, no. 1-2, pp. 7–17, 2004.

[81] Yudin, P. V., Ahluwalia, R., and Tagantsev, A. K., "Upper bounds for flexoelectric coefficients in ferroelectrics," *Applied Physics Letters*, vol. 104, no. 8, p. 082913, 2014.

[82] Yudin, P. V. and Tagantsev, A. K., "Fundamentals of flexoelectricity in solids," *Nanotechnology*, vol. 24, no. 43, p. 432001, 2013.

[83] Zarepour, M., Hosseini, S., and Akbarzadeh, A., "Geometrically nonlinear analysis of Timoshenko piezoelectric nanobeams with flexoelectricity effect based on Eringen's differential model," *Applied Mathematical Modelling*, vol. 69, pp. 563–582, 2019.

[84] Zhang, J., Wang, C., and Bowen, C., "Piezoelectric effects and electromechanical theories at the nanoscale," *Nanoscale*, vol. 6, no. 22, pp. 13314–13327, 2014.

[85] Zhao, S. and Erturk, A., "Deterministic and band-limited stochastic energy harvesting from uniaxial excitation of a multilayer piezoelectric stack," *Sensors and Actuators A: Physical*, vol. 214, pp. 58–65, 2014.

[86] Zhao, X., Zheng, S., and Li, Z., "Size-dependent nonlinear bending and vibration of flexoelectric nanobeam based on strain gradient theory," *Smart Materials and Structures*, 2019.

[87] Zubko, P., Catalan, G., Buckley, A., Welche, P. R. L., and Scott, J. F., "Strain-gradient-induced polarization in SrTiO3 single crystals," *Physical Review Letters*, vol. 99, no. 16, p. 167601, 2007.

[88] Zubko, P., Catalan, G., Buckley, A., Welche, P. R. L., and Scott, J. F., "Erratum: Strain-gradient-induced polarization in SrTiO3 single crystals [Phys. Rev. Lett. 99, 167601 (2007)]," *Physical Review Letters*, vol. 100, no. 19, p. 199906, 2008.

[89] Zubko, P., Catalan, G., and Tagantsev, A. K., "Flexoelectric effect in solids," *Annual Review of Materials Research*, vol. 43, pp. 387–421, 2013.